



POLITECNICO DI TORINO

*DEPARTMENT OF ENVIRONMENT, LAND AND INFRASTRUCTURAL
ENGINEERING, POLITECNICO DI TORINO*

Master of Science in Petroleum Engineering

DEVELOPMENT OF A HYDRO-MECHANICALLY COUPLED APPROACH TO ESTIMATE POTENTIAL LEAKAGE IN CARBON STORAGE WELLS

Supervisors:

Prof. Vera ROCCA

Dr. Peter FOKKER

Dr. Al MOGHADAM

Sahar AMIRI

JULY 2022

ABSTRACT

In the last few decades, the Underground Gas Storage (UGS) operation has been proven to be a sustainable solution for mitigating greenhouse gas emissions toward the European union's aim of being climate neutral by 2050. One of the main gases for storage operations is carbon dioxide, which accounts for 82% of greenhouse gases in the atmosphere. Despite the fact that CO₂ has a lower global warming potential (GWP) than other greenhouse gases, due to the amount of the emissions into the atmosphere, it is the most important greenhouse gas to be considered for efficient climate control. Depleted hydrocarbon reservoirs are suitable candidates for such purpose, and the integrity of wellbores which are pathways for injecting CO₂ into underground storage sites is a major concern for ensuring an efficient storage operation. In case of failure in the wellbore integrity, different kinds of leakage paths can appear and lead to the outflow of the captured gas. Due to the change of the pressure and temperature inside the wellbore system or shrinkage of the cement behind the wellbore casing, a clearance can be created between casing and cement or between cement and rock formation which is called microannulus. Microannulus behaves like a vertical fracture with a relatively high permeability and provides a perfect discharge way for the material.

Carbon dioxide leakage poses a hazard depending on its rate of discharge. Therefore, a model of CO₂ leakage is an important part of a risk assessment framework. As the main leakage pathway within the wellbore, characterization, and estimation of the outflow amount in microannuli is essential in UGS projects. As in the case of flow investigations in fractures, we need to know the microannulus aperture size distribution and its relative permeability to determine the leakage rates through the microannuli. For this reason, several experimental, numerical and analytical studies have been conducted to characterize microannuli and evaluate their discharge rates. In all carbon capturing and storage (CCS) projects, a caprock layer above the reservoir with a very small value of permeability plays a crucial role to trap the captured material. Consequently, there is a need for fairly high levels of integrity for both the caprock layer and well systems traversing this layer in such operations. Due to this reason, microannulus structures along the caprock layer have been taken into account in this research for modeling and flow calculations.

In this study, a finite element Abaqus model is utilized for calculating the initial mechanical size of the microannulus in the intended platform under different stress conditions throughout the entire life-cycle of the CCS well. The information on the pressure and temperature of the formation and the casing are acquirable from a CMG – GEM model and an Olga model respectively. Accounting for the effects of buoyancy, viscous, inertial, and capillary forces, we have considered the two-phase flow of water and carbon dioxide inside the microannulus without any phase changes. In the vertical direction, the considered area is divided into several elements. Incorporating all the mentioned data and using the Python programming language, a calculator package is developed based on an analytical solution. The package calculates the fluid pressure inside the microannulus for each element and then updates the mechanical size of the annular area due to the extra fluid pressure inside the microannulus according to the mechanical parameters of the system. The fluid properties including density, viscosity, compressibility factor, and gas compressibility are updating for each element based on the corresponding thermodynamic conditions. The mechanical sizes are then corrected for the hydraulic apertures in the calculator using an empirical correlation. As a result, the permeability of the system can be calculated using the hydraulic size distribution inside the microannulus and cubic law for the estimation of leakage rate.

SUMMARY

1	Introduction.....	12
2	Theoretical background	21
2.1	Mechanical deformation due to the stress variations	21
2.2	Flow components and description.....	24
2.2.1	Flow regime	26
2.2.2	Multiphase flow	30
2.2.3	Flow pattern	36
2.3	Modeling tools and methods	38
2.4	Mechanical – hydraulic aperture correlation	41
3	Methodology and research design	44
3.1	Research objectives and questions	44
3.2	Research design.....	45
3.3	Linking the models (Abaqus model description).....	47
3.4	Model Description.....	53
3.4.1	Flow components	55
3.4.2	Base model parameters	56
3.5	Flow potential and pressure deviation calculations	57
3.6	Microannulus size update (mechanical and hydraulic apertures)	59
3.7	Two-phase flow module (optional).....	64
4	Results and discussion	67
4.1	Base model results.....	67
4.1.1	Inner microannulus	67
4.1.2	Outer microannulus.....	70
4.2	Sensitivity analysis.....	74
4.2.1	Initial aperture.....	74
4.2.2	Initial reservoir pressure	75
4.2.3	Inertial coefficient.....	78
4.2.4	Element size	79
4.2.5	Caprock thickness	79

4.2.6	Mechanical parameters	80
4.2.7	Temperature	85
4.3	Two-phase flow results	85
4.3.1	Inner microannulus – Darcy module	86
4.3.2	Outer microannulus – Non-Darcy module.....	88
4.4	Entire life-cycle	91
4.5	Validity and reliability of the results.....	93
4.6	Risk identification	94
4.7	Mitigations	95
5	Conclusion	97
5.1	Research question.....	97
5.2	Key contributions and findings	98
5.3	Suggestions for future research.....	101
	References.....	102

LIST OF FIGURES

Figure 1.1. Possible leakage pathways through an abandoned well (Gasda et al., 2004)	14
Figure 2.2. The aperture of the microannulus in different points around the circumference (Garcia Fernandez, 2018).....	18
Figure 2.1. The hydraulic aperture of the microannulus as a function of effective permeability (Stormont et al., 2017).....	25
Figure 2.2. Results from two series of measurements with different confining pressures using Equation 2.6 (Stormont et al., 2017).....	28
Figure 2.3. Sample of inertial coefficient and hydraulic aperture correlation in fractures (Hatambeigi et al., 2020)	30
Figure 2.4. Brooks-Corey model (Garcia Fernandez et al., 2020).....	34
Figure 2.5. van Genuchten model (Garcia Fernandez et al., 2020)	34
Figure 2.6. Effective saturation versus capillary pressure (Garcia Fernandez et al., 2020)	35
Figure 2.7. Experimental results fitted with van Genuchten and Brooks-Corey models (Garcia Fernandez et al., 2020).....	35
Figure 2.8. Flow patterns map inside the smooth fracture with contours of pressure gradient and liquid saturation (Fourar and Bories, 1993).....	37
Figure 2.9. Flow patterns map inside the rough fracture with contours of pressure gradient and liquid saturation (Fourar and Bories, 1993).....	38
Figure 2.10. Residual aperture versus average fluid pressure (Moghadam et al., 2019) 42	
Figure 3.1. Predicted pathways for gas leakage along the wellbore system (Tao et al., 2011) – the mentioned similar pathway area along the cement, includes the intended area in this research.....	45
Figure 3.2. (a) Microannulus with the average size in the cement-casing interface (b) Non-uniform appearance of microannulus in the cement-casing interface	46
Figure 3.3. The top view geometry of the Abaqus (finite element) model.....	48
Figure 3.4. Cement and casing materials in the Abaqus model - The orange surface shows the cement-formation interface with the opening size close to 7.580e-05 (as	

mentioned in the ranging table on the left side) for the last time step of the model.	
Black circles represent the interface nodes for the first slice of the model	49
Figure 3.5. Exaggerated top view of the opening in the cement- formation/cement-casing interface	50
Figure 3.6. Angle - cubic aperture size graph for the first slice along the caprock at the last time step of the model	52
Figure 3.7. Element sensitivity analysis using leakage rate parameter.....	54
Figure 3.8. Element sensitivity analysis using aperture size parameter	54
Figure 3.9. Phase diagram of CO ₂ highlighting the zone considered in this research ...	55
Figure 3.10. wellbore system top view, showing stresses which control the opening of the inner microannulus.....	61
Figure 3.11. wellbore system top view, showing stresses which control the opening of the outer microannulus.....	63
Figure 4.1. The output of the leakage calculator package showing the variation of the internal pressure and microannulus aperture versus depth for the viscous flow - Results related to the inner microannulus.....	68
Figure 4.2. The output of the leakage calculator package showing the variation of the internal pressure and microannulus aperture versus depth for the visco-inertial flow - Results related to the inner microannulus	69
Figure 4.3. Comparison of the annual leakage rates based on the viscous flow calculations - Results related to the inner microannulus	69
Figure 4.4. Comparison of the annual leakage rates based on the visco-inertial flow calculations - Results related to the inner microannulus	70
Figure 4.5. The output of the leakage calculator package showing the variation of the internal pressure and microannulus aperture versus depth for the viscous flow – Results related to the outer microannulus.....	71
Figure 4.6. The output of the leakage calculator package showing the variation of the internal pressure and microannulus aperture versus depth for the visco-inertial flow – Results related to the outer microannulus.....	72
Figure 4.7. Comparison of the annual leakage rates based on the viscous flow calculations - Results related to the outer microannulus	73

Figure 4.8. Comparison of the annual leakage rates based on the visco-inertial flow calculations - Results related to the outer microannulus	73
Figure 4.9. Aperture curves, the output of the leakage calculator package for the sensitivity analysis of different initial aperture ranges. (a)-initial mean mechanical aperture equal to 161.32 (μm) – (b)-initial mean mechanical aperture equal to 80.66 (μm) – (c)-initial mean mechanical aperture equal to 40.33(μm)	75
Figure 4.10. Pressure curves, the output of the leakage calculator package for the sensitivity analysis of different reservoir pressures. (a)-reservoir pressure equal to 37 (MPa) – (b)- reservoir pressure equal to 37.49 (MPa) – (c)- reservoir pressure equal to 38 (MPa)	77
Figure 4.11. Aperture curves, the output of the leakage calculator package for the sensitivity analysis of different reservoir pressures. (a)-reservoir pressure equal to 37 (MPa) – (b)- reservoir pressure equal to 37.49 (MPa) – (c)- reservoir pressure equal to 38 (MPa)	78
Figure 4.12. Comparison of the annual leakage rates for different values of inertial coefficient	79
Figure 4.13. Comparison of the annual leakage rates for different values of caprock thickness.....	80
Figure 4.14. Aperture curves, the output of the leakage calculator package for the sensitivity analysis of different v_{cement} . (a)- v_{cement} equal to 0.15 – (b)- v_{cement} equal to 0.2 – (c)- v_{cement} equal to 0.25	81
Figure 4.15. Aperture curves, the output of the leakage calculator package for the sensitivity analysis of different Young’s modulus of cement. (a)- E_{cement} equal to 8160 (MPa) – (b)- E_{cement} equal to 7200 (MPa) – (c)- E_{cement} equal to 6240 (MPa).....	82
Figure 4.16. Aperture curves, the output of the leakage calculator package for the sensitivity analysis of different Young’s modulus of formation. (a)- $E_{formation}$ equal to 6000 (MPa) – (b)- $E_{formation}$ equal to 5200 (MPa) – (c)- $E_{formation}$ equal to 4400 (MPa)	84
Figure 4.17. Comparison of the annual leakage rates for different values of system temperature	85

Figure 4.18. (a)- Saturation distribution inside the inner microannulus along the caprock layer – (b)- Comparison of the annual leakage rates for single-phase and multiphase flows	87
Figure 4.19. Relative permeability curve for water and CO ₂ inside the microannulus along the pathway (the applicable range in the intended area is highlighted)	87
Figure 4.20. Aperture curves, the output of the leakage calculator package for (a)- Single-phase viscous flow inside the inner microannulus – (b)- Multiphase viscous flow inside the inner microannulus	88
Figure 4.21. (a)- Saturation distribution inside the outer microannulus along the caprock layer – (b)- Comparison of the annual leakage rates for single-phase and multiphase flows	89
Figure 4.22. Aperture curves, the output of the leakage calculator package for (a)- Single-phase visco-inertial flow inside the outer microannulus – (b)- Multiphase visco-inertial flow inside the outer microannulus	90
Figure 4.23. Cumulative leakage rate along the outer microannulus over five years of CO ₂ injection.....	92
Figure 4.24. Leakage rate variation for the outer microannulus	92
Figure 4.25. Mean hydraulic aperture variation for the outer microannulus along the caprock thickness	92

LIST OF TABLES

Tab. 3.1: Mean mechanical aperture along the caprock for the last time step of the model	52
Tab. 3.2: Base model parameters	56
Tab. 3.3: Fluid properties in the base model.....	57
Tab. 3.4: Mechanical properties of the well system materials in the base model.....	57
Tab. 4.1: Results of the sensitivity analysis for different initial aperture ranges.....	75
Tab. 4.2: Results of the sensitivity analysis for different initial aperture ranges.....	77
Tab. 4.3: Results of the sensitivity analysis for different Poisson’s ratios of cement ...	81
Tab. 4.4: Results of the sensitivity analysis for different cement Young’s modulus	82
Tab. 4.5: Results of the sensitivity analysis for different Poisson’s ratio of casing	83
Tab. 4.6: Results of the sensitivity analysis for different casing Young’s modulus.....	83
Tab. 4.7: Results of the sensitivity analysis for different formation Young’s modulus	84
Tab. 4.8: Summary of the rate measurements at the wellheads of oil and gas wells (Moghadam et al., 2021).....	94

LIST OF EQUATIONS

Equation (1.1)	16
Equation (1.2)	16
Equation (1.3)	19
Equation (2.1)	23
Equation (2.2)	23
Equation (2.3)	24
Equation (2.4)	24
Equation (2.5)	25
Equation (2.6)	27
Equation (2.7)	27
Equation (2.8)	28
Equation (2.9)	28
Equation (2.10)	29
Equation (2.11)	29
Equation (2.12)	31
Equation (2.13)	32
Equation (2.14)	33
Equation (2.15)	33
Equation (2.16)	33
Equation (2.17)	33
Equation (2.18)	33
Equation (2.19)	41
Equation (2.20)	42
Equation (2.21)	43
Equation (2.22)	43
Equation (3.1)	49
Equation (3.2)	49
Equation (3.3)	50
Equation (3.4)	50
Equation (3.5)	51

Equation (3.6)	51
Equation (3.7)	51
Equation (3.8)	51
Equation (3.9)	58
Equation (3.10)	58
Equation (3.11)	60
Equation (3.12)	61
Equation (3.13)	62
Equation (3.14)	62
Equation (3.15)	62
Equation (3.16)	62
Equation (3.17)	63
Equation (3.18)	63
Equation (3.19)	64
Equation (3.20)	65
Equation (3.21)	65
Equation (3.22)	66
Equation (3.23)	66

1 INTRODUCTION

In order to achieve the Paris 2015 objective of keeping the global mean temperature rise well below 2°C, Carbon sequestration and carbon capture have been given a lot of attention in the past decade as mitigation options to avoid the emission of CO₂ into the atmosphere (IPCC, 2005). In the case of Carbon Capturing and Storage (CCS) operations, escapes of CO₂ could contaminate shallow overlying aquifers used for water supply, hydrocarbon reservoirs, and mineral resources, or find their way into the surface (Tao et al., 2010; Ajayi et al., 2019; Ladva et al., 2004). A wellbore provides pathways for underground connections in different types of operations, such as hydrocarbon production or underground storage. As a result of drilling through several strata, there is a chance of fluids communication or upward migration. Therefore, Leakage is the main concern associated with such operations (Ajayi et al., 2019; Moghadam et al., 2022), and the risk assessment of the CO₂ leakage hazard along the wellbores is necessary and requires the estimation of the CO₂ discharge rate (Tao et al., 2010).

In order to prevent leaks, well designs usually entail several cement-filled steel casings located along the borehole at various depths. A cement slurry is pumped through the casing and flows into the annulus space between casings overlapped or between the casing and rock formations to fix the casings in place. Once the cement is hardened and set, it serves as a barrier supporting the casing and ensuring zonal isolation throughout the life of a well (Tardy, 2018; Moghadam et al., 2022; Hatambeigi et al., 2020). While the proper placement of the cement or cement-slurry design is crucial to ensure the cement's ability to isolate, they are not sufficient to guarantee its performance and other well parameters have to be taken into account. Even if the cement is well placed, changes in downhole conditions can affect the integrity of the cement sheath (Bois et al., 2011; Bellabarba et al., 2008). The cement integrity depends on the mechanical properties and geometry of the well system, and the surrounding formation (Thiercelin et al., 1998).

There can be various types of leakage paths inside underground reservoirs, including geological paths related to caprocks, faults, and fractures, and man-made paths, such as

poorly completed and abandoned wells (Tao et al., 2011). Leaks along wells can occur between the cement and the casing (Carey et al., 2009, 2010), through the cement itself (Tavassoli et al, 2018; Bois et al., 2012), or between the cement and the formation (Gu et al, 2012). Various leakage paths for an abandoned well are shown in Figure 1.1. These pathways can also be caused by a number of origins, including poor cement slurry design, inadequate downhole mapping, or poorly executed cementing procedure (Benge, 2005; Chadwick et al., 2004). Additionally, subsequent well operations can damage the cement as a result of temperature or pressure changes during injection or production (Bois et al., 2012). Cement can debond from the casing or the formation, creating an annular space called microannulus (Gasda et al, 2004; Roy et al., 2018; Corina et al., 2021), which provides a connected leakage pathway leading to significant fluid migration from the reservoir up along the well (Zhang and Bachu 2011; Gasda et al. 2004; Dusseault et al. 2014; Orlic et al., 2021).

Since intact cement has a permeability in the order of a few micro-Darcies, the small leakage rates through the cement matrix are likely to be in the range of naturally occurring background fluxes. Larger leakage rates are most likely to occur along interfaces in the steel/cement/formation systems (Crow et al., 2010). Among all the possible leakage paths that have been identified, the cement-casing or cement-formation interfaces; herein referred to as the microannulus, are regarded as the most probable leakage path (Orlic et al., 2021; Bachu and Bennion, 2009; Bellabara, 2008; Zhang and Bachu, 2011; Gasda et al., 2004). Based on collected field samples, the cement-formation interface has been identified as the most risky leak path for stored CO₂ along wells (Carey et al., 2006).

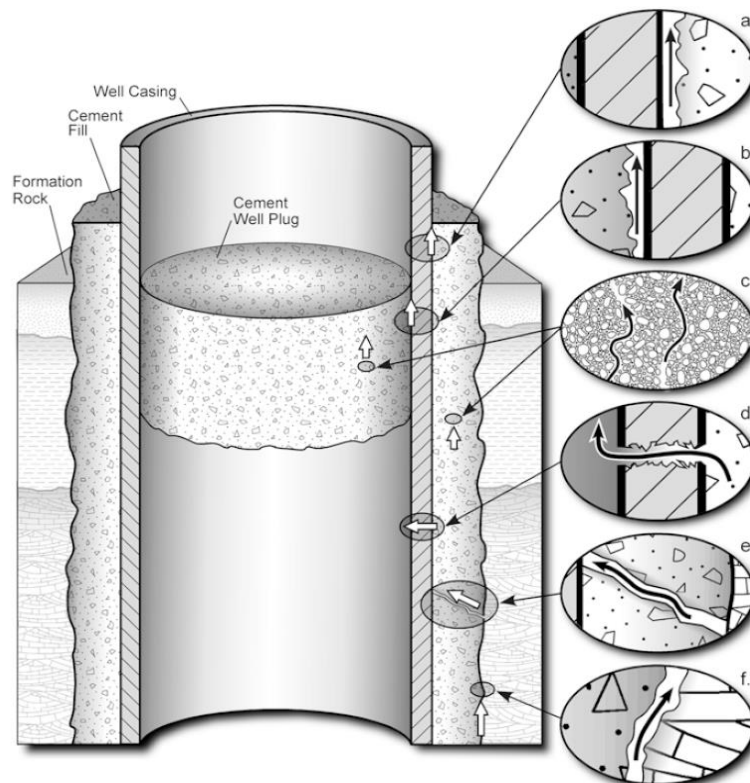


Figure 1.1. Possible leakage pathways through an abandoned well (Gasda et al., 2004)

Underground storage operations introduce chemical, thermal, and mechanical stresses to the storage reservoir, which may result in microannulus formation and increase the risks of the well leakage (Zhang and Bachu, 2011). Microannulus formation can be mainly attributed to the thermal contraction, temperature, and associated stress reduction at the interfaces due to cold fluid injection, variations in cement volume during hydration (chemical shrinkage/expansion), and high formation pressure sufficient to de-bond the cement from the casing (Lecampion et al. 2013; Feng et al. 2017). Some other factors like poor mud cake removal, early set cement, casing decentralization, formation strains, stress, and free water channels can also be considered as origins of the microannulus formation (Gomez et al., 2017; Tavassoli et al., 2018; Bois et al, 2011; Lecampion et al. 2011).

Considering the risk assessment of the leakage problems, it is crucial to estimate the size and geometry of the microannulus, permeability of the pathway, and the out-flow rates. Therefore several experimental, analytical and numerical models have been

developed in the last years to investigate these parameters (Moghadam et al., 2022). Although data regarding the characterization of wellbore microannuli are limited, the hydraulic aperture of the microannulus can be estimated from pressure build-up or flow measurements at the wellhead. Sustained casing pressure (SCP) appears in many wells, is defined as any measurable casing pressure that rebuilds after a bleed-down. The existence of leakage paths along the microannulus exhibits SCP in the well. SCP model yields information about the effective permeability of the pathway (Rocha-Valadez et al., 2014; Tao et al., 2010). Huerta et al. 2009 and Tao et al., 2010 applied the same approach using the modified SCP model and determined the cement's effective permeability and the gas leakage depth by matching the model with field data. Tao et al., 2010 described a model to investigate the flow rate of CO₂, considering single-phase flow and a continuous pathway of constant aperture to obtain a rough over-estimation of the leakage rate. Furthermore, the variation of the CO₂ properties along the pathway, imposed by temperature change (geothermal gradient), was taken into account in this research and computed with the Peng-Robinson equation of state. Tao et al., 2011 also implemented the modified model of Huerta et al. for studying the nature of leakage pathways in natural gas wells, to estimate the range of leakage rates likely to occur in a CO₂ sequestration operation (Tao et al., 2010, 2011; Huerta *et al.*, 2009). Tuuk et al., 2014 studied two types of rock formations and showed the strong dependency of the degree of cement-formation debonding to the surface properties of the formation rock. X-ray micro-computed tomography (μ -CT) was used in this study to provide a three-dimensional (3D) visualization of the cement-formation interface. Salehi et al., 2013 developed a 3D finite element model specifically for cement leakage modeling using a multistage approach in shale gas wells. Rocha-Valadez et al., 2014 introduced an analytical solution for the SCP numerical model developed by Xu et al., assuming a constant gas inflow pressure. The authors attempted to provide a theoretical frame and a model for quantitative analysis of SCP-test data. Aas et al., 2016 used conventional and expandable cement in their experimental research to investigate the cement sealability by pressurizing the set cement with water. The authors reported that the microcannulas created in this study were relatively small and did not provide large flow rates. A leakage model was developed based on the experiments to estimate the flow rate through the created microannuli based on Equation 1.1.

$$Q = \left(\frac{\pi R_c \Delta P}{6 \mu L} \right) \delta R^3 \quad (1.1)$$

where:

Q = flow rate (m^3/s)

R_c = casing radius (m)

ΔP = pressure difference across the cement (Pa)

μ = viscosity of fluid (Pa.s)

L = the length of the cement column (m)

δR = the microannulus gap (m)

Ford et al., 2017 established simple leakage calculators for quick evaluation of leakage, which were taking into account different leakage pathways including microannuli along cement interfaces. Equation 1.1 developed by Aas et al., was used for the leakage calculations in microannulus in these models. Stormont et al., 2018 conducted several experiments by creating a microannulus in a cement specimen to investigate the effect of confining, casing, and pore pressures on the gas flow inside the microannulus. The authors concluded that the microannulus acts like a fracture with respect to deformation under stress and developed an analytical gas leakage model assuming that gas only flows through the microannulus. Based on the fracture-like behavior of the microannuli, they modeled the flow using the Navier–Stokes equation coupled with the cubic law (Equation 1.2).

$$Q = - \frac{\nabla P}{12 \mu} \omega h^3 \quad (1.2)$$

where:

Q = flow rate (m^3/s)

∇P = pressure gradient (Pa/m)

μ = viscosity of fluid (Pa.s)

h = hydraulic aperture (m)

ω = length of the hydraulic aperture, which is approximated by the circumference of the casing (m)

Corina et al., 2021 used the experimental approach applying a pressure at the bottom of the inlet, creating a pressure gradient and a mass flow through the geometry. They fixed the pressure at the outlet for the numerical convergence and modeled the flow assuming a constant density, steady-state, and laminar flow approximations through the pathway. Moghadam et al., 2022 combined an experimental study with a numerical modelling approach to evaluate microannuli formation at casing–cement interface. Hydraulic aperture of the microannuli was calculated by measuring water flow through the casing–cement interface at various casing pressures and after axial displacements. The results of this study show that the size of a formed microannulus reduces by the increase in the internal casing pressures up to a certain level and after that, it remains constant in its irreducible value due to the tortuosity and roughness of the system. the axial displacement of the casing did not lead to a significant change in the hydraulic apertures. A numerical model was created with a comparable geometry to the experiments which generates the values of mechanical apertures of the microannuli. The authors then proposed a relationship to link the mechanical apertures from the numerical models to the hydraulic apertures measured in large-scale experiments.

The limiting assumption in all research projects mentioned above is the fixed microannuli geometries which are not changing during flow. For instance, the increase in the storage reservoir pressure may lead to further cement debonding and increase the size of the microannuli (Bois et al., 2019). Furthermore, several experimental studies using X-ray computed tomography (CT) visualizations of experimentally created microannuli have shown that microannuli geometries are not uniform or homogeneous (De Andrade et al., 2014, 2016; Vralstad et al., 2019). Therefore, this simplification cannot model a real situation and requires more reliable correction. The experimental approaches provide a single-valued parameter as "equivalent" or "effective" microannuli apertures based on the measured flow rates and represent the microannulus as a uniform, smooth-walled, annular gap (Boukhelifa et al., 2004; Nagelhout et al., 2010; Aas et al., 2016). Numerical models of wellbore systems which include microannuli formation, also assume the microannulus as a smooth annular gap and do not characterize the fracture-like nature of the microannulus (Stormont et al., 2018; Sandia report, 2019). Wang and Dahi Taleghani, 2017 presented a cohesive zone model to evaluate the cement sheath integrity for a hydraulic fracturing operation, which presents

the non-uniform size trend expected also in microannulus geometry which illustrates an upward size reduction in the vertical pathways (Garcia Fernandez, 2018; Sandia Report, 2019). Moreover, the results of several studies on microannulus characterization, show that the aperture size also varies considerably around the circumference of the cement or casing. Figure 1.2 shows an example of circular non-uniformity. (Corina et al., 2021; Garcia Fernandez, 2018).

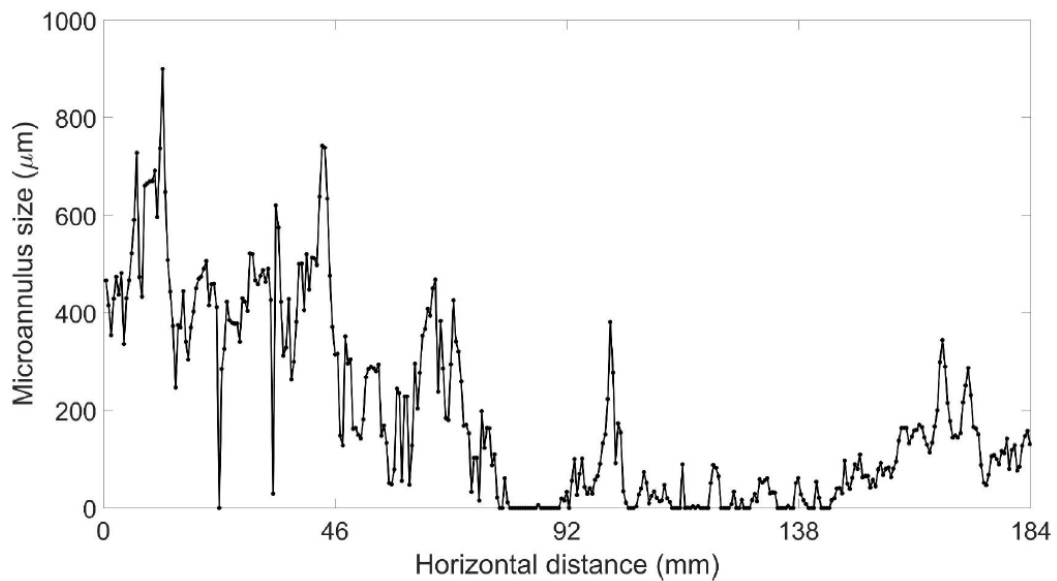


Figure 2.2. The aperture of the microannulus in different points around the circumference (Garcia Fernandez, 2018)

Even in samples with relatively large hydraulic apertures interpreted from flow measurements, perfect contact (no aperture) has been observed in some parts of the steel-cement interface in Garcia Fernandez, 2018 results. The uniform aperture assumption results in the linear Darcy flow calculations in the mentioned studies. Corina et al., 2021 expanded the Skorpa and Vralstad, 2018 study and presented results of CFD simulations of fluid flow through real microannuli geometries, obtained from X-ray computed tomography (CT) visualization. They performed the simulation with three different fluids as methane, water, and oil, and concluded that these complex flow patterns result in non-linear dependencies between flow rate and pressure gradient for the less viscous fluids, i.e. gas and water, whereas the more viscous oil display linear flow. Several recent studies on fluid flow inside the microannuli have demonstrated that they are fracture-like and do not have uniform geometries, subsequently, for a better

understanding of the actual flow, it is important to take non-linearities into account. (Skorpa and Vralstad, 2018; Garcia Fernandez et al., 2019; Hatambeigi et al., 2020). Nonlinear relation between flow rate and pressure differences at higher velocities has been attributed to inertial forces (Aagnaou et al., 2017); and flow under these conditions is referred to as visco-inertial flow (Bear, 1972). In cases that inertial forces cannot be neglected, the flow rates can be interpreted using the Forchheimer equation (Forchheimer, 1901). While Equations 1.1 and 1.2 only account for single-phase viscous flow, this equation includes both viscous (Darcy) and inertial (non-linear) flow terms (Equation 1.3) (Hatambeigi et al., 2020; Gomez et al., 2017).

$$-\nabla P = \frac{\mu}{kA} Q + \frac{\beta\rho}{A^2} Q^2 \quad (1.3)$$

where:

Q = flow rate (m^3/s)

∇P = pressure gradient (Pa/m)

μ = viscosity of fluid ($\text{Pa}\cdot\text{s}$)

ρ = density of fluid (kg/m^3)

k = permeability (m^2)

A = cross-sectional area involved in the flow (m^2)

β = inertial coefficient

Considering that leaky wellbores are usually associated with multiphase flows, understanding two-phase flow behavior in the microannulus is an important factor in the leakage risk assessments. Garcia Fernandez et al., 2020 used an experimental setup to investigate the two-phase flow of silicon oil and nitrogen along the microannulus. They injected the gaseous phase at the bottom of the specimen, to simulate the upward migration of gas along the interfaces. The authors could fit the results with Brooks-Corey and Van Genuchten models, which relate capillary pressure, saturation, and relative permeability of the two phases. They concluded that a very small gas pressures were enough to displace oil and initialize continuous gas flow In the field scales. While a continuous column of fluid can increase the mentioned breakthrough pressure, determining the initial saturation conditions is essential to evaluate the hydraulic

properties of microannuli. The results of this study can be applicable in computational models of flow along a wellbore microannulus (Sandia Report, 2021).

The potential of the gas leakage in the underground storage projects can exist both during injection and for a significant time during the post-injection site care. Therefore, long-term evaluation of the leakage risk for the entire life-cycle of these wells is crucial to ensure the success of these storage operations (Moghadam et al., 2022). As an example, Lackey et al., 2019 simulated a 50-year basin-scale injection of CO₂ and a 50-year post-injection period at a hypothetical site based on the Kimberlina Project Site in the Southern San Joaquin Valley of California. In light of all the mentioned concerns in the flow investigations inside the microannuli, there is a need to develop a more accurate leakage model taking all those factors into account and obtaining more reliable estimations. For this reason, we have developed a leakage calculator in this project to achieve a more accurate leakage risk assessment in the entire life-cycle of the underground storage wells.

2 THEORETICAL BACKGROUND

Intact wellbore cement has a very low gas permeability on the order of $10 \mu\text{D}$ ($10^{-19} - 10^{-17} \text{ (m}^2\text{)}$) (Anwar et al., 2019; Oil & Gas UK, 2015) and water permeability in the order of $0.01 \mu\text{D}$ or less (Bachu and Bennion 2009), therefore it is able to provide a good sealing against the downhole fluids flow (Corina et al., 2021; Stormont et al., 2018). Cement debonding in the interfaces can dramatically increase the effective permeability of the cement sheath and fail the required well integrity (Checkai et al., 2013; Hatambeigi et al., 2020). Seidel and Greene, 1985 indicated that a microannulus of $25 \mu\text{m}$ is large enough to be problematic for gas flow along a well, whereas Dusseault et al., 2014 state that microannuli as small as 10 to $15 \mu\text{m}$ will provide a pathway for gas movement. Having a reliable estimation of the flow rate along this annular region, requires the determination of the leakage scenario and characterization of the hydromechanical properties of the microannulus (Humez et al., 2011). Modeling the aperture and permeability evolution of microannuli over the well's history relies heavily on these parameters (Moghadam et al., 2022). Determination of the leakage scenario inside the microannulus requires a comprehensive study of flow components, flow patterns, and mechanical properties of the materials in the system.

2.1 Mechanical deformation due to the stress variations

Wellbore integrity can be affected significantly by stresses acting on the wellbore system, either from the formation or from within the casing, since these stresses may tend to open or close wellbore flaws including microannuli (Dusseault et al. 2014; Carroll et al. 2017). Since the formation surrounding the borehole must support the stresses previously carried by the removed material, the near-wellbore area will experience a stress redistribution and concentration. A stress model around the borehole associated with the in-situ stresses, mechanical properties of the materials, wellbore pressure, and well configuration is essential to predict the opening or mechanical response of the microannuli to the mentioned stresses (Do Quang et al., 2020).

Subsurface operations such as underground gas injections lead to stress changes in casing internal pressure or confining stress of the formation(s) surrounding the wellbore system. Many factors, such as overburden pressure, creep effect, wellbore system deformation due to reservoir compaction or expansion, formation pore pressure changes, cement expansion or contraction, and casing pressures and temperatures can affect the final external stresses which apply on the interfaces (Hawkes et al., 2005; Orlic, 2009). In addition to these factors, due to the high pressure inside the storage system, an additional fluid pressure inside the annular area is expected. This elevated pressure due to the CO₂ injection was modeled by Carey et al., 2013 developing a computational simulator. This model aimed to estimate the vertical propagation of the annular damage along the wellbore by taking the mentioned extra pressure into account. Although the additional pressure inside the microannulus has been considered in this study, based on the main target of this project, the pressure distribution and microannulus size update due to this pressure at different depths were not investigated. In addition, the results of the experiments conducted by Moghadam et al., 2022 confirm this effect showing a higher value of hydraulic aperture (widening) at higher water flow rates resulting in the average water pressure increase in the microannulus.

Knowing the material properties of cement, formation and steel is crucial for a reliable estimate of the stress distributions and deformations in the well systems. Cement as a non-linear complex fluid sometimes behaves as a viscoelastic material and sometimes as a visco-plastic material (Tao et al., 2021). Tao et al., 2021 reviewed the viscous rheology models for cement slurries with applications in well systems as the important input in the constitutive models. The authors, also investigated the effect of cement particle concentration, water-to-cement ratio, shear rate, temperature, pressure and the mixing method on the material performance. Description of the set-cement behavior in a stress condition is possible using its compressive strength, elastic properties (both Young's modulus and Poisson's ratio), contracting and thermal behavior (Bois et al, 2011). The deformations in the formation surrounding the wellbore system, with the presence of fluids in cracks and pores in the rocks can be described using the theory of poroelasticity. For an ideal poroelastic material, the constitutive relations are linear as in elasticity (Grandi et al., 2002).

In this study, the elastic hollow cylinder, two-dimensional plane strain solution is used to interpret the radial deformations in cement and casing interfaces, based on the radial stresses at the inner and outer boundaries. This solution cannot be applied to the cement during the hydration process, when the cement behaves more like a compacting soil, not an elastic material and its properties change over time. Considering the life-cycle duration and the intended operation (underground gas storage) in this project the cement curing period is neglected and thick cylinder theory is used to model the deformation of the material. Radial and tangential stresses in a hollow cylinder can be calculated using Equations 2.1 and 2.2 respectively (Baumgarte et al., 1999, Shi et al., 2017).

$$\sigma_r = \frac{(P_2 r_2^2 - P_1 r_1^2)}{(r_2^2 - r_1^2)} - \frac{(P_2 - P_1) r_2^2 r_1^2}{(r_2^2 - r_1^2)} \frac{1}{r^2} \quad (2.1)$$

$$\sigma_\theta = \frac{(P_2 r_2^2 - P_1 r_1^2)}{(r_2^2 - r_1^2)} + \frac{(P_2 - P_1) r_2^2 r_1^2}{(r_2^2 - r_1^2)} \frac{1}{r^2} \quad (2.2)$$

where:

σ_r = radial stress in the hollow cylinder

σ_θ = tangential stress in the hollow cylinder

P_2 = pressure applied on the outer boundary of the cylinder

P_1 = pressure applied on the inner boundary of the cylinder

r_2 = outer radius of the cylinder

r_1 = inner radius of the cylinder

The equations derived by G.Kirsch, 1898 (Equations 2.3 and 2.4) describing the stress concentration in a plate with a circular hole (plain strain condition) are used to model the stress distribution around the borehole in this research (Malvern, 1969; Grandi et al., 2002).

$$\sigma_r = \frac{1}{2}(\sigma_H + \sigma_h)(1 - \frac{R^2}{r^2}) + \frac{1}{2}(\sigma_H - \sigma_h)(1 - 4\frac{R^2}{r^2} + 3\frac{R^4}{r^4})\cos(2\theta) + \frac{\Delta PR^2}{r^2} \quad (2.3)$$

$$\sigma_\theta = \frac{1}{2}(\sigma_H + \sigma_h)(1 + \frac{R^2}{r^2}) - \frac{1}{2}(\sigma_H - \sigma_h)(1 + 3\frac{R^4}{r^4})\cos(2\theta) - \frac{\Delta PR^2}{r^2} \quad (2.4)$$

where:

σ_r = radial stress

σ_θ = tangential stress

σ_H = effective maximum horizontal principal stress

σ_h = effective minimum horizontal principal stress

R = radius of the hole

θ = azimuth measured from the direction of σ_H

ΔP = difference between the fluid pressure in the borehole and that in the formation

2.2 Flow components and description

Leakage can occur in the presence of a leak source (e.g. hydrocarbon-bearing formation), a driving force (e.g. buoyance) and a leakage pathway (Watson and Bachu, 2009). Understanding the nature of fluid flow in the leakage pathways, is very important for the correct outflow estimation. Therefore, it needs to be specified, whether the flow is laminar or turbulent, and what components are involved in the flow.

Studies have shown that microannuli deform in a fracture-like manner as a result of stress changes, therefore they can be described in terms of their aperture, similar to rock fractures. Furthermore, as it happens for the fracture networks, even under very large external pressures, microannuli remain open and are capable of conveying significant flow (Stormont et al., 2018; Berkowitz 2002; Garcia Fernandez et al., 2019; Skorpa and Vrålstad, 2018). If it is assumed that all the out-flow occurs through the microannulus, its hydraulic aperture corresponds to the effective permeability (k) of the pathway through the so-called cubic law as it is described in Equation 2.5 (Witherspoon et al.,

1980). Figure 2.1 shows the relation between hydraulic aperture of the annular area and the permeability of the pathway (Stormont et al., 2018).

$$h^3 = \frac{12kA}{\omega} \quad (2.5)$$

where:

k = permeability (m^2)

A = wellbore annular area (m^2)

h = hydraulic aperture of microannulus (m)

ω = length of the hydraulic aperture which, if flow is assumed to occur through the cement-casing microannulus, can be approximated by the circumference of the outside of the casing (m)

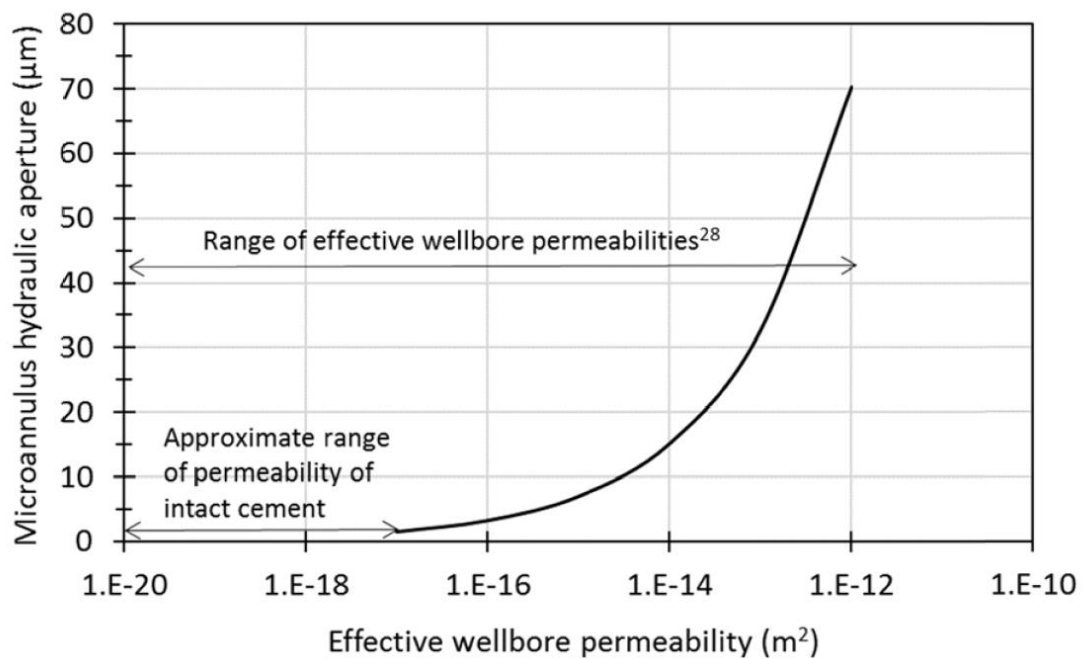


Figure 2.1. Hydraulic aperture of the microannulus as a function of effective permeability (Stormont et al., 2017)

The results of Stormont et al., 2018 research show that the cubic law provides a very close approximation for flow through annuli based on geometries typical of wellbore microannuli.

2.2.1 Flow regime

Porous-medium approaches have traditionally been used for subsurface flows in which capillary and viscous forces are involved, while inertial forces are ignored (Fourar and Bories, 1993). Several experimental studies on flow evaluation inside microannulus have shown that Darcy's law cannot describe the relationship between the pressure gradient and the measured flow rate, especially at higher flowrates where the flow deviates significantly from linearity due to the loss of kinetic energy in restrictions and constrictions (Aгнаou et al., 2017). Accordingly, inertial forces need to be taken into account in flow investigations referring to a visco-inertial flow (Lindquist, 1933; Bear, 1972; Scheidegger, 1974). Visco-inertial flow has been widely studied in rock fractures (Zimmerman et al., 2004; Zhang and Nemcik, 2013; Javadi et al., 2014; Chen et al., 2015; Zhou et al., 2015). The gas flow through fractures in the casing cement has been also investigated in several researches (Picandet et al., 2009). Hatambeigi et al., 2020 applied three different nonlinear models for fractures: the weak inertia cubic law (Mei & Auriault, 1991), Izbash's law (Izbash, 1931) and Forchheimer's law to fit the experimental data. According to the results, the last model gave the best fit to the data points from all samples. Forchheimer's equation is widely used to describe visco-inertial flow in rock fractures or microannuli due to its strong theoretical background and perfect correspondence with experimental results. The cubic law (Equation 2.5) with Forchheimer's equation, (Equation 1.3) has been used to describe the flow in microannuli in several researches considering the contribution of the inertial forces. For steady-state isothermal gas flow, Equation 1.3 can be rewritten as Equation 2.6.

$$\frac{MA(P_u^2 - P_d^2)}{2zRT\mu L\rho Q} = \frac{1}{k} + \left(\frac{\rho Q}{\mu A}\right)\beta \quad (2.6)$$

where:

M = molecular weight of the gas (kg/mol)

L = the length of the cement column (m)

z = gas compressibility factor

R = universal gas constant ($\text{m}^3 \cdot \text{Pa} \cdot \text{K}^{-1} \cdot \text{mol}^{-1}$)

T = temperature (K)

P_u = upstream pressure (Pa)

P_d = downstream pressure (Pa)

μ = viscosity of fluid (Pa.s)

ρ = density of fluid (kg/m^3)

Q = flow rate (m^3/s)

β = inertial coefficient

k = permeability (m^2)

A = cross-sectional area involved in the flow (m^2)

Stormont et al., 2018 rewrote this correlation in the form of the Equation 2.7:

$$y = \frac{1}{k} + x\beta \quad (2.7)$$

where:

y = the left-side of Equation 2.6

x = the term in parentheses on the right-hand side of Equation 2.6

They applied different pressure gradients on the sample and measured the flow rate in order to generate several pairs of (x,y). then, plotting the (x,y) pairs a straight line was generated with a slope that is a function of the inertial coefficient β (equal to zero in case of the viscous flow) and an intercept inversely proportional to permeability (Figure 2.2). The authors concluded that permeabilities corrected for visco-inertial flow in this

method, show values higher and even twice more than permeabilities interpreted from individual measurements assuming only viscous flow (Stormont et al., 2018).

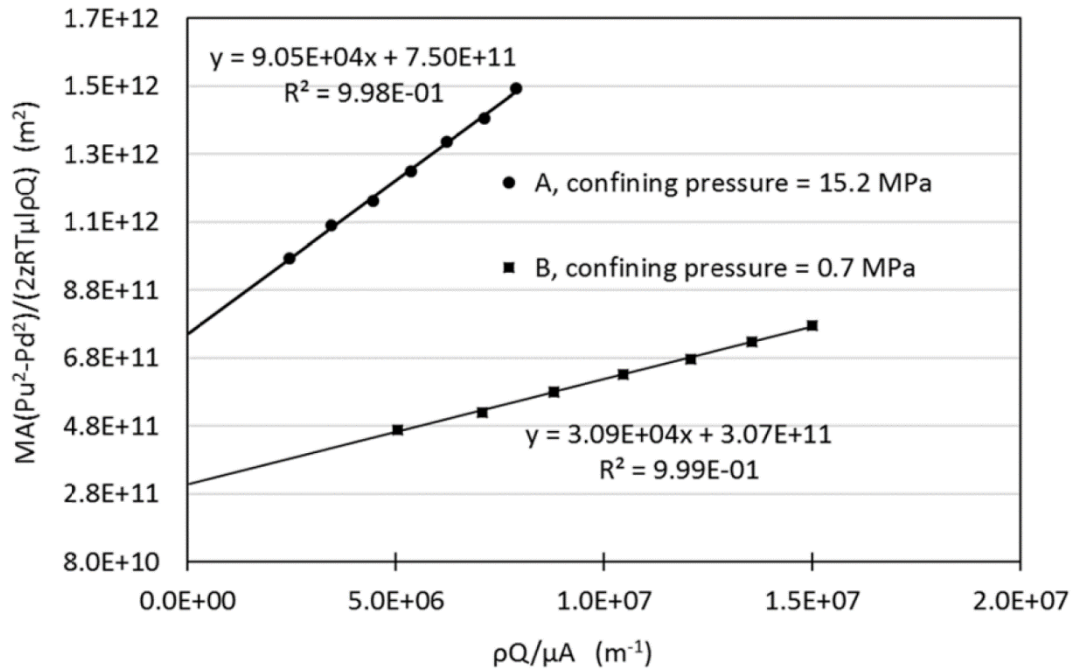


Figure 2.2. Results from two series of measurements with different confining pressures using Equation 2.6 (Stormont et al., 2017)

Several approaches have been used to discover the margin between the linear and nonlinear behavior of the flow. Hatambeigi et al., 2020 conducted several experiments on nitrogen gas flow through wellbore cement fractures under varying pressure conditions and flow rates and investigated the conditions in which non-Darcy flow occurs. They characterized the criteria to enter visco-inertial flow in terms of a critical Reynolds number (Re_c) and used parameter α as the ratio of the pressure loss due to inertial flow to the overall pressure loss. Rewriting Forchheimer's equation as Equation 2.8, the parameter α can be obtained from Equation 2.9.

$$-\nabla P = aQ + bQ^2 \quad (2.8)$$

$$\alpha = \frac{bQ^2}{aQ + bQ^2} \quad (2.9)$$

According to the recent studies, the value of 10% for α has been considered as the margin for considering the inertial flow contribution (Zimmerman et al., 2004; Ranjith and Darlington, 2007; Zhang and Nemcik, 2013; Chen et al., 2015; Zhou et al., 2015, Hatambeigi et al., 2020). Corina et al., 2021 used the Forchheimer number (Equation 2.10) as the ratio of pressure gradient required to overcome inertial forces to that of viscous forces derived from Equation 2.8 to describe the transition from viscous to visco-inertial flow (Chen et al. 2015). Zeng and Grigg, 2006 suggested that 0.11 is the critical value of the Forchheimer number (F_o), where values of F_o higher than 0.11 result in non-linear flow.

$$F_o = \frac{bQ^2}{aQ} = \frac{bQ}{a} \quad (2.10)$$

Regarding the mentioned experimental studies of non-Darcy flow, an inverse relationship has also been found between the inertial coefficient and hydraulic aperture of the microannulus (Hatambeigi et al., 2020). The same relationship has been observed earlier by Chen et al., 2015 and Zhou et al., 2015 modifying the expression of Cooke (1973) to relate β and hydraulic aperture in a power-law expression for rock fractures (Equation 2.11 and Figure 2.3) which can be applicable for the microannuli. The results of their studies showed that the coefficient m varies in a narrow range between samples, while the value of λ varies by almost two orders of magnitude.

$$\beta = \lambda h^{-m} \quad (2.11)$$

where:

β = inertial coefficient

h = hydraulic aperture

λ and m = regression coefficients

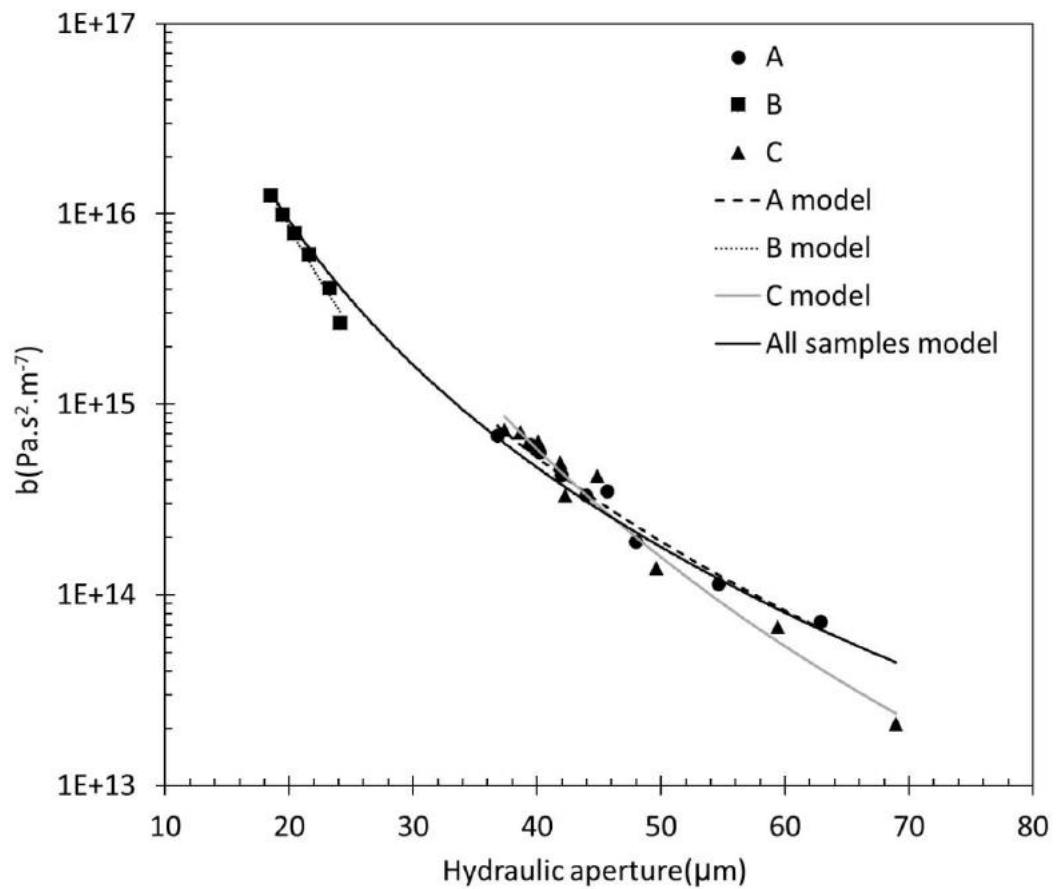


Figure 2.3. Sample of inertial coefficient and hydraulic aperture correlation in fractures (Hatambeigi et al., 2020)

2.2.2 Multiphase flow

Investigation of a multiphase flow along a vertical leakage pathway, such as vertical fractures or microannuli, requires the inclusion of capillary forces in flow evaluation models. For this reason, capillary pressure and relative permeability calculations must be added to the models. In such condition, the relative permeability accounts for the fact that each phase interferes with the flow of the other, and k_{rl} and k_{rg} are greatly influenced by phase saturations (Fourar and Bories, 1993). Capillary pressure for a fracture can be calculated using Equation 2.12 (Fourar and Bories, 1993). Equation 2.12 which can be applied for the microannuli due to their fracture-like nature, reveals that

assuming a relatively constant wettability and interfacial tension, the pore throat size variation controls the values of capillary pressure (Sivila, 2013).

$$P_c = \frac{2\sigma \cos \theta}{a} \quad (2.12)$$

where:

P_c = capillary pressure between the phases (Pa)

σ = interfacial tension (N/m)

θ = contact angle between the phases ($^\circ$)

a = aperture of the fracture (m)

Three approaches have traditionally been used to model multiphase flow in fractures: the porous medium approach, the pipe flow model, and the equivalent homogeneous single-phase model (Shad and Gates, 2010). Considering the two-phase flow conditions, Perrine, 1956 and Martin, 1959 (P-M) recommended an empirical method by substitution the single-phase compressibility and mobility into the sum of total mobility and compressibility of the multiphase system. Matthews and Russell, 1967 tried to modify the P-M approach and proposed the fluid parameter calculation method for the same theory. Considering the P-M model as an appropriate model for oil-water systems, Alkhalifah et al., 1989 and Hatzignatiou and Reynolds, 1996 applied the pressure square method for the multiphase flow system and indicated that this method is better suited for multiphase systems with a gas phase involved. Using the cumulative production data of water and hydrocarbon Xu et al., 2017 presented a dynamic relative permeability function to describe the multiphase flow behavior. Yang et al., 2016 applied a semi-analytical method to analyze the two-phase flow in complex fracture networks of the horizontal well based on the material balance theory. Fourar and Bories, 1993 conducted laminar flow experiments on smooth-walled plastic fracture cells and measured oil and brine permeability and relative permeabilities in the horizontal direction. The single-phase flow experiments were used to calculate the hydraulic aperture h of each fracture using the cubic law. Maloney and Doggett, 1997 studied the multiphase flow (oil and brine) in fractures and concluded that in the wide fracture, the dependencies of relative permeability on saturation were strongly influenced by the

densities of the fluids as well as flow directions, while in the narrow fracture, relative permeabilities were obtained as simple functions of fluid saturation. The authors used a sample of vertical fracture with the size of 787 microns to investigate two-phase flow through the experimental approach. They considered Gravitational (F_g), viscous (F_v), and capillary (F_c) forces as the primary acting forces and concluded that the effects related to differences in fluid densities appear to become less significant under the following conditions: flow rates are such that $F_v \gg F_g$; or narrow fracture widths and flow rates yield $F_v + F_c \gg F_g$.

Despite many studies that have been carried out on multiphase flow in fracture as some of them were mentioned above, the researches on multiphase flow inside microannulus are limited. Brooks-Corey (Equations 2.13 to 2.15) and van Genuchten (Equations 2.16 to 2.18) empirical correlations had been developed based on the concept of threshold pressure (P_d) and were applied to relate capillary pressure, saturation and relative permeabilities in fractures in many studies (Brooks and Corey, 1964; Van Genuchten, 1980). In the research carried on by Garcia Fernandez et al., 2020; the authors succeed to fit the experimental results of a research on flow along the microannulus with both models of Brooks-Corey and van Genuchten as shown in Figures 2.4 to 2.6 and mentioned them as the reliable models in microannulus similar to the rock fractures (Sandia Report, 2021).

$$S_e = \frac{S_w - S_{wir}}{1 - S_{wir}} = \left(\frac{P_b}{P_c}\right)^\lambda \quad (2.13)$$

where:

S_e = effective saturation

S_w = saturation at a given capillary pressure

S_{wir} = residual saturation

P_b = breakthrough pressure

P_c = capillary pressure

λ = pore-size distribution index

$$k_{rnw} = [1 - (\frac{P_b}{P_c})^\lambda]^2 [1 - (\frac{P_b}{P_c})^{\lambda+2}] \quad (2.14)$$

$$k_{rw} = (\frac{P_b}{P_c})^{3\lambda+2} \quad (2.15)$$

where:

k_{rnw} = relative permeability of non-wetting phase

k_{rw} = relative permeability of wetting phase

$$S_e = (\frac{1}{1 + (\alpha P_c)^n})^m \quad (2.16)$$

where:

S_e = effective saturation

P_c = capillary pressure

α , n and m = fitting parameters

$$k_{rnw} = [1 - S_e]^{0.5} (1 - S_e^{1/m})^{2m} \quad (2.17)$$

$$k_{rw} = S_e^{0.5} [1 - (1 - S_e^{1/m})^m]^2 \quad (2.18)$$

where:

k_{rnw} = relative permeability of non-wetting phase

k_{rw} = relative permeability of wetting phase

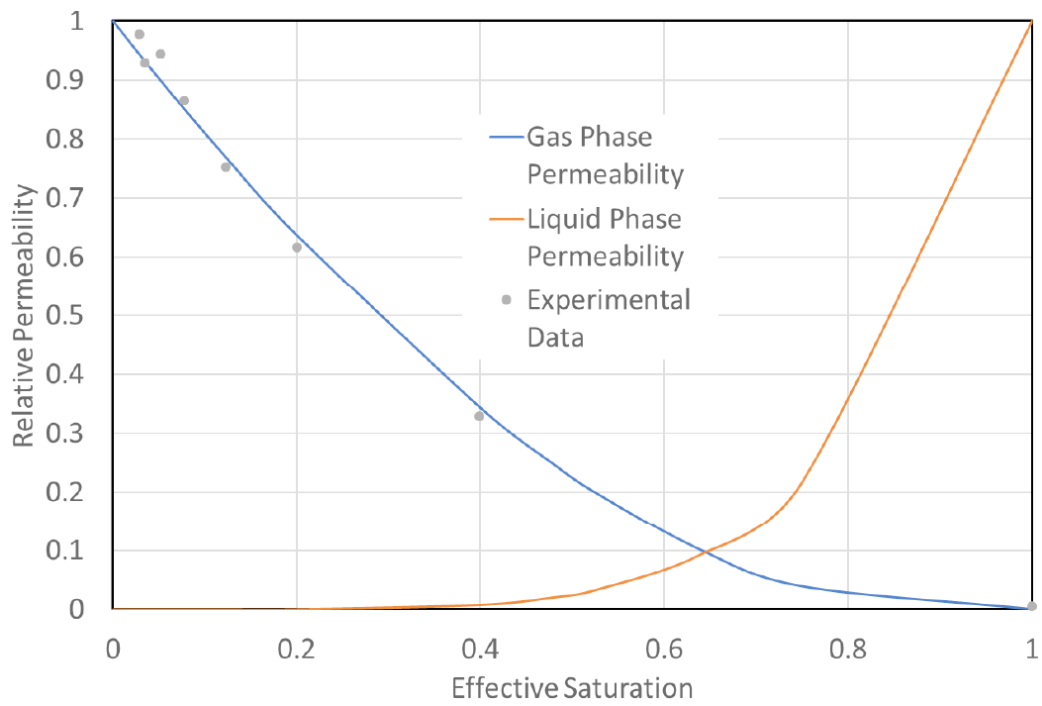


Figure 2.4. Brooks-Corey model (Garcia Fernandez et al., 2020)

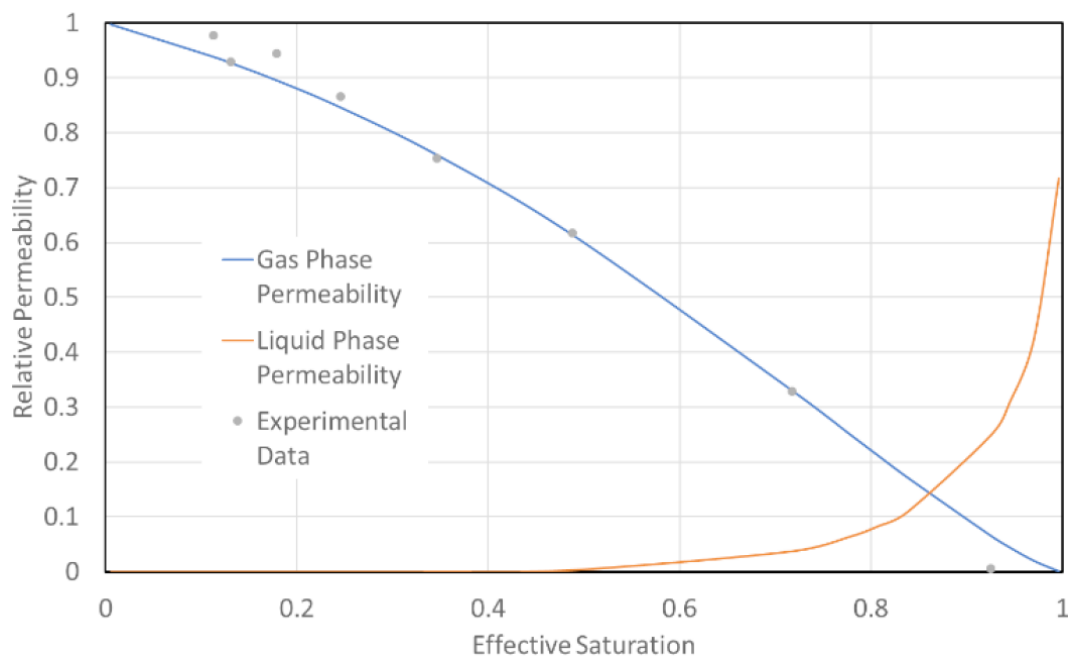


Figure 2.5. van Genuchten model (Garcia Fernandez et al., 2020)

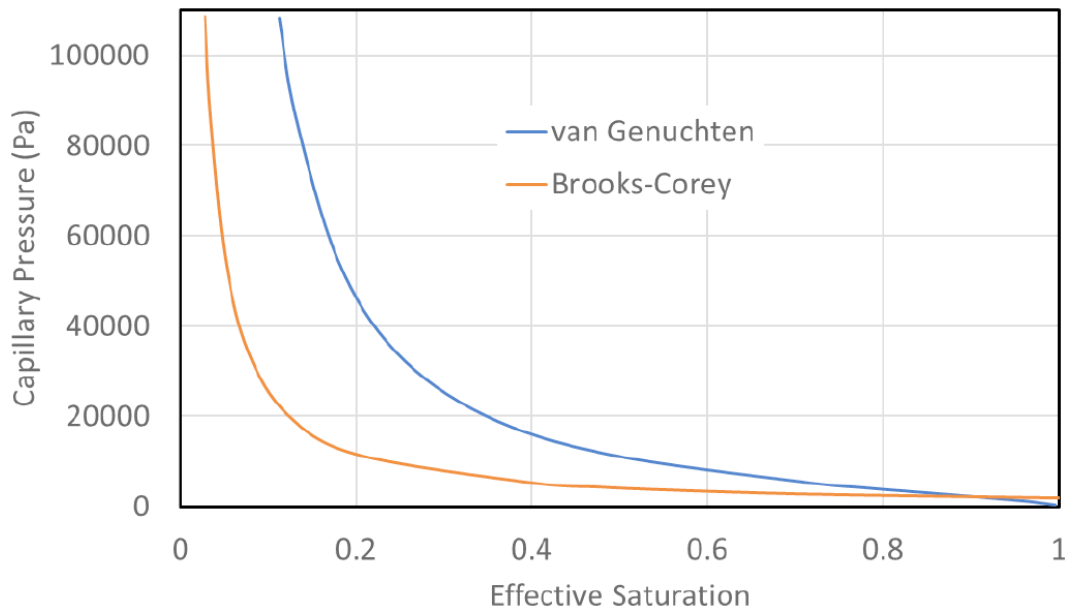


Figure 2.6. Effective saturation versus capillary pressure (Garcia Fernandez et al., 2020)

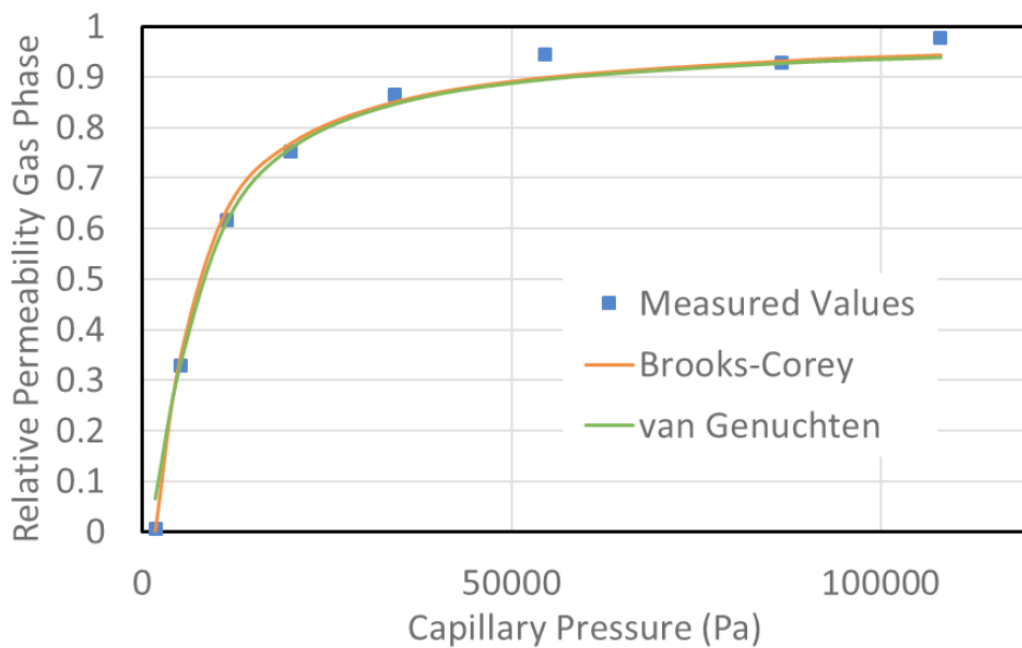


Figure 2.7. Experimental results fitted with van Genuchten and Brooks-Corey models (Garcia Fernandez et al., 2020)

Shad and Gates, 2010 showed that relative permeability is not just a function of the fluid saturations and fluid properties and flow pattern within the fracture itself are also effective and must be identified. They also observed that the change in fluid saturations, due to gravity effects, can change a co-current flow to a counter-current one. Therefore having a realistic view of the flow pattern inside the microannuli is essential to achieve a reliable estimation of the multiphase flow behavior.

2.2.3 Flow pattern

Due to the complex geometry and the occurrence of two-phase flow, identification of the flow regime inside the microannuli is extremely challenging and it may also change along the leakage pathway. Applying Laplace transformation and Duhamel superposition principle Li et al., 2022 developed a semi-analytical two-phase flow model for the vertical fracture networks to describe the complicated two-phase flow regimes. Results of this study showed seven possible flow regimes to describe the flow according to the typical curves. One of the main steps in flow pattern characterization in multiphase flow systems, is to specify the continuous and dispersed phases. The properties of the continuous phases are mostly homogeneous, while disperse phases typically have some kind of property distribution, such as particle size distribution and seepage velocity distribution. The presence of fracturing fluids in fractures in the very initial phases of production of a fractured gas reservoir leads to the existence of a continuous liquid phase and dispersed gas phase in the near-wellbore area. Continuing the production operation and by water saturation reduction, the liquid phase becomes a disperse phase and the gas phase becomes a continuous phase (Hauang et al., 2021). A similar situation is expected in the microannulus system, when it is fully saturated with water before the storage operations. Then during the UGS operation by increasing the gas pressure, it enters the annular area and finally switches the continuous phase. Fourar and Bories, 1993 used an experimental setup to investigate the flow regimes and their boundaries occurring in a gas-liquid system flowing through a horizontal fracture. The authors observed that at a low gas flow rate, gas bubbles dispersed in the flowing liquid and as the gas flow rate increased the bubbles grew larger and an unstable flow regime was created (fingering bubbles). Passing this unstable phase, at higher gas velocity, the

gas occupied the main part of the fracture and the liquid phase formed a film along the walls and the small liquid drops dispersed in the flowing gas. They concluded that unlike the flow in pipes, there is no sharp variation in the pressure gradient when the flow structure is changing in the fractures. Figures 2.8 and 2.9 were developed based on the results which represent the flow patterns for different phase velocity ratios in a two-phase system for both smooth and rough fracture systems.

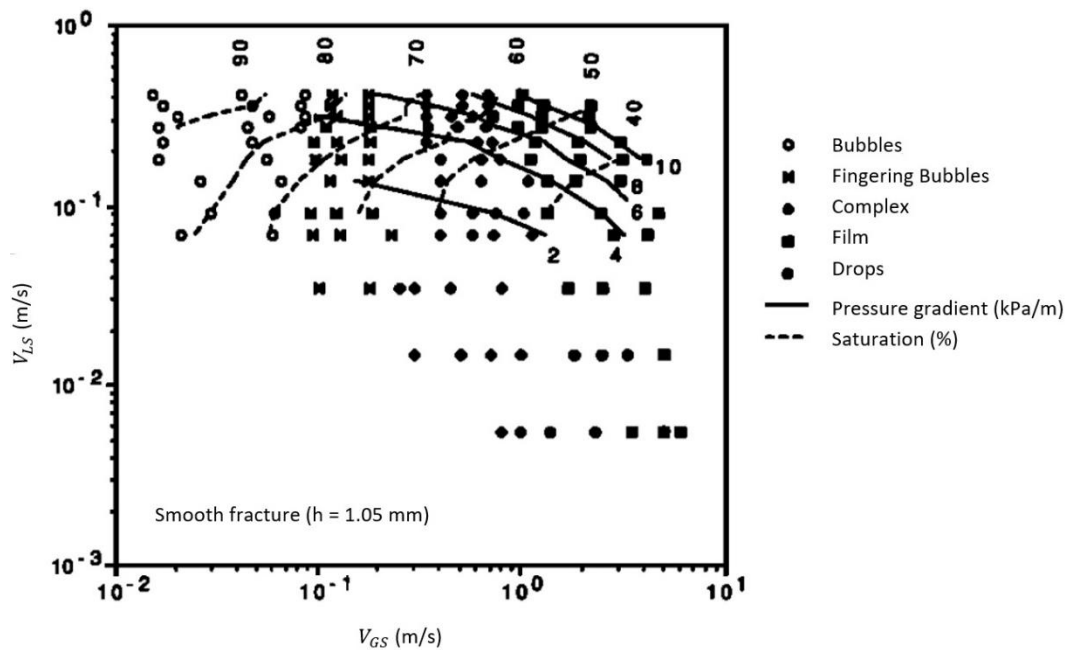


Figure 2.8. Flow patterns map inside the smooth fracture with contours of pressure gradient and liquid saturation (Fourar and Bories, 1993)

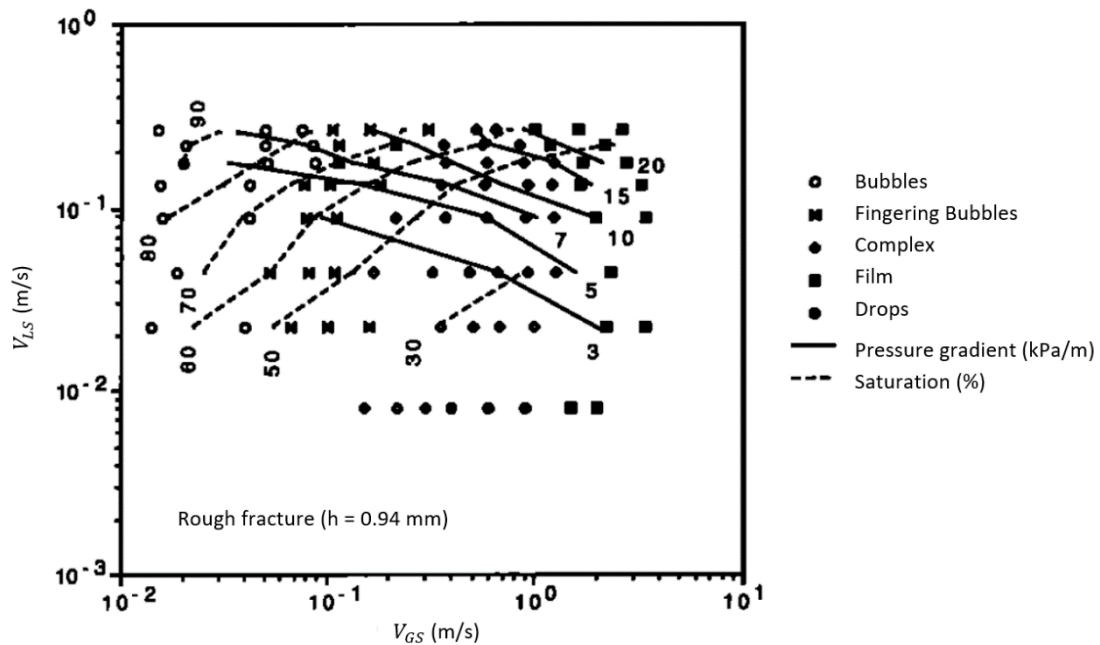


Figure 2.9. Flow patterns map inside the rough fracture with contours of pressure gradient and liquid saturation (Fourar and Bories, 1993)

2.3 Modeling tools and methods

As mentioned in the previous parts, many studies have been carried out focusing on the annular cement integrity. Each of these studies has applied an experimental, numerical or/and analytical approach to achieve the targets of the research. The use of numerical models for underground gas storage risk assessment allows for a better description of geological features and integrates hydrological, thermal, and geochemical processes (Humez et al., 2011). Despite the importance of numerical models in such studies, they should be validated by laboratory experiments or well logs to ensure their accuracy in predicting cement failure. In the following, several numerical and experimental approaches on the subject are outlined.

Bosma et al., 1999 developed a finite element model to study different loading scenarios, as well as differences in initial stress assumptions on cement sheath integrity calculations. They concluded that elastic properties of cement are important design parameters to reduce the risk of in-situ cement failure. Gray et al., 2009 provided a

review of the previous finite element models and indicated the necessity of involving the entire load history of the well in the models. Bois et al., 2012 proposed a numerical model to simulate the hydration process of cement and predict various types of cement failure. Gomez et al., 2017 presented a numerical joint model to calculate stress and displacement in the microannulus region, under varying confining and casing pressures. The conditions leading to the debonding of casing and cement were studied by Lavrov, 2018 using the numerical method. The results of this research showed that adjustment of the cement stiffness according to the formation stiffness can reduce the impact of thermal stresses. To investigate the effect of thermal stresses on cement integrity, Roy et al., 2018 conducted several numerical simulations and concluded that the risk of microannulus decreases with increasing in-situ stresses. National Risk Assessment Partnership (NRAP) developed system-modelling approach tool employing Monte Carlo analysis to study subsurface storage reservoirs (Alcalde et al., 2018). Zhang and Eckert, 2020 presented a staged finite element model to study the impact of cement pore pressure and stiffness on the cement failure. Moghadam and Corina, 2022 proposed a methodology to include the impact of cement hydration in a geomechanical model to accurately calculate the initial stress condition in cement. Their results were validated using experimental work conducted by Meng et al., 2021, where cement's pore pressure and stress were measured during hydration. To describe the visco-inertial flow through the leakage pathways, Hatambeigi et al., 2020 proposed a finite difference model applying second-order, central differencing spatial discretization and solved it explicitly in time by MATLAB script. They also used an experimental setup containing cement fractures to measure gas flow for both receiving the required input for the numerical model and validating the simulator results. Orlic et al., 2021 used a finite element simulator based on the Monte Carlo procedure to evaluate the uncertainty of the input parameters, obtain the failure modes in cement and the resulting apertures of the microannuli. They used Python scripts to sample a series of input parameters based on a prescribed distribution.

Regarding experimental approaches in cement integrity studies, Goodwin and Crook, 1992 conducted laboratory experiments to investigate the cement failure in the annular area between two casings. They observed the evolution of permeability of the annular area under different pressure cycles. The same setup was also used by Jackson and

Murphey, 1993 to evaluate the impact of the pressure cycles and well configurations. The authors concluded that permeability of the area increases as casing pressure decreases, while no permeability is expected at high inner casing pressure. De Andrade et al., 2016 used an experimental setup of X-ray computed tomography to visualize cement failure and characterize the microannulus under various loading conditions. Therond et al., 2017 utilized a large-scale setup to study the impact of various pressure and temperature conditions on cement integrity and concluded that the formation of microannuli has the biggest impact on the annular permeability. Stormont et al., 2018 investigated the impact of the confining stress and casing pressures on microannulus opening using an experimental approach. The results of this study showed that although casing pressure can close the microannulus to some degree, a residual permeability always seems to exist. Welch et al., 2020 used a triaxial direct shear setup to measure the cohesion and friction angle of the cement–steel interface. The authors observed a little change in the interface permeability due to shear displacement. Moghadam et al., 2022 measured the hydraulic aperture of a microannulus in a large-scale setup (2 (m) length) and concluded that the hydraulic aperture in a microannulus is smaller than the mechanical aperture, and that a residual aperture remains open even at high casing pressures.

An idea which has been considered in several studies to receive a comprehensive view of the cement integrity through the entire life-cycle of the well is typical multistage method. In particular, some world-famous companies, such as Total and BP, have applied complete multistage methods to simulate the overall process before, during, and after drilling (Bois et al., 2010; Therond et al., 2017). Applying this method, Gray et al., 2009 considered several stages including: Stage 1: Unperturbed stage (the wellbore is not drilled), system under the in-situ stresses. Stage 2: Drilling stage, drilling fluid pressure is applied in addition to the in-situ stresses. Stage 3: Casing and cementing stage, at the end of this stage, the pressures inside the casing and annulus may be equal or unequal. Stage 4: Cement hydration stage, at the end of this stage, all mechanical parameters of the cement-sheath reach stable values. Stage 5: Operation stage, (fracturing, injection, or production), different downhole pressures and temperatures can be applied to the system in this stage, according to the operation.

2.4 Mechanical – hydraulic aperture correlation

An important concept in microannuli characterization is the difference and relationship between the hydraulic and mechanical aperture of the microannulus. The hydraulic aperture is generally not equivalent to the actual average aperture in fractured cement and rocks (Akhavan et al. 2012). As Garcia Fernandez, 2018 pointed out, the hydraulic aperture derived from flow measurements cannot accurately reflect the mechanical (actual) aperture size of a microannulus and does not provide any information regarding its spatial variability. Due to the roughness of the microannulus walls and the tortuosity of flow paths, hydraulic aperture typically has a lower value than mechanical aperture. There can be no difference in hydraulic or mechanical sizes if the roughness between the two surfaces is much smaller than the aperture size (Moghadam et al., 2022). Furthermore, the mechanical and hydraulic aperture can be considered equal under high flow rates and large apertures. When aperture size approaches the surface roughness scale, this assumption becomes less reliable (Gomez et al., 2017). Flow can take place even at high casing pressures due to the roughness between the surfaces of the casing/formation and the cement which is related to a residual aperture of the microannulus. The relationship between the hydraulic and mechanical apertures in microannuli is largely unknown. There have been several studies proposing correlations to calculate the hydraulic aperture of a single fracture based on the mechanical aperture and some form of roughness coefficient. For instance, Barton et al., 1985 presented the following empirical relationship (Equation 2.19) using Joint Roughness Coefficient (JRC).

$$e_h = \frac{e_m^2}{JRC^{2.5}} \quad (2.19)$$

where:

e_h = hydraulic aperture

e_m = mean mechanical aperture

JRC = joint roughness coefficient

An important issue in correlations like Equation 2.19, is that when the mechanical aperture approaches zero they do not show the residual hydraulic aperture. Equation

2.20 (Moghadam et al., 2022) demonstrates the relationship between the residual aperture and fluid pressure using the definition of the residual aperture's compressibility. Figure 2.10 illustrates the changes of the residual aperture according to fluid pressure based on the results of the experiments by Moghadam et al., 2022.

$$e_r = e_i \exp(C_p P) \quad (2.20)$$

where:

e_r = residual aperture

e_i = intrinsic residual aperture (at zero fluid pressure)

C_p = compressibility

P = fluid pressure inside the microannulus

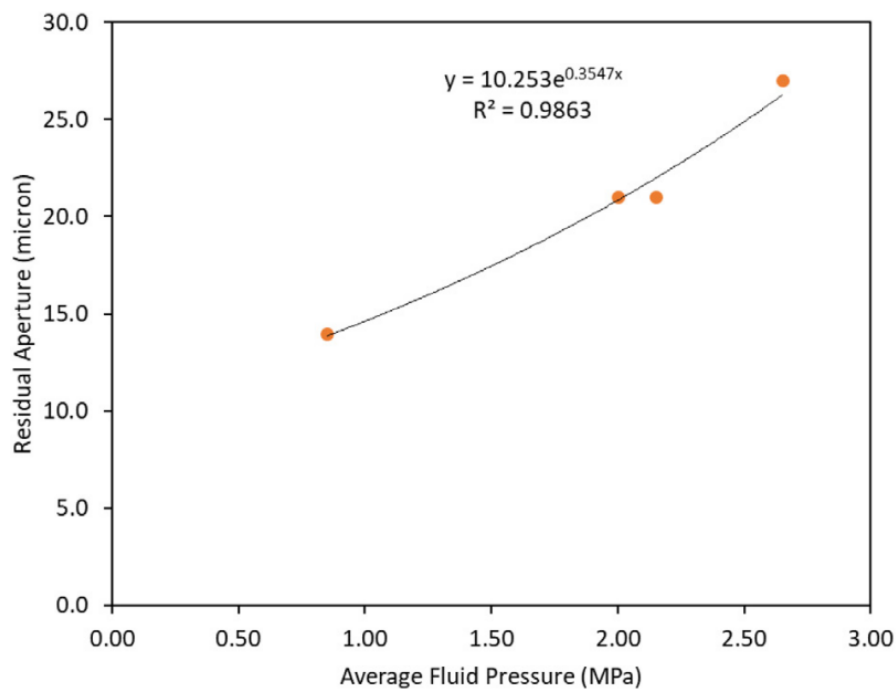


Figure 2.10. Residual aperture versus average fluid pressure (Moghadam et al., 2019)

Moghadam et al., 2022 proposed a relationship between hydraulic and mechanical aperture in microannulus (Equation 2.21) taking residual aperture into consideration. In

this correlation mechanical and hydraulic apertures are normalized using the residual aperture.

$$\frac{e_h}{e_r} = \exp \left(a \frac{e_m}{e_r} \right) \quad (2.21)$$

where:

e_r = residual aperture

e_m = mean mechanical apertures

e_m = hydraulic aperture

a = empirical parameter

P = fluid pressure inside the microannulus

Substituting residual aperture with the correlation mentioned in Equation 2.19, they obtained Equation 2.22.

$$\frac{e_h}{e_i \exp(C_p P)} = \exp \left(a \frac{e_m}{e_i \exp(C_p P)} \right) \quad (2.22)$$

where:

e_r = residual aperture

e_m = mean mechanical apertures

e_m = hydraulic aperture

a = empirical parameter

Residual aperture has been considered in Equation 2.22 and when the mechanical aperture approaches zero in this correlation, hydraulic aperture approaches the residual value. At high mechanical apertures (over 1000 micron in the present case in this study), Equation 2.22 and other correlations result in e_h values higher than e_m , which is not consistent with the expectation of having higher values for mechanical aperture. As it was mentioned, at high mechanical apertures, hydraulic and mechanical apertures are expected to be equivalent. Therefore, according to the author's recommendation, Equation 2.22 can only be ideally used for mechanical apertures below 500 microns which should be sufficient for well integrity problems related to a microannulus (Moghadam et al., 2022).

3 METHODOLOGY AND RESEARCH DESIGN

3.1 Research objectives and questions

Literature reviews indicate that there are still significant gaps in the characterization of microannuli and flow analysis inside these pathways. In addition, it is crucial to develop a reliable risk assessment approach regarding the leakage problems in the underground gas storage operations. Due to these points, this study aims to develop a more accurate calculator to estimate the leakage and aperture distribution through the microannuli. For this reason, the impact of the fluid pressure inside the microannulus in case of two-phase flow of carbon dioxide and water has been taken into account in this research. In previous studies on the flow inside the microannulus, the fluid pressure inside the pathway was assumed to be the same as the formation pore pressure in numerical or analytical models in order to determine the average mechanical size of the leakage path. On the other hand, in the experimental studies, this pressure has been fixed as a known constant value through the specimen to calculate the average hydraulic aperture of the pathway within the sample. As a result of the high reservoir pressure after a storage operation, in the case where a microannulus exists or can be created, a higher pressure than the formation pressure is to be expected at the top of the reservoir where the fluid enters the microannulus. Since the caprock formation has a very low permeability, additional pressure inside the microannulus is unable to reach equilibrium with the formation pressure. Consequently, it is expected to have a higher fluid pressure distribution inside the microannulus along the caprock, which can reach the pressure of the formation at the top of the caprock where it can have direct communication with the in-situ fluids in permeable formations. In addition to the casing and formation pressures, this extra pressure can affect the opening of the interfacial clearance between cement and formation or casing which can change the permeability of the leakage pathway and result in variations in the estimated leakage rates. The main questions of this study are how the fluid pressure and microannulus size will be distributed inside the leakage pathway through the intended area and how the final leakage flow rate will change by adding the mentioned consideration into the calculations. The approach is to model the

coupled system of fluid pressure inside the microannulus and its effect on the aperture with a newly developed calculator, and to perform a comprehensive sensitivity analysis to discover the most influential parameters.

3.2 Research design

As discussed in section 3.1, due to the high pressure inside the reservoir and the low permeability of the caprock layer, a higher pressure than the formation pressure is expected inside the microannulus through the caprock before reaching the equilibrium with the formation pressure in contact with the permeable layers. According to this fact, the caprock layer has been selected as the intended thickness for the investigation and the upward flow calculations in this research. Figure 3.1 shows the expected leakage pathway for the gas, scaping the reservoir in presence of the microannuli.

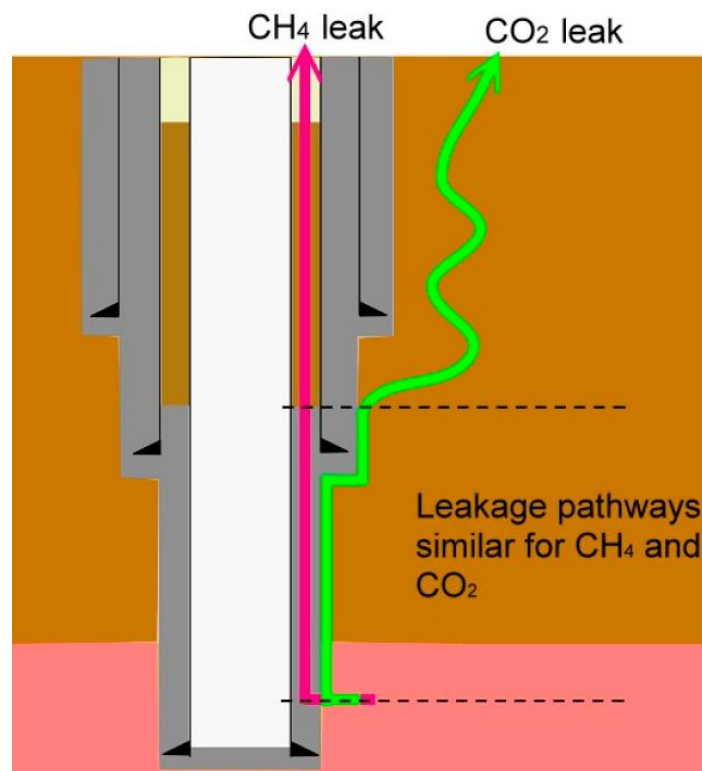


Figure 3.1. Predicted pathways for gas leakage along the wellbore system (Tao et al., 2011) – the mentioned similar pathway area along the cement, includes the intended area in this research

An average hydraulic or mechanical aperture size is usually obtained from the experimental and numerical studies which represents the effective permeability of the leakage pathway according to the cubic law. Several experimental researches have investigated the non-uniformity of the microannulus aperture using the X-ray computed tomography (CT) observing the size change in different slices of the sample. As the result of Garcia Fernandez, 2018 showed, a general trend of upward average size reduction is expected through the microannulus. Considering the extra fluid pressure inside the microannulus, being in the highest value at top of the reservoir and its upward reduction through the pathway, the same trend is expected in our study. Figure 3.2-(a) shows the microannulus appearance as the output of the simulators with the average opening size along the caprock layer and figure 3.2-(b) shows the expected trend in this study as a more realistic appearance. It should be noted that in case of occurrence of some specific events such as shale creep in reaction with carbon dioxide, this general trend can be different (zonal reduction in this example).

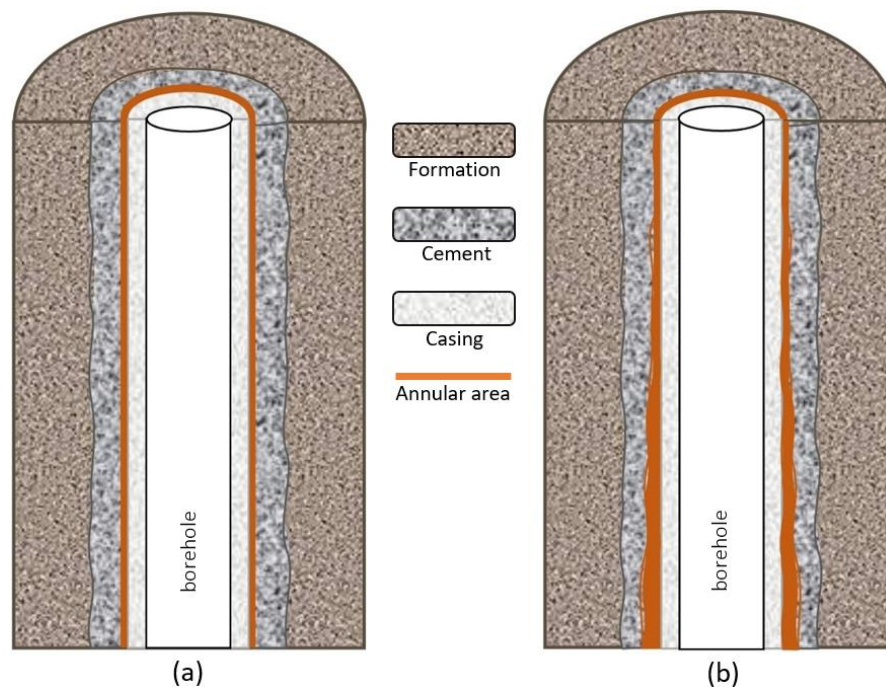


Figure 3.2. (a) Microannulus with the average size in the cement-casing interface
(b) Non-uniform appearance of microannulus in the cement-casing interface

3.3 Linking the models (Abaqus model description)

A numerical modelling methodology has been previously developed to assess the cement integrity and the size of microannuli in a CCS well (Moghadam and Orlic, 2021; Moghadam and Corina, 2022; Orlic et al., 2021). The tool uses the commercial finite element package Abaqus to model the microannulus opening under varying casing and formation pressures and temperatures. A cross-section of the 3D model is shown in Figure 3.3. Due to symmetry, only a quarter of the wellbore geometry is included in the analysis. This is sufficient to capture the change in the microannulus aperture in the tangential direction. The assumption of symmetry does not hold when cement channels and casing eccentricity are present. However, these impacts are beyond the scope of this study. The length of the model covers the entire thickness of the caprock which was assumed to be 100 m.

The methodology captures the change in near-wellbore stresses throughout the life of the well. This includes the drilling, casing placement, cementing, hydration, and production/injection stages. If debonding occurs at any stage, the size of the microannulus is recorded along the well over time. This size is the base value for the calculations in this work. The Abaqus model always assumes a hydrostatic pressure is present in the microannulus. Therefore, if the pressure is different from hydrostatic, the impact of pressure on the microannulus aperture is not captured by the Abaqus model. For the present model, steel, formation, and cement properties were taken from Orlic et al., 2021. The interfaces between the casing, cement and formation have been modeled using the surface-to-surface contact discretization method (Abaqus/Standard User's Manual, 2019). This formulation allowed us to set the debonding status and calculate the mechanical aperture of the microannulus. The initial bond between the cement and the casing was simulated using a cohesive contact model. Once the tensile stresses at the contact exceeded the bond strength, the cohesive bond broke, and the contact surfaces were free to separate. A von Mises failure criterion was used for the casing and the outer shell, while the Mohr-Coulomb failure criterion was used for the cement and the rock formation.

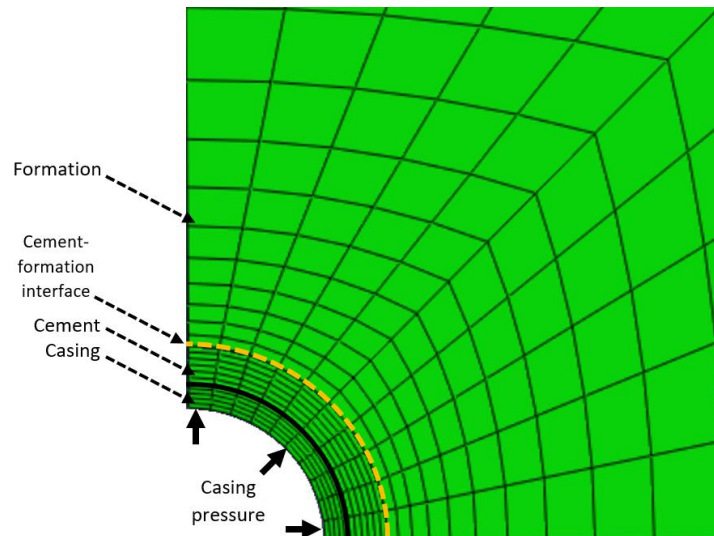


Figure 3.3. The top view geometry of the Abaqus (finite element) model

Using the Abaqus model's output, we developed a data analysis tool using a python script to provide an averaging process. This data analyzer is able to receive the microannulus opening information of the related nodes on the interface of the model (nodes of the first slice on the cement-formation interface are shown in Figure 3.4) and calculate the mean aperture around the circumferences at each depth. For this reason, after receiving the corresponding node labels, the developed tool is putting them in different classes according to the Abaqus model geometry, in which each class represents the node addresses of a single horizontal slice along the caprock thickness. Then for the values corresponding to the node labels in each group the averaging method must be applied.

The non-linear relation of the effective permeability and flow rate with the aperture size of the microannulus must be taken into consideration in the averaging method development. Equation 3.1 illustrates the correlation of the permeability with the aperture size based on the cubic law. Equation 3.2 demonstrates the correlation of the cross-sectional area with the size, as shown in Figure 3.5. Substituting both equations in the Darcy flow correlation (Equation 3.3) Equation 3.4 is obtained.

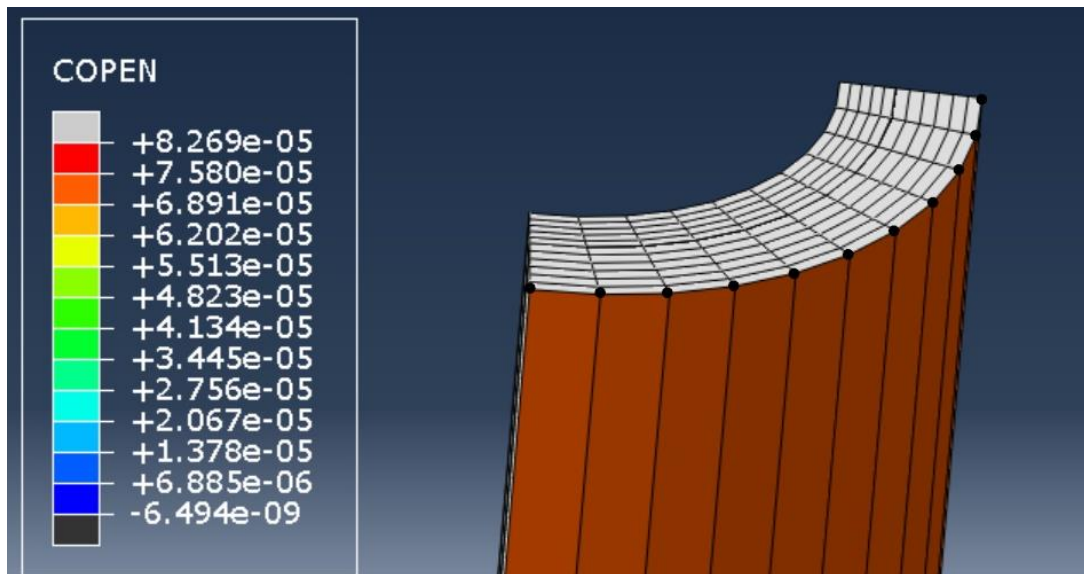


Figure 3.4. Cement and casing materials in the Abaqus model - The orange surface shows the cement-formation interface with the opening size close to $7.580e-05$ (as mentioned in the ranging table on the left side) for the last time step of the model. Black circles represent the interface nodes for the first slice of the model

$$k = \frac{h^2(\theta)}{12} \quad (3.1)$$

where:

$h(\theta)$ = hydraulic aperture for a specific angle (m)

k = permeability (m^2)

$$dA = d\theta \cdot h(\theta) \quad (3.2)$$

where:

$h(\theta)$ = hydraulic aperture for a specific angle

$d\theta$ = grid angle size

dA = grid cross-sectional area open to the flow

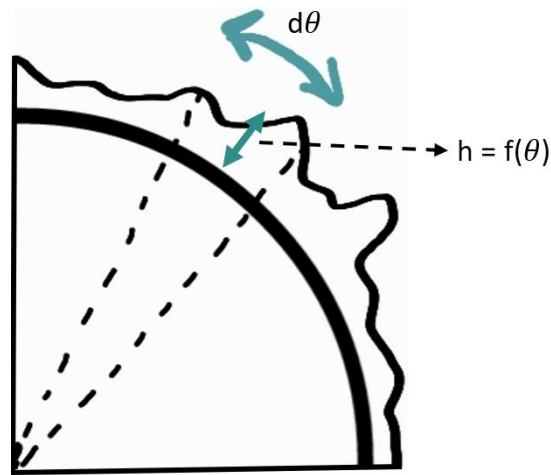


Figure 3.5. Exaggerated top view of the opening in the cement-formation/cement-casing interface

$$q = \frac{kA}{\mu} \frac{dP}{dx} \quad (3.3)$$

where:

q = flow rate

k = permeability

A = cross-sectional area in front of the flow

μ = fluid viscosity

dP / dx = pressure gradient

$$q = \frac{h^2(\theta)}{12} \frac{d\theta h(\theta)}{\mu} \frac{dP}{dx} \quad (3.4)$$

Equation 3.5 shows the last correlation after integrating. If we have a uniform opening size around the circumference, simplifying the relationship shown in Equation 3.5 for the aperture size, we obtain Equation 3.6. with the same approach Equation 3.7

represents the integral in case of the non-uniform size distribution. Therefore, the average opening size in each group in our data frame is calculating by Equation 3.8.

$$\int q = \int_0^{2\pi} \frac{h^2(\theta)}{12} \frac{d\theta h(\theta)}{\mu} \frac{dP}{dx} \quad (3.5)$$

$$h = \text{cte.} \rightarrow \int_0^{2\pi} h^3(\theta) d\theta = h^3(\theta) \cdot \theta \Big|_0^{2\pi} = 2\pi h^3(\theta) \quad (3.6)$$

$$\int_0^{2\pi} h^3(\theta) d\theta = 2\pi \bar{h}^3(\theta) \quad (3.7)$$

where:

\bar{h} = mean opening size around the circular area

$$\bar{h}(\theta) = \sqrt[3]{\frac{1}{2\pi} \int_0^{2\pi} h^3(\theta) d\theta} \quad (3.8)$$

On the other hand, having the opening size for all nodes around the circular area in our data frame, we can plot angle versus cubic size as the example shown in Figure 3.6. This plot demonstrates a relationship between angle and aperture size power three, therefore the surface area under this graph can be used as the value of the integral in equation 3.7. The surface area under the graph is calculated using Equation 3.2 for all involved nodes. substituting the integral in Equation 3.7, we receive the average size of the opening for each slice along the caprock layer.

The output of this tool will be used as the input for the initial values of the microannulus opening in the main leakage calculator in this project. For instance, the output of the mentioned data analysis on our Abaqus model for the last time step of the model shows the average values mentioned in Table 3.1 for 22 slices along the caprock layer (100 (m) thickness). Regarding the selected element size in our leakage calculator package, equal to 0.1 (m), the mean opening values in the Table 3.1 are extrapolating for the elements they cover in the calculator.

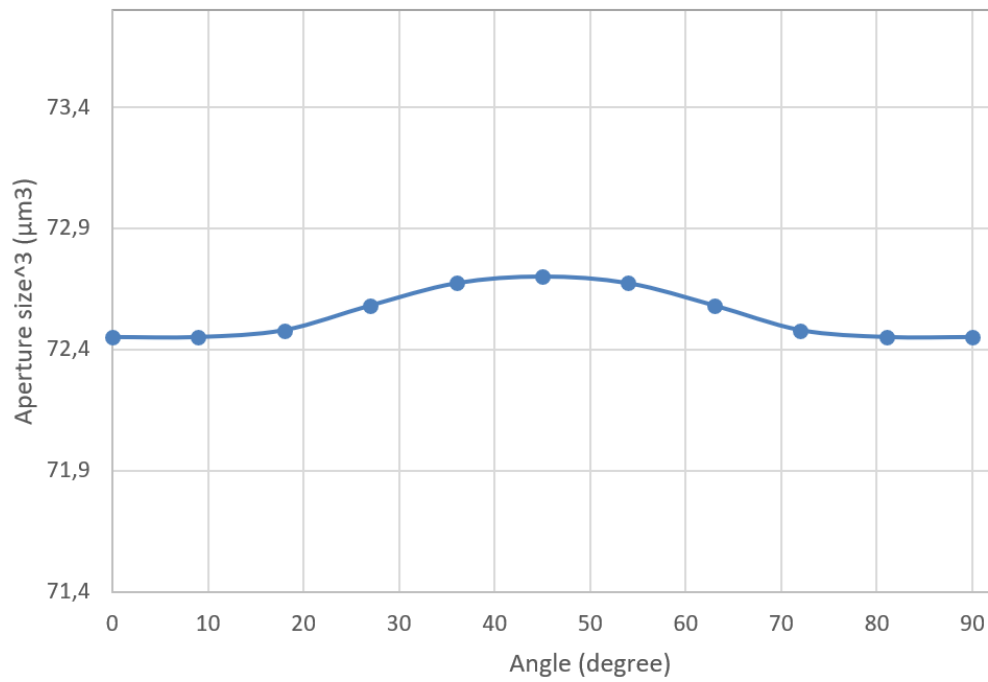


Figure 3.6. Angle - cubic aperture size graph for the first slice along the caprock at the last time step of the model

Tab. 3.1: Mean mechanical aperture along the caprock for the last time step of the model

Slice	Depth (m)	Mechanical aperture (μm)
1	3100.00	74.88
2	3095.23	84.68
3	3090.47	77.85
4	3085.71	83.12
5	3080.95	79.04
6	3076.19	82.23
7	3071.42	79.72
8	3066.66	81.71
9	3061.90	80.12
10	3057.14	81.39

11	3052.38	80.36
12	3047.61	81.20
13	3042.85	80.52
14	3038.09	81.08
15	3033.33	80.61
16	3028.57	81.00
17	3023.80	80.67
18	3019.04	80.96
19	3014.28	80.71
20	3009.52	80.93
21	3004.76	80.72
22	3000.00	80.92

3.4 Model Description

Using the python script, an iteration method has been applied in this project to develop the calculator and generate the fluid pressure distribution inside the microannulus along the caprock. For this purpose, the whole intended area (caprock thickness) has been divided into a certain number of elements with the size (thickness) equal to (dx). The final value of the dx in the calculator is chosen according to an element size sensitivity analysis. The size of the dx is reduced step by step in this analysis and then dx versus flow rates and hydraulic aperture outputs of the calculator have been plotted. Once the selected parameters become stable, the element size can be chosen as the input value of the calculator. Figures 3.7 and 3.8 show the element size (grid) sensitivity analysis in the model based on model inputs mentioned in section 3.2.3. As it is highlighted in these figures, element sizes below about 0.5 (m) result in stabilized output values. Regarding this analysis and optimum process time, value of 0.1 (m) has been selected for the element size in this study.

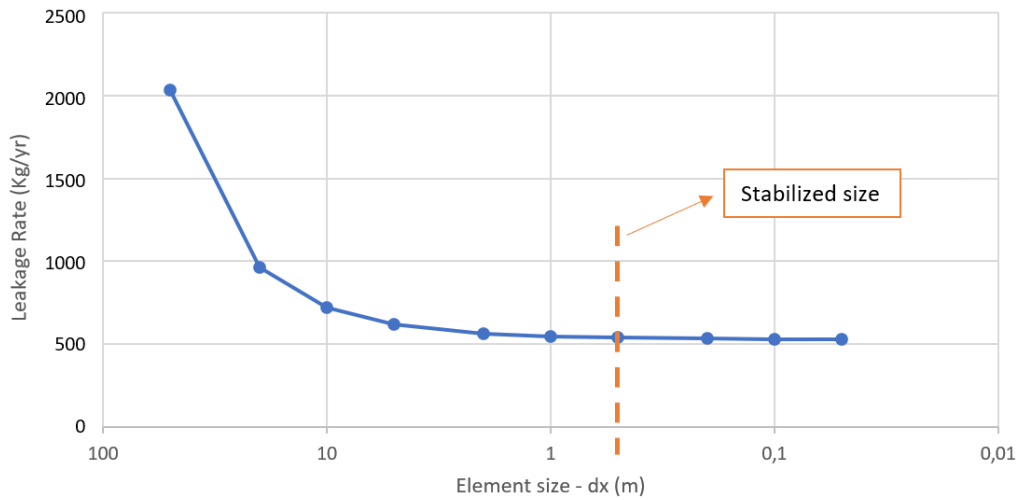


Figure 3.7. Element sensitivity analysis using leakage rate parameter

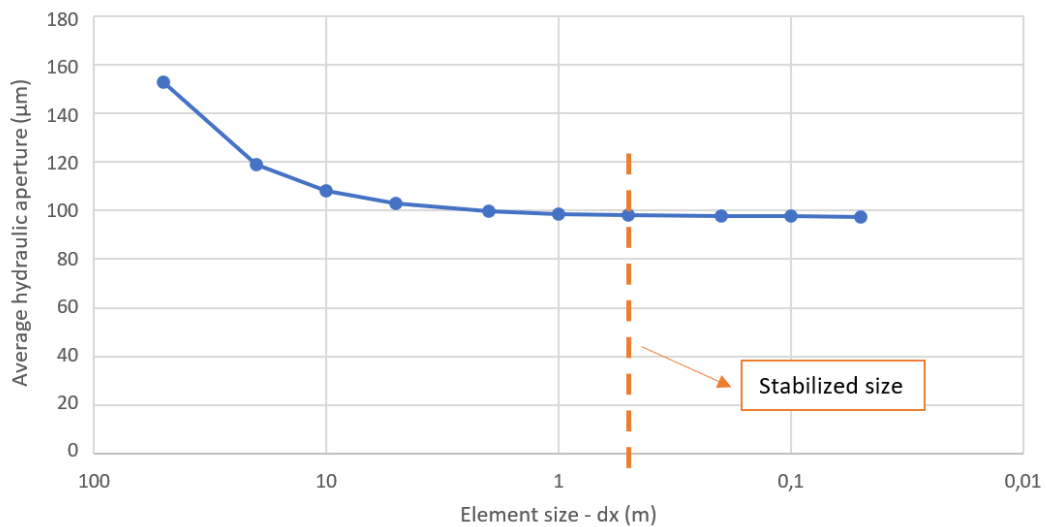


Figure 3.8. Element sensitivity analysis using the aperture size parameter

The pressure values at the beginning and end of the region are known as the boundary conditions and they are equal to the reservoir pressure and the formation pressure at the caprock top, respectively. At each time frame during the gas injection or after the injection operation, the average mechanical size of the microannulus is known from the Abaqus numerical model as the initial condition. Knowing the initial pressure value and microannulus size in the pathway entrance (top of the reservoir, first element), the calculator estimates step-by-step the pressure value for the next element. Then obtaining the value of the extra pressure inside the microannulus for each element, its effect on

the microannulus opening is calculating based on the mechanical parameters of the system applying the approach described in section 3.6. The updated mechanical apertures are then converted to the hydraulic values using equation 2.22 and recorded in the size distribution list. The calculations are repeated for each element until the final step is reached and the last pressure value is obtained. As the boundary condition of the model, this value must converge the formation pressure, therefore the whole loop will be repeated until this result is achieved. Upon convergence, the generated list of the microannulus size and the fluid pressure inside the microannulus is the desired distributions.

3.4.1 Flow components

Since leaky wellbores are commonly associated with multiphase flows and its importance in risk assessments, CO₂ and water are considered as involved fluids in our model. Figure 3.9 shows the expected phase state of the CO₂ in the expected thermodynamic conditions range in this project along the intended depth (through the caprock thickness).

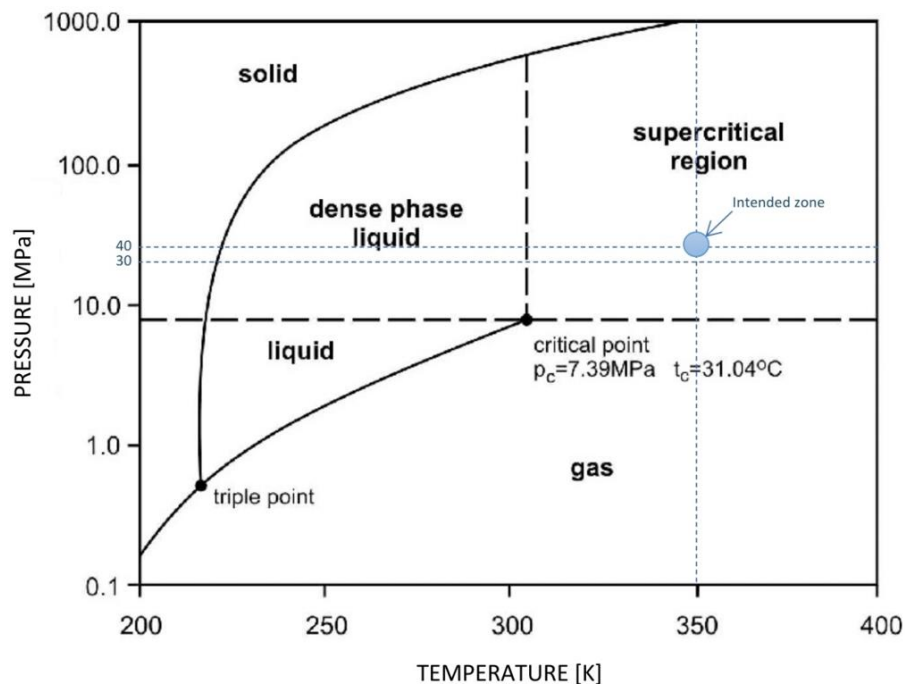


Figure 3.9. Phase diagram of CO₂ highlighting the zone considered in this research

3.4.2 Base model parameters

In the first phase of this project, a synthetic source of data has been considered for the calculator generation and result interpretation. The model developed with this series of data is called as “base model” in this study. Tables 3.2 to 3.4 represent the input data of the base model.

Tab. 3.2: Base model parameters

Parameter	Value (unit)		Note
Caprock thickness	100 (m)		-
Caprock base	3100 (m)		SSL
Borehole size	20.00 (cm)		For the whole thickness
Casing OD	17.78 (cm)		For the whole thickness
Casing ID	16.17 (cm)		For the whole thickness
Temperature	350 (K)		At 3100 m SSL, Reducing upward 3°/100 m
Initial mechanical aperture	Cement/casing interface	Cement/formation interface	For the outer microannulus from the Abaqus model outputs
	150 (µm)	-	
Inertial coefficient	10e3		-
	At caprock base	At caprock top	
Formation pressure	37.5 (MPa)	36.5 (MPa)	Gradient : 0.443 Psi / ft
Casing pressure	37.8 (MPa)	38.06 (MPa)	-
Fluid pressure inside microannulus	39 (MPa)	36.5 (MPa)	-

Tab. 3.3: Fluid properties in the base model

Parameter	Carbon Dioxide		Water	
	At caprock base	At caprock top	At caprock base	At caprock top
Viscosity (Pa.s)	$78.02 * 10^{-6}$	$75.11 * 10^{-6}$	$3.68 * 10^{-4}$	$3.83 * 10^{-4}$
Density (kg/m3)	827.09	811.40	990.21	989.2
Molecular weight (g/mol)	44		18	
Compressibility factor	0.712	0.681	-	

Tab. 3.4: Mechanical properties of the well system materials in the base model

Parameter	Casing	Cement	Formation
Young's modulus	200 (GPa)	7.2 (GPa)	5.2 (GPa)
Poisson ratio	0.3	0.2	-

3.5 Flow potential and pressure deviation calculations

As mentioned in section 3.2.1, for each element, the calculator estimates the value of the fluid pressure inside the microannulus using the pressure of the previous element. In order to have an accurate estimation of the pressure at each level, a comprehensive consideration of all driving forces is required. In this project gravitational (buoyancy), viscous, inertial and capillary forces have been considered in the calculations due to the following reasons. According to the flow direction inside microannuli, which is fully vertical in vertical wells or has a noticeable vertical component in the deviated wells, and considering the range of the caprock layers' thicknesses, a significant value of pressure drop due to the buoyancy is expected in the system. Due to the high pressure inside the storage reservoir after the gas injection, a significant potential for the viscous flow is developing along the microannulus. The mentioned potential in many cases leads to the gas flow rates large enough to put the inertial forces into contribution.

Furthermore, according to the multiphase flow consideration in this project, a capillary pressure will be built in the fluids interface which affects the flow. In order to take all the mentioned driving forces into consideration, a comprehensive structure has been applied. For this purpose, in the first step, pressure drops were corrected for pressure heads using Equations 3.9 to 3.10 (Equation 3.10 is the result of subtracting Equation 3.9 for two adjacent elements).

$$\Phi_{g_i} = P_i - \rho_{g_i} g h_i \quad \text{and} \quad \Phi_{g_{i+1}} = P_{i+1} - \rho_{g_{i+1}} g h_{i+1} \quad (3.9)$$

$$\Delta\Phi_i = \Delta P_i - \Delta P_{\text{head}} \quad (3.10)$$

where:

P_i = fluid pressure inside microannulus in element (i)

Φ_{g_i} = gas flow potential in element (i)

S_{w_i} = water saturation in element (i)

ρ_{g_i} = gas density in element (i)

h_i = depth of element (i)

In order to take the effect of viscous and inertial forces into account, we developed two separate modules called Darcy and Non-Darcy modules. The Forchheimer number (Fo) (Equation 2.10) is used to understand the boundary between the viscous and visco-inertial behavior of the flow inside the microannulus and the $Fo > 0.11$ presents the visco-inertial flow in our model. For each specific reservoir, the calculator first runs the Darcy module and using the obtained flow rates, it is calculating the Forchheimer number. An average value for the fluid parameter is used for Fo calculation in this step. The average values for these parameters such as density and viscosity are obtained from the first run of the calculator using the Darcy module. The value of the interfacial coefficient in our data frame has been chosen by interpolation of the experimental data by Hatambeigi et al., 2020. Then according to the value of the Fo, the calculator decides if the Darcy module was enough or inertial forces must be also considered to have a more reliable estimation. In the latter case, the Non-Darcy module will be run and generates the desirable results.

In the running process of each of the mentioned modules, by moving upward through the annular area, pressure and temperature are varying and consequently the properties of the fluid such as density and viscosity are changing. Therefore, three modules have been defined in our calculator package to update the values of viscosity, density and compressibility factor of the gas in different depths with various thermodynamic conditions. These modules are able to calculate the mentioned parameters for CO₂, H₂ and CH₄. Regarding the density module, the correlation of Ouyang, 2011 (The Open Petroleum Eng Journal 4, 13-21), Peng-Robinson EOS (1971) and Lemmon and Huber, 2008 correlation have been used for CO₂, CH₄ and H₂ respectively. The viscosity module employs the Lee (1966) viscosity model of natural gases for CH₄ and Muzny et al., 2013, model for H₂. These tools are called in the Darcy and non-Darcy calculators for each element to update the calculation parameters.

In most of the underground storage reservoirs, after the injection process, the saturation of the water is reducing to very low values. Inside the microannulus, a small value of the irreducible water saturation is expected due to the relatively large size scale. In addition, the transition time in the first stages of injection when the water saturation in the microannulus is reducing to its final low value, is too short in comparison to the whole injection and post-injection leakage periods. Relying on the mentioned condition, the effect of the water flow interference in the final leakage amounts after years, can be really small. Therefore, the contribution of the capillary force and two-phase flow has been added as an optional ability to our calculator package. In the beginning, the user will decide to put the multiphase flow assumption in the calculations on the "ON" or "OFF" status. In this way, in case of higher water saturation in the reservoir or smaller sizes of microannulus, the user can take it into account for a more accurate estimation and ignore them in the other cases to speed up the processing of the tool.

3.6 Microannulus size update (mechanical and hydraulic apertures)

As mentioned in section 3.3, the Abaqus model is generating the initial mean mechanical apertures of the microannulus considering all the involved stresses including formation stresses around the borehole, casing pressure and formation

pressure. The only parameter which is ignored in the Abaqus model and the other models in the literature, is the real fluid pressure distribution inside the microannulus. Instead of this pressure, a value equal to the formation pressure has been considered in the numerical model. Therefore, the contribution of the difference between the mentioned pressures as the real fluid pressure inside the annular area must be taken into account in the leakage rate assessments. During this step of the calculation, our tool adds the effect of this additional pressure inside the microannulus to the opening of the pathway at each element. The averaging tool introduced in section 3.3, provides the initial mechanical size of the microannulus for each step as the output of the mentioned data processing to be updated in this step (Table 3.1). Pressure values inside the microannulus are generating for each element with the process explained in section 3.4. Having these values and the formation pressure at different depths (hydrostatic pressure), the extra pressure for each step can be calculated (Equation 3.11).

$$P_{\text{extra}} = P_{\text{MA}} - P_f \quad (3.11)$$

where:

P_{MA} = fluid pressure inside microannulus

P_f = formation pressure

In order to measure the radial displacement of the microannulus walls at each element due to the additional internal pressure, two different models have been used for the inner and outer microannulus. In this research, the inner microannulus stands for the annular area between casing and cement and the outer microannulus represents the annular area in the cement–formation interface. According to the geometry and mechanical properties of the materials in the system, we used the thick cylinder theory for cement and casing materials, and the Kirsh solution for the formation, to calculate the radial displacement of the walls.

Figure 3.10 illustrates the top view of the wellbore system with all stresses involved in the deformation calculations for the inner microannulus. Equation 3.12 shows the general hook's constitutive law for the radial strain in the polar coordinate system. Equation 3.13 represents the relationship between radial strain and radial displacement.

Using these correlations and thick cylinder theory (Equation 2.1), the radial displacement at the boundaries of cement/casing can be obtained by Equation 3.14. Removing the effect of the stresses which are considered in our Abaqus model and keeping the value of the extra fluid pressure within the pathway, we investigated the change in the microannulus aperture in our case. For this reason, our package is calculating the radial displacement in both surfaces (walls) of the microannulus and applies the deformation in both directions on the initial aperture to estimate the updated size of the microannulus. Equations 3.15 and 3.16 show Equation 3.14 after substitution of our desired values for each step in order to update the mechanical aperture of the inner microannulus for the casing and cement sides respectively.

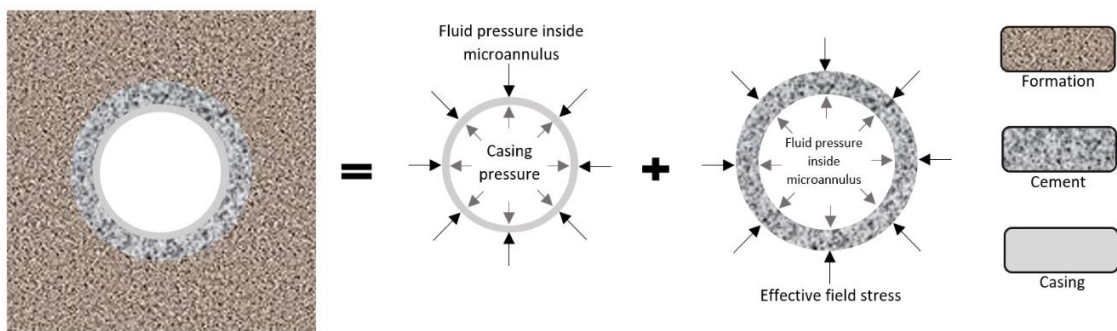


Figure 3.10. wellbore system top view, showing stresses which control the opening of the inner microannulus

$$\varepsilon_r = \frac{1}{2G} ((1 - \nu)\sigma_r - \nu\sigma_\theta) \quad (3.12)$$

where:

ε_r = radial strain

ν = Poisson's ratio

σ_θ = tangential stress

σ_r = radial stress

G = shear modulus

$$\epsilon_r = \frac{dr}{r} = \frac{u}{r} \quad (3.13)$$

where:

u = radial displacement

$$u = \frac{(1-2\nu)}{2G} \frac{(P_2 r_2^2 - P_1 r_1^2) r}{(r_2^2 - r_1^2)} + \frac{1}{2G} \frac{(P_2 - P_1) r_2^2 r_1^2}{(r_2^2 - r_1^2)} \frac{1}{r} \quad (3.14)$$

where:

P_2 = pressure applied on the outer boundary of the cylinder

P_1 = pressure applied on the inner boundary of the cylinder

r_2 = outer radius of the cylinder

r_1 = inner radius of the cylinder

$$u = \frac{(1-2\nu_{casing})}{2G_{casing}} \frac{(P_{extra} r_{OR_csg}^2) r_{OR_csg}}{(r_{OR_csg}^2 - r_{IR_csg}^2)} + \frac{1}{2G_{casing}} \frac{(P_{extra}) r_{OR_csg}^2 r_{IR_csg}^2}{(r_{OR_csg}^2 - r_{IR_csg}^2)} \frac{1}{r_{OR_csg}} \quad (3.15)$$

$$u = \frac{(1-2\nu_{cement})}{2G_{cement}} \frac{(0 - P_{extra} r_{OR_csg}^2) r_{OR_csg}}{(r_{borehole}^2 - r_{OR_csg}^2)} + \frac{1}{2G_{cement}} \frac{(0 - P_{extra}) r_{OR_csg}^2 r_{borehole}^2}{(r_{borehole}^2 - r_{OR_csg}^2)} \frac{1}{r_{OR_csg}} \quad (3.16)$$

where:

P_{extra} = additional pressure inside microannulus

r_{OR_csg} = outer radius of the casing

r_{IR_csg} = inner radius of the casing

$r_{borehole}$ = borehole radius

Figure 3.11 shows the top view of the wellbore system with all the stresses involved in the deformation calculations for the outer microannulus. As mentioned, for the outer microannulus, thick cylinder theory is used to model the mechanical response of the material on the cement side (Equation 3.14), while for the formation side, Kirsh solution is applied to measure the mechanical displacements. Again using the general hook's constitutive law (Equation 3.12 and 3.13) and Kirsh theory, Equation 3.17 is obtained to calculate radial displacement at the formation boundary. Removing the effect of the

stresses which are considered in our Abaqus model and substituting our desired values for each step, Equation 3.17 is simplified to Equation 3.18 which allows us to calculate the radial displacement in the formation side of the outer microannulus. Radial displacement on the cement side is calculating with the same approach for the inner microannulus as is shown in Equation 3.19.

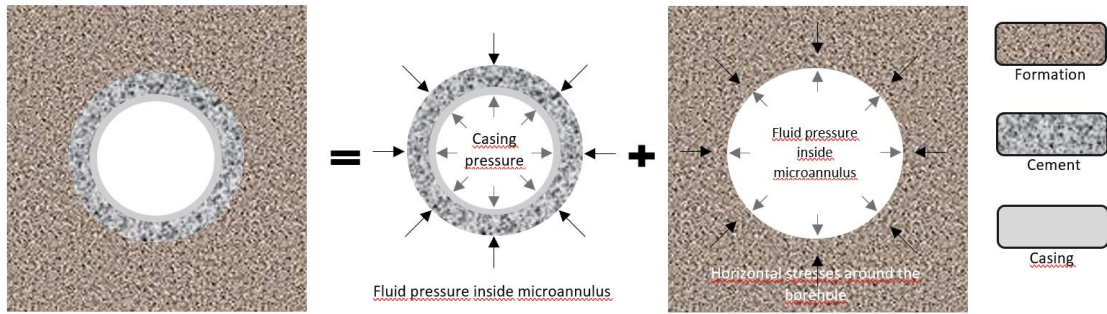


Figure 3.11. wellbore system top view, showing stresses which control the opening of the outer microannulus

$$\mathbf{u} = \frac{r}{2G} \left[\frac{1}{2} (\sigma_H + \sigma_h) \left[(1 - 2\nu_{formation}) - \frac{R^2}{r^2} \right] + \frac{1}{2} (\sigma_H - \sigma_h) \left[1 - (1 - \nu_{formation}) 4 \frac{R^2}{r^2} + 3 \frac{R^4}{r^4} \right] \cos 2\theta + \frac{\Delta P R^2}{r} \right] \quad (3.17)$$

where:

σ_H = effective maximum horizontal principal stress

σ_h = effective minimum horizontal principal stress

R = radius of the hole

θ = azimuth measured from the direction of σ_H

ΔP = difference between the fluid pressure in the borehole and that in the formation

u = radial displacement

G = shear modulus

ν = Poisson's ratio

$$\mathbf{u} = \frac{1}{2G_{formation}} (P_{extra}) r \quad (3.18)$$

$$\mathbf{u} = \frac{(1-2\nu_{\text{cement}})(P_{\text{extra}}r_{\text{borehole}}^2)r_{\text{borehole}}}{2G_{\text{cement}}(r_{\text{borehole}}^2 - r_{\text{OR_csg}}^2)} + \frac{1}{2G_{\text{cement}}} \frac{(P_{\text{extra}})r_{\text{OR_csg}}^2 r_{\text{borehole}}}{(r_{\text{borehole}}^2 - r_{\text{OR_csg}}^2)} \frac{1}{r_{\text{borehole}}} \quad (3.19)$$

When the mentioned radial displacements are applied to the initial mechanical sizes, a new list of aperture values is generated, referred to as the updated mechanical apertures. It is necessary to convert these updated values to hydraulic apertures in order to use them in cubic law and flow computations. To perform this conversion at each element, equation 2.22 is applied with the assumption of an irreducible aperture equal to 10 (μm).

3.7 Two-phase flow module (optional)

As mentioned in section (2.2.2), the Brooks-Corey and van Genuchten models, both are capable to model the relationship between saturation, capillary pressure and permeability inside the microannuli. In this research, we have chosen the Brooks-Corey model (which also showed the better fit in the Sandia's report, 2021) to correlate saturation and relative permeability values in the multiphase flow calculations. In order to apply this model it is crucial to employ a reliable value of the pore-size distribution index for the intended system. Sources providing estimations for this index in fractures and microannuli are scarce. For the range of the average aperture of our input data set, the value of 0.8 is selected for (λ) based on the extrapolation of the value provided by Garcia Fernandez et al., 2020. In the multiphase module of our package, a function is defined to generate the relative permeabilities of the involved phases along the pathway. This function imports the water saturations for each element and calculates the relative permeabilities using the Brooks-Corey model (Equations 2.12 to 2.14). Gas relative permeabilities are then used in the flow calculator modules to yield more reliable leakage estimations.

The ability to obtain reasonable relative permeabilities is strongly dependent on knowing the saturation values at each step. The water saturation inside the reservoir is known and must be entered in the calculator package inputs. The variations of

interfacial tension (IFT) and contact angle between CO₂ and water are almost negligible for pressures more than 7 MPa. Considering the size of each element in our computations (0.1 (m)), we can assume that using Equation 2.12, IFT and contact angles are the same for the two first adjacent elements and Pc is changing by size. With this assumption, the ratio of the Pc values in the two first elements can be obtained by Equation 3.20.

$$\frac{P_{c_2}}{P_{c_1}} = \frac{h_1}{h_2} \quad (3.20)$$

where:

P_{c_1} = capillary pressure in the first element

P_{c_2} = capillary pressure in the second element

h_1 = microannulus aperture in the first element

h_2 = microannulus aperture in the second element

Inspiring from the empirical correlation between Pc and saturation, developed by Kwon and Pickett, 1975 (Equation 3.21), and knowing the Pc of the first element by Equation 2.12 and Sw in the first element (equal to reservoir saturation), we can obtain fitting parameter (B) in this correlation. ($\emptyset = 1$ inside the annular area)

$$P_c = 19.5(S_w)^{-1.7} \left(\frac{k}{100\emptyset} \right)^B \quad (3.21)$$

where:

Pc = capillary pressure (psia)

k = permeability (md)

ϕ = porosity (fraction)

Sw = water saturation (fraction)

According to equation 3.20, we obtain the capillary pressure in the second element.

Equation 3.21 is then used to calculate the water saturation at this step using the fitting

parameter derived from the above approach. At this point of computation, the calculator will have the Pc and Sw values for the two initial elements.

In order to generate the saturation values in the whole intentional area, a dimension-less parameter of Pc type is defined as illustrated in Equation 3.22.

$$\text{Dimensionless-Pc} = \frac{P_{c_i}}{P_{c_0}} \quad (3.22)$$

where:

P_{c_i} = capillary pressure in element (i)

P_{c_0} = capillary pressure in the first element (entrance of the microannulus)

This parameter is then related to the water saturation in each element through Equation 3.23. With the knowledge of the Pc and Sw pairs in the first two elements, the multiphase module obtains the fitting parameters (a and b) for each specific geometry. Then, Equations 3.20 and 3.23 are used at each step through the computation process to generate the water saturations along the pathway. These saturations are then employed by the relative permeability function to update the flow calculations.

$$\text{Dimensionless-Pc} = a(S_w)^b \quad (3.23)$$

where:

S_w = water saturation

a and b = fitting parameters

4 RESULTS AND DISCUSSION

4.1 Base model results

4.1.1 Inner microannulus

In the very first step of the result observation, we have run the calculator package for the inner microannulus (with the average mechanical size of 150 (μm) along the caprock). using the base model parameters (section 3.4.2) as the inputs. Figure 4.1 shows the pressure and aperture variations inside the microannulus through the intended layer based on the Darcy module calculation. Figure 4.2 presents the same graphs for the Non-Darcy module. As it is illustrated in these figures, after applying the effect of the additional fluid pressure inside the microannulus, we observe higher values of pressure within the pathway leading to the wider openings inside the annular area. Formation pressure along the intended pathway is changing from 37.5 MPa (at 3100 m) to 36.5 MPa (at 3000 m), while the pressure inside the pathway is varying from the value of 39 MPa (reservoir pressure) to 36.5 MPa at the end of the impermeable layer. The green dash lines in the graphs show the parameters as they have been considered in the numerical model (i.e. considering the formation pressure inside the microannulus with the avg mechanical size equal to 150 (μm) in this case. The yellow lines show the updated mechanical size trend after taking the extra pressure into account. The updated value of around 312 (μm) for the mechanical aperture at the beginning of the pathway is almost 2 times bigger than its initial value. The average of the updated mechanical sizes equal to 231.14 (μm) is about 50% bigger than the initial average. The red solid lines in these graphs represent the main outputs of this research. In the pressure plots, the red line shows the fluid pressure distribution inside the microannulus. In the left side plots, the red lines represent the variation of the microannulus hydraulic aperture which must be employed in the flow calculations in order to obtain the most reliable estimation for the outflow rates. The average hydraulic aperture obtained for the pathway is equal to 97.37 (μm) and 97.42 (μm) for the Darcy and Non-Darcy calculators respectively.

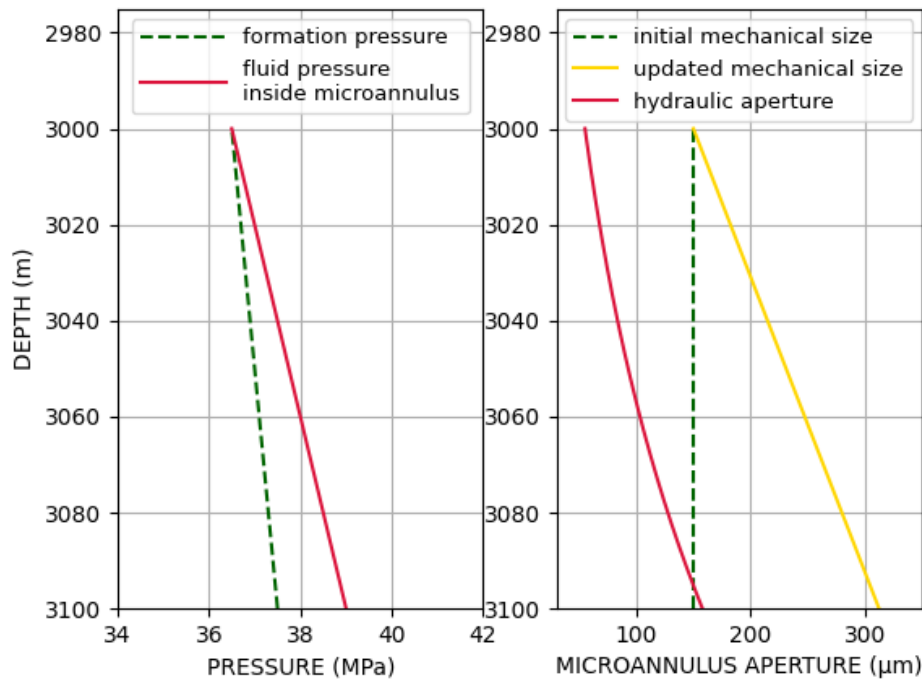


Figure 4.1. The output of the leakage calculator package showing the variation of the internal pressure and microannulus aperture versus depth for the viscous flow - Results related to the inner microannulus

In the Darcy and Non-Darcy modules, the pressure variability is almost identical despite a small difference in the orders of a few Pa for each element. The same consistency is expected and observed in the aperture trends as a result of the microannulus size at each step being updated based on the extra pressure in our model.

Figures 4.3 and 4.4 illustrate the leakage flow rates obtained from our package, compared to the rough estimations for viscous and visco-inertial flows respectively. The approximated values are estimated using the Darcy and Non-Darcy flow equations based on the known pressure values in the boundaries and the average size and fluid properties along the caprock. Yellow bars in the charts show the flow rates calculated using the average of the initial mechanical size along the pathway. This average value is then converted to a hydraulic aperture average according to equation 2.21. Red bars show the flow rates corresponding to the hydraulic average. The green bars are generated based on the pressure and hydraulic aperture distributions inside the microannulus developed in the calculator package outputs.

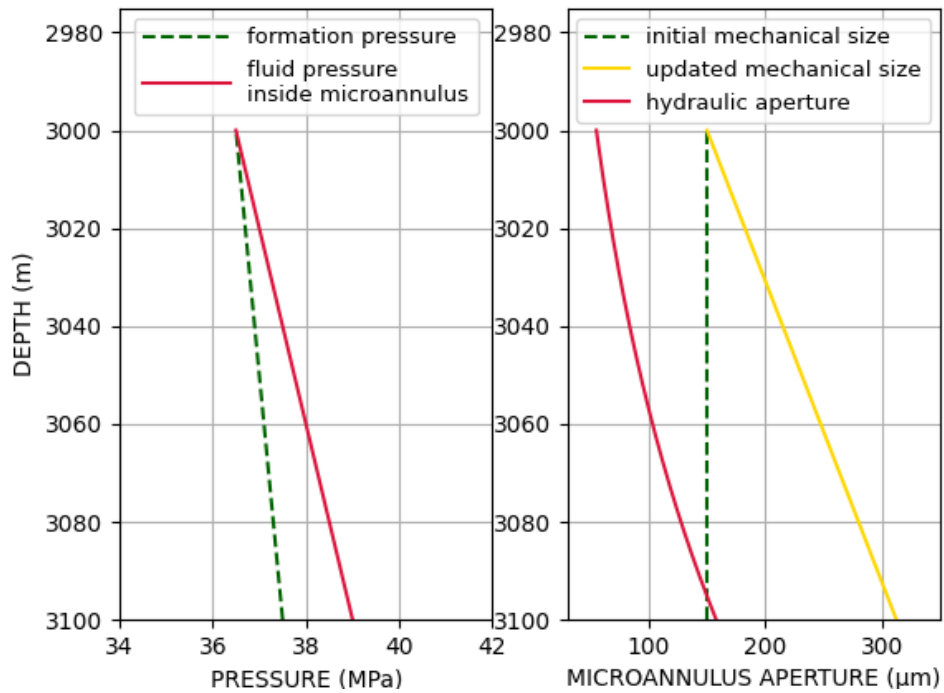


Figure 4.2. The output of the leakage calculator package showing the variation of the internal pressure and microannulus aperture versus depth for the visco-inertial flow - Results related to the inner microannulus

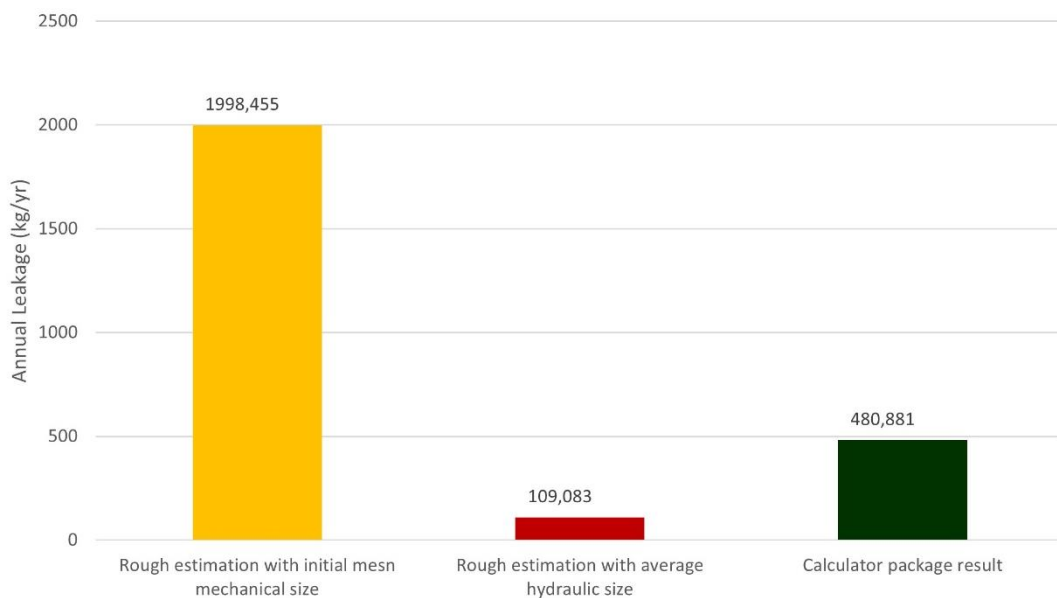


Figure 4.3. Comparison of the annual leakage rates based on the viscous flow calculations - Results related to the inner microannulus

According to these charts, it is concluded that taking the additional pressure's effect into consideration is important and can significantly change the flow rates and the estimated leakage amounts. For our synthetic data, the outflow estimation of the calculator package for viscous flow is about four times smaller than the rough estimation based on the mechanical size average and about four times bigger than the rough estimation based on the hydraulic average. With the same comparison done for visco-inertial flow, the value obtained is about two times smaller than the rough estimation based on mean mechanical aperture, and about three times bigger than the rough estimation based on the average hydraulic size.

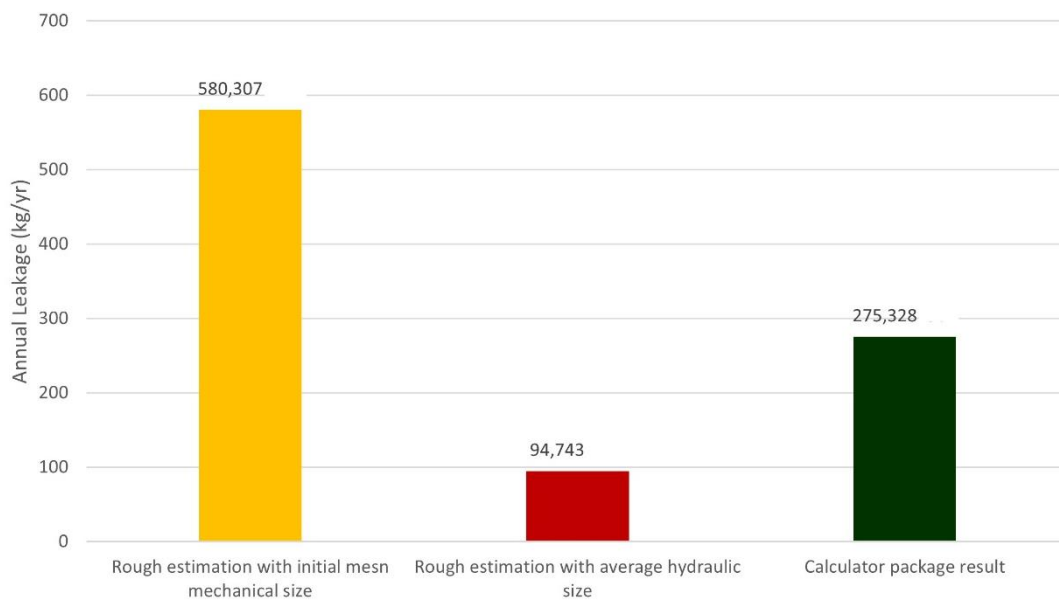


Figure 4.4. Comparison of the annual leakage rates based on the visco-inertial flow calculations - Results related to the inner microannulus

4.1.2 Outer microannulus

For the flow characterization in the outer microannulus, as mentioned before, the processed outputs of the Abaqus model are used as the initial mechanical aperture values (Table 3.1). Using these aperture lists and the base model inputs, Figure 4.5 and 4.6 are obtained for the pressure and aperture changes along the intended area based on the Darcy and Non-Darcy modules. The same result of higher pressure and opening

values at each element is also evident in the outer microannulus. The dashed lines in these plots exhibit some fluctuations due to the small variations in mechanical size distributions obtained from the Abaqus model. At the beginning of the pathway, the updated mechanical size is about 315 (μm) which is almost four times as big as the mechanical size estimated from the Abaqus model. The average of the updated mechanical apertures is about 200.20 (μm), which is 2.5 times larger than the initial size average (80.66 (μm)). Hydraulic aperture estimated for the pathway is 83.92 (μm) for Darcy and 84.07 (μm) for Non-Darcy modules.

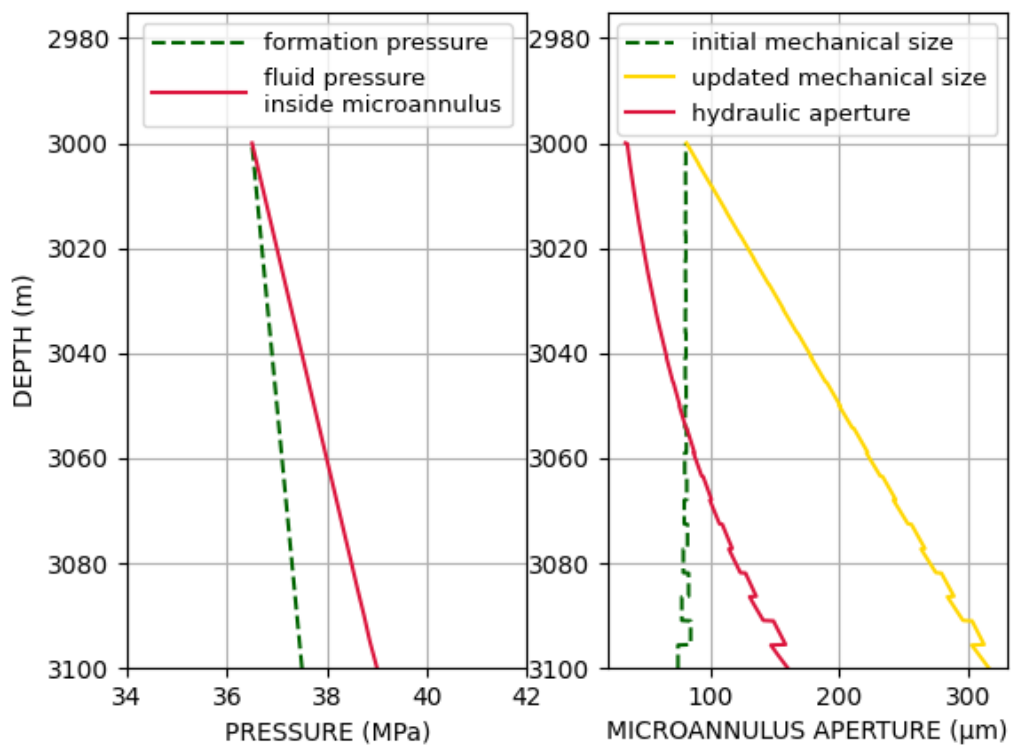


Figure 4.5. The output of the leakage calculator package showing the variation of the internal pressure and microannulus aperture versus depth for the viscous flow – Results related to the outer microannulus

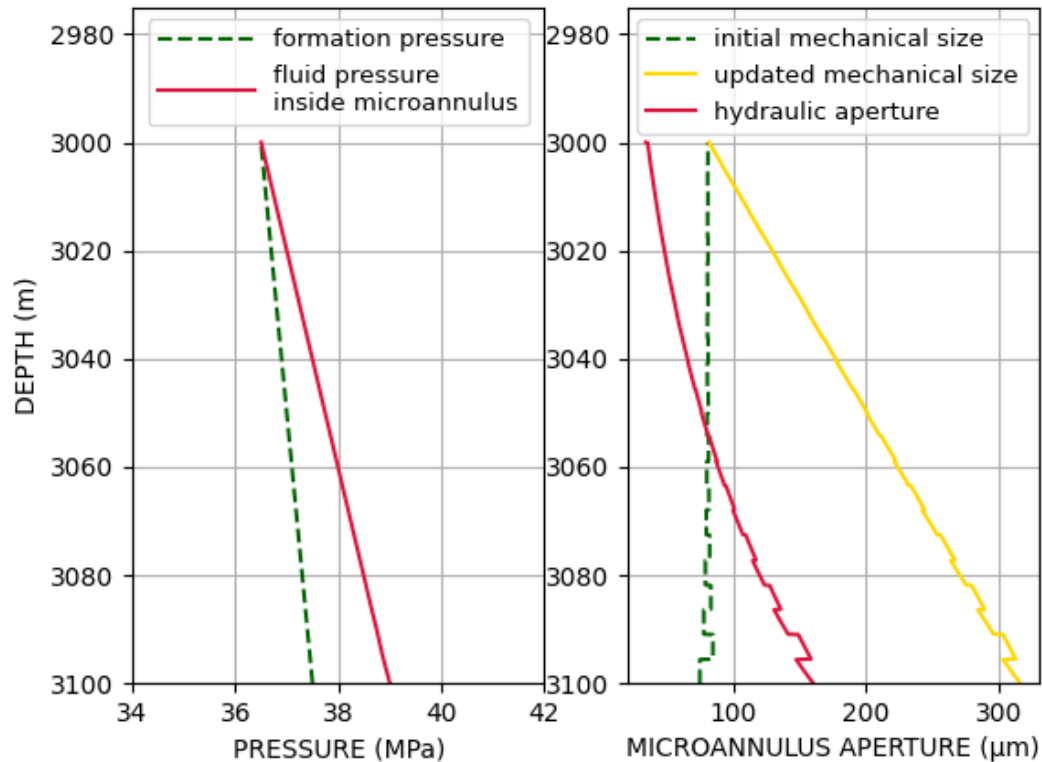


Figure 4.6. The output of the leakage calculator package showing the variation of the internal pressure and microannulus aperture versus depth for the visco-inertial flow – Results related to the outer microannulus

The same calculations as the previous section (for the inner microannulus) are applied in this part according to the aperture values for the outer annular area. Figure 4.7 displays the flow rates bar chart for the Darcy flow. For this series of information, the estimated leakage rate from the calculator package is approximately equal to what would be predicted by the mechanical size average, and approximately sixteen times greater than what would be predicted by the hydraulic size average. The same results for the Non-Darcy flow are shown in Figure 4.8. The value obtained for visco-inertial flow is approximately equal to the rough estimation based on the mean mechanical aperture, and about eleven times larger than the estimation based on the average hydraulic aperture.

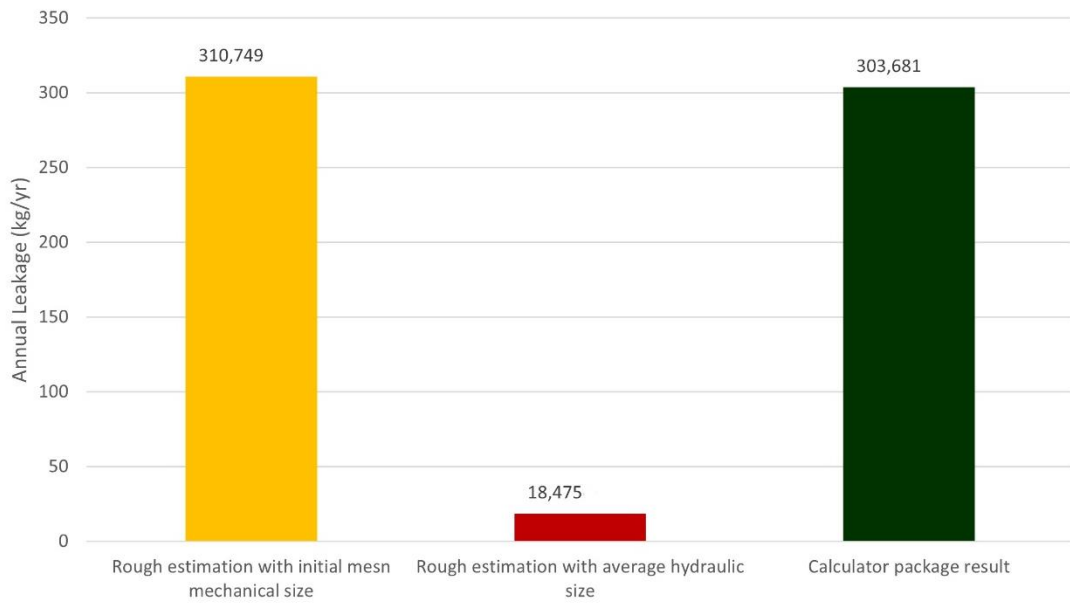


Figure 4.7. Comparison of the annual leakage rates based on the viscous flow calculations - Results related to the outer microannulus

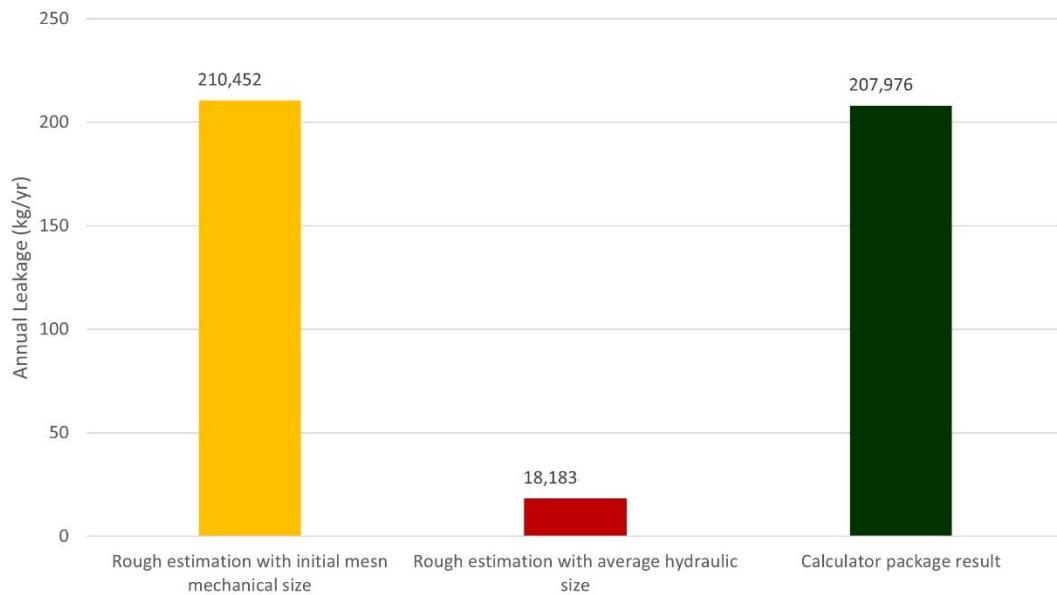


Figure 4.8. Comparison of the annual leakage rates based on the visco-inertial flow calculations - Results related to the outer microannulus

4.2 Sensitivity analysis

In this section a comprehensive sensitivity analysis is developed to investigate the effect of the following parameters on our calculator package results. The values of the Forchheimer number for sections 4.1.1 and 4.1.2 are equal to 1.307 and 0.72, respectively. Therefore, due to the high percentage of the inertial force contribution (about 50% and 41% respectively for these two examples) a visco-inertial behavior is expected for the flow. Therefore, the indicator case (results) to be used for sensitivity evaluations is chosen as: the Non-Darcy package run for the outer microannulus, using the aperture outputs from the last time step of the Abaqus model.

4.2.1 Initial aperture

In order to compare the results both for smaller and larger ranges of mechanical sizes, we multiply the mechanical sizes of our indicator case by 2 (case(a)) and by 0.5 (case(c)) to examine the effects of the aperture range on the package results. Figure 4.9 displays the aperture distribution outputs for all three cases. Table 4.1 shows some important results for a better sense of comparison. Due to the presence of the same pressure values inside the pathway for all cases, the same values of radial displacement are expected in the updated mechanical apertures. Therefore, it appears that for the lower initial apertures, the ratio of the final hydraulic aperture to the initial mechanical aperture is increasing. This results in a greater and more important change in the flow rates for smaller initial apertures (despite the higher absolute flow rate values of larger aperture ranges). Additionally, the difference between mechanical and hydraulic openings exhibits a converging trend along the pathway for the smaller initial apertures. For an average size two times larger, the flow rate is 2.39 times greater, which for our data set means 289 kg more annual emissions. The flow rate of the index case is 1.73 times bigger than for the case (c) (88.426 kg/yr more). Therefore the effect of the size change can significantly change the leakage rate assessment results.

Tab. 4.1: Results of the sensitivity analysis for different initial aperture ranges

Case	Mean initial mechanical aperture	Updated mechanical size in the reservoir top	Mean calculated hydraulic aperture	Flow rate (kg/yr)
(a)	161,32 (μm)	390.69 (μm)	141.58 (μm)	497.888
(b)	80,66 (μm)	315.81 (μm)	84.07 (μm)	207.976
(c)	40,33 (μm)	280.92 (μm)	65.39 (μm)	119.550

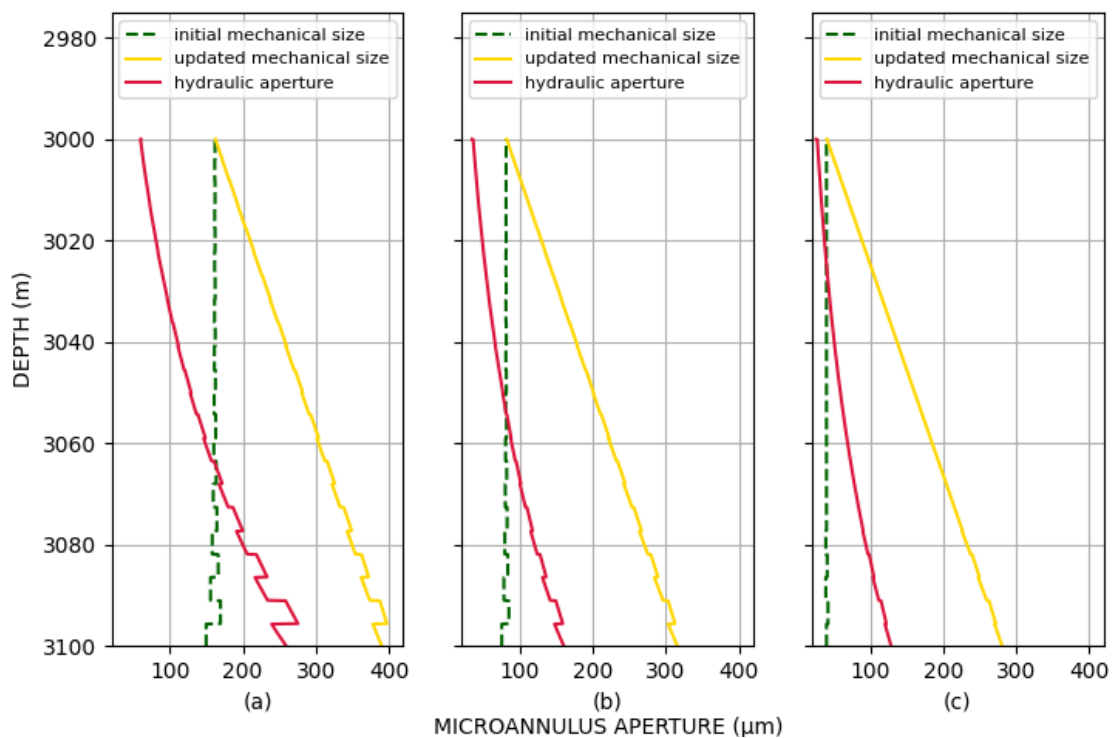


Figure 4.9. Aperture curves, the output of the leakage calculator package for the sensitivity analysis of different initial aperture ranges. (a)-initial mean mechanical aperture equal to 161.32 (μm) – (b)-initial mean mechanical aperture equal to 80.66 (μm) – (c)-initial mean mechanical aperture equal to 40.33(μm)

4.2.2 Initial reservoir pressure

In order to investigate the effect of the initial reservoir pressure value in the leakage assessment, we have developed the comparison between runs for pressure equal to

hydrostatic pressure (37.49 MPa) and two values below and above this pressure. Existence of a positive potential for gas to flow is a very first requirement for the leakage phenomena to occur. Considering the density of the CO₂ in the intended zone, a minimum pressure equal to 37.47 (MPa) is required to have a positive flow potential. Therefore, if the reservoir pressure, during or after injection, will be less than 37.47 (MPa), no leakage rate is expected. Due to this fact, the results of the case (a) for reservoir pressure equal to 37 (MPa) shows a zero flow rate for the leakage in our case. The reservoir pressure equal to 37.49 (MPa) in case (b), with a value very close to the minimum required pressure for flow occurrence, represents a very small leakage rate of 0.474 (kg/yr) as shown in Table 4.2. Figure 4.10 shows the pressure curves along the pathway for these three cases. As it is expected, higher values of fluid pressure entering the annular area, result in wider apertures. Comparing the results mentioned in Table 4.2, for 0.5 (MPa) of pressure increase, the final average size changes from 32.54 (μm) in case (b) to 50.02 (μm) in case (c). It is shown and concluded that for the smaller values of the initial pressure during or after the storage operation, the ratio of the final hydraulic average to the initial mean mechanical size is becoming smaller. In addition, by changing the reservoir pressure a different trend between hydraulic and mechanical values is observed. With regards to the flow rate variation, as indicated in Table 4.2, an increase in pressure leads to an exponential increase in leakage rate values.

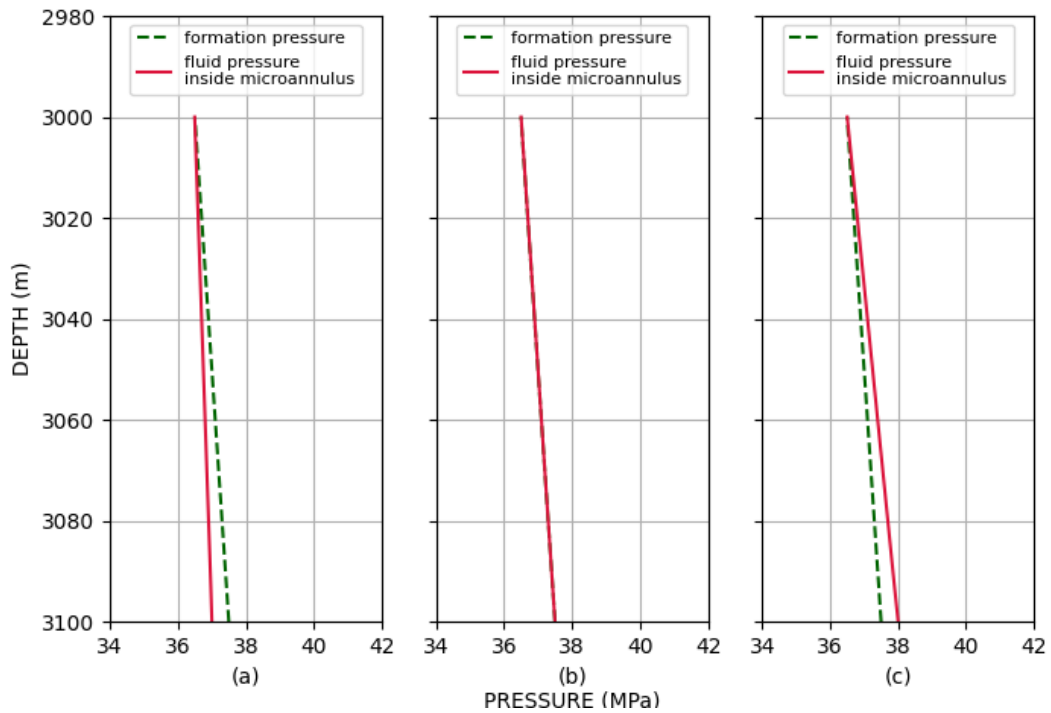


Figure 4.10. Pressure curves, the output of the leakage calculator package for the sensitivity analysis of different reservoir pressures. (a)-reservoir pressure equal to 37 (MPa) – (b)- reservoir pressure equal to 37.49 (MPa) – (c)- reservoir pressure equal to 38 (MPa)

Tab. 4.2: Results of the sensitivity analysis for different initial aperture ranges

Case	Reservoir pressure	Updated mechanical size in the reservoir top	Mean calculated hydraulic aperture	Flow rate (kg/yr)
(a)	37.00 (MPa)	74.88 (μm)	32.54 (μm)	0
(b)	37.49 (MPa)	74.88 (μm)	32.54 (μm)	0.474
(c)	38.00 (MPa)	155.30 (μm)	57.02 (μm)	17.130

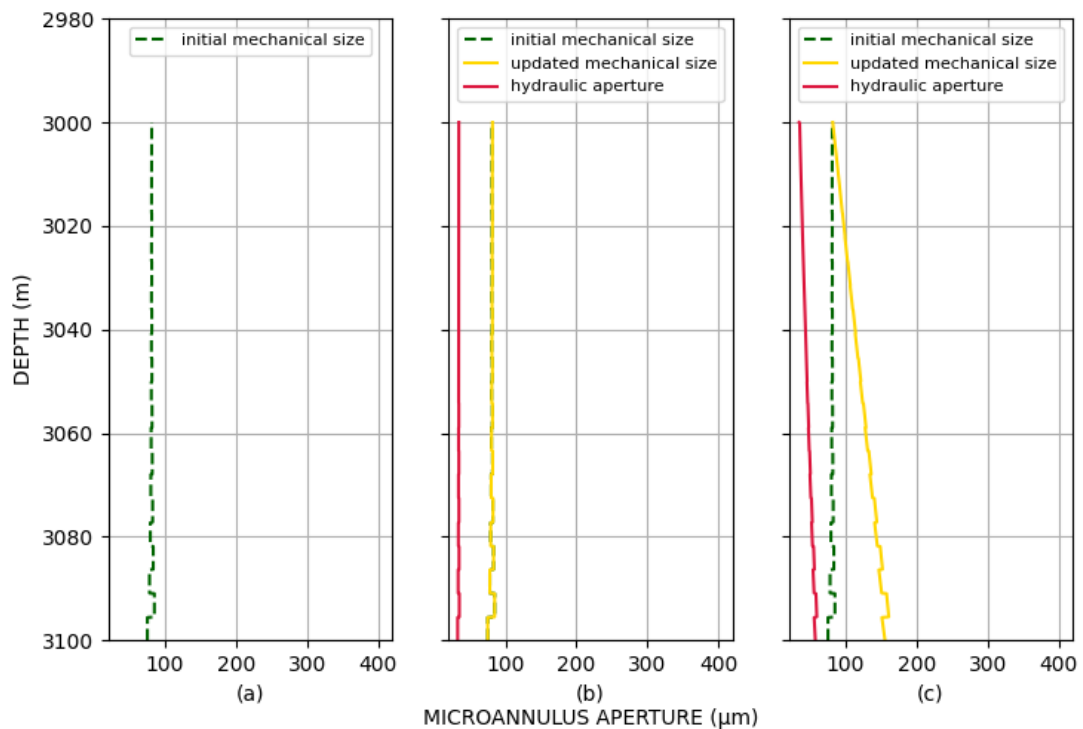


Figure 4.11. Aperture curves, the output of the leakage calculator package for the sensitivity analysis of different reservoir pressures. (a)-reservoir pressure equal to 37 (MPa) – (b)- reservoir pressure equal to 37.49 (MPa) – (c)- reservoir pressure equal to 38 (MPa)

4.2.3 Inertial coefficient

The input value of inertial coefficient (β) in cases (a), (b) and (c) has been considered equal to 6000, 1000 and 600 respectively. The comparison of the outputs, shows a negligible change in pressure and aperture distributions. The variation of this coefficient is just affecting the leakage rates obtained from the Non-Darcy module. Figure 4.12 shows the flow rates calculated for the mentioned cases which indicates a flow rate reduction by increasing the value of (β).

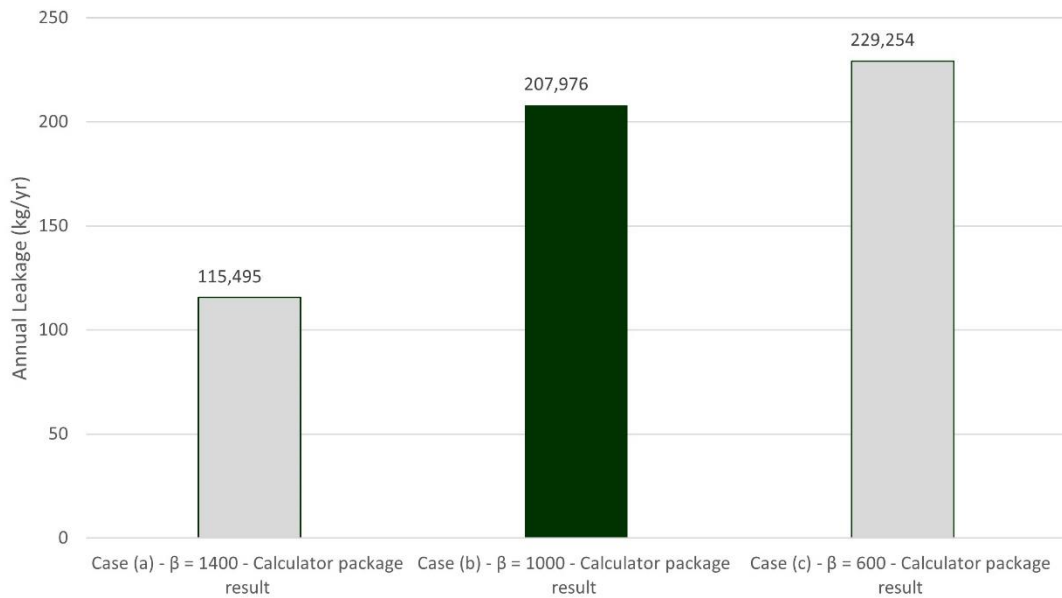


Figure 4.12. Comparison of the annual leakage rates for different values of inertial coefficient

4.2.4 Element size

The sensitivity of the computation process to the element size has been investigated in section 3.2.1 to find the representative grid size in the model. It has been shown previously (Figures 3.7 and 3.8) that flow rate and mean hydraulic aperture are decreasing as elements grow smaller until the stabilization point. The results remain constant for the smaller element sizes after the stabilization (around 1 (m)).

4.2.5 Caprock thickness

Variations in caprock thickness cause almost the same pressure and aperture patterns to spread across a different thickness, changing leakage rates as a result. Figure 4.13 represents the flow rates for three cases with caprock thicknesses equal to 50, 100 and 200 (m). As it is shown, for the thicker caprock layers a smaller leakage rate is expected.

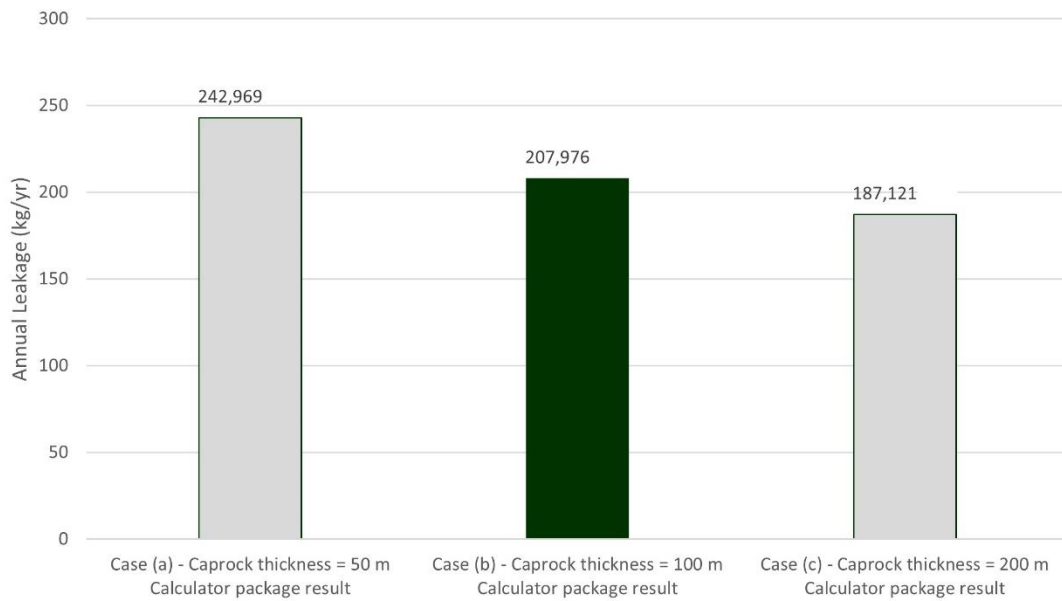


Figure 4.13. Comparison of the annual leakage rates for different values of caprock thickness

4.2.6 Mechanical parameters

4.2.6.1 *Cement properties*

As mentioned in section 3.6, shear modulus and Poisson's ratio of cement are the mechanical properties of this material involved in the computational model.

Considering that cement is present in one side of the annular area for both inner and outer microannuli, the variation of its properties can affect both pathways. Figure 4.14 and Table 4.3 demonstrate the results of the model's sensitivity to the variation of the Poisson's ratio of cement (ν_{cement}). By decreasing the value of (ν_{cement}), the aperture size and flow rate through the pathway are slightly increased.

Tab. 4.3: Results of the sensitivity analysis for different Poisson's ratios of cement

Case	Poisson's ratio of cement	Updated mechanical size in the reservoir top	Mean calculated hydraulic aperture	Flow rate (kg/yr)
(a)	0.15	327.74 (μm)	88.20 (μm)	228.646
(b)	0.20	315.81 (μm)	84.07 (μm)	207.976
(c)	0.25	303.88 (μm)	80.17 (μm)	188.693

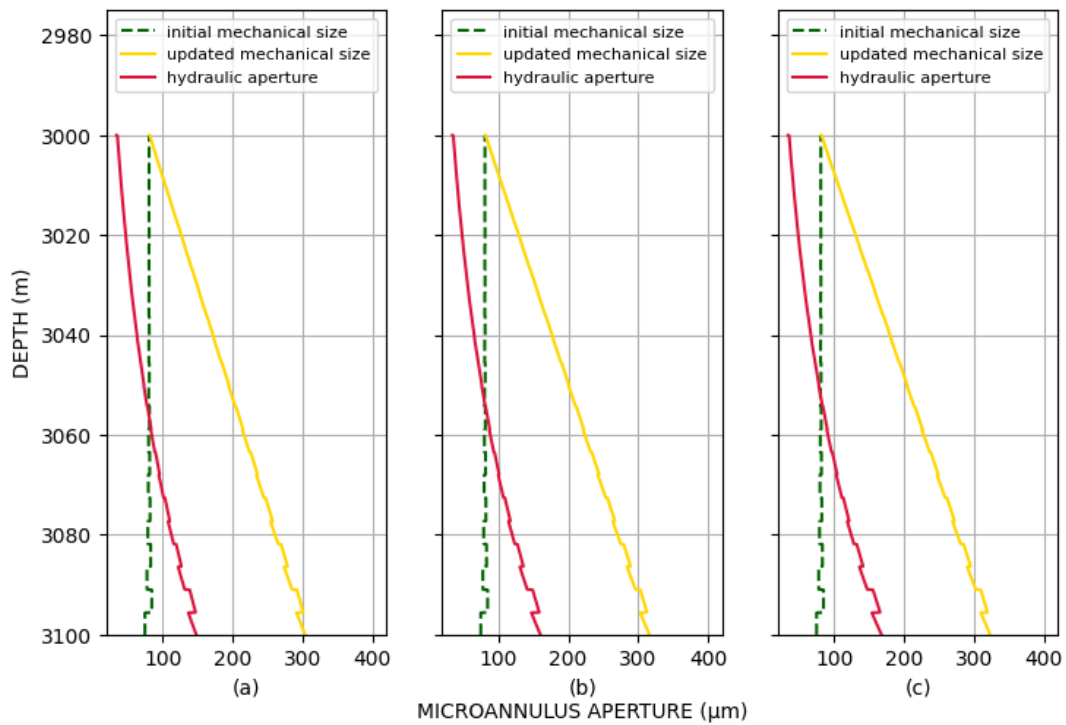


Figure 4.14. Aperture curves, the output of the leakage calculator package for the sensitivity analysis of different ν_{cement} . (a)- ν_{cement} equal to 0.15 – (b)- ν_{cement} equal to 0.2 – (c)- ν_{cement} equal to 0.25

Figure 4.15 and Table 4.4 depict the model's sensitivity to changes in the cement Young's modulus (E). A smaller value of this mechanical parameter for cement results in a partly increase in the aperture size and flow rate.

Tab. 4.4: Results of the sensitivity analysis for different cement Young's modulus

Case	Young's modulus of cement	Updated mechanical size in the reservoir top	Mean calculated hydraulic aperture	Flow rate (kg/yr)
(a)	8160 (MPa)	296.29 (μm)	77.80 (μm)	174.717
(b)	7200 (MPa)	315.81 (μm)	84.07 (μm)	207.976
(c)	6240 (MPa)	341.33 (μm)	93.20 (μm)	250.432

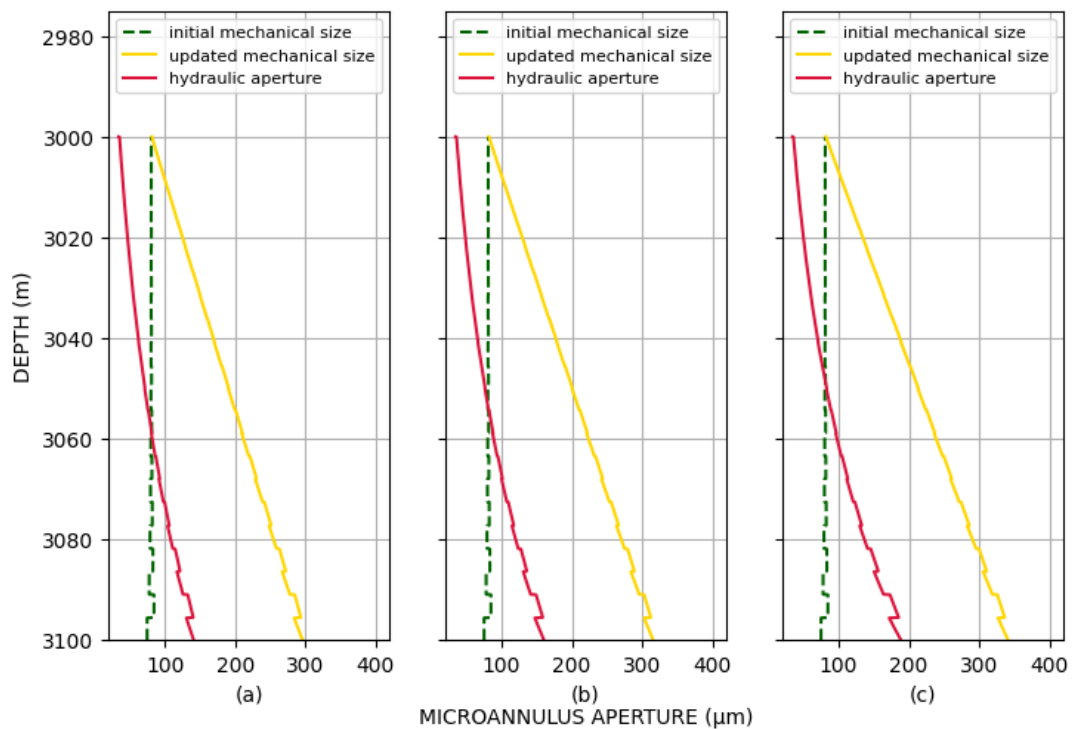


Figure 4.15. Aperture curves, the output of the leakage calculator package for the sensitivity analysis of different Young's modulus of cement. (a)- E_{cement} equal to 8160 (MPa) – (b)- E_{cement} equal to 7200 (MPa) – (c)- E_{cement} equal to 6240 (MPa)

4.2.6.2 Casing properties

Mechanical properties of the casing material can affect the opening of the inner microannulus in our model. Tables 4.5 and 4.6 illustrate the influence of these parameters on the computation results. As it is shown in these tables, due to the high stiffness of the steel material, the radial displacement in the casing side of the annular pathway is negligible in all cases. Therefore there is not an effective change observed in the results by varying these parameters.

Tab. 4.5: Results of the sensitivity analysis for different Poisson's ratio of casing

Case	Poisson's ratio of casing	Updated mechanical size in the reservoir top	Mean calculated hydraulic aperture	Flow rate (kg/yr)
(a)	0.27	315.81 (μm)	84.07 (μm)	207.976
(b)	0.30	315.81 (μm)	84.07 (μm)	207.976
(c)	0.33	315.81 (μm)	84.07 (μm)	207.976

Tab. 4.6: Results of the sensitivity analysis for different casing Young's modulus

Case	Young's modulus of casing	Updated mechanical size in the reservoir top	Mean calculated hydraulic aperture	Flow rate (kg/yr)
(a)	190 (MPa)	315.81 (μm)	84.07 (μm)	207.976
(b)	200 (GPa)	315.81 (μm)	84.07 (μm)	207.976
(c)	210 (MPa)	315.81 (μm)	84.07 (μm)	207.976

4.2.6.3 Formation properties

The shear modulus of the caprock impermeable formation is the only mechanical parameter capable of affecting the size of the outer microannulus. Table 4.7 and Figure 4.16 demonstrate the size and flow rate variation for different values of formation stiffness. For the formation, a smaller value of Young's modulus results in a larger aperture size and increased flow rate.

Tab. 4.7: Results of the sensitivity analysis for different formation Young's modulus

Case	Young's modulus of formation	Updated mechanical size in the reservoir top	Mean calculated hydraulic aperture	Flow rate (kg/yr)
(a)	6000 (MPa)	306.02 (μm)	80.86 (μm)	192.054
(b)	5200 (MPa)	315.81 (μm)	84.07 (μm)	207.976
(c)	4400 (MPa)	329.05 (μm)	88.67 (μm)	231.007

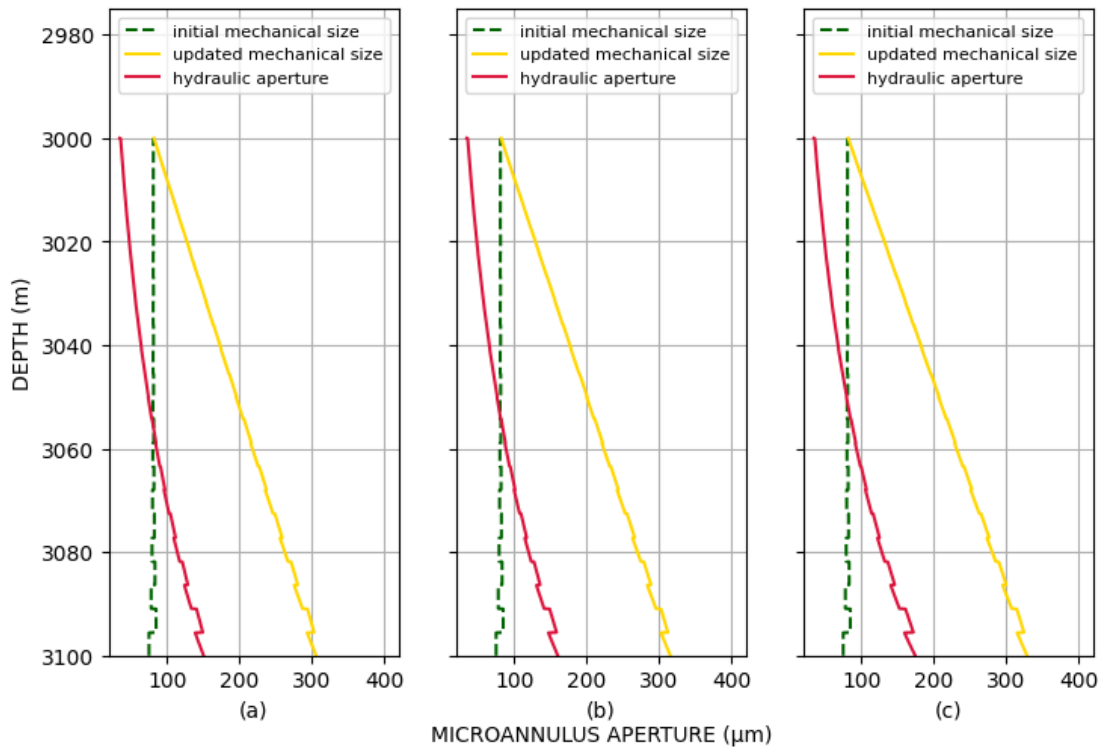


Figure 4.16. Aperture curves, the output of the leakage calculator package for the sensitivity analysis of different Young's modulus of formation. (a)- $E_{\text{formation}}$ equal to 6000 (MPa) – (b)- $E_{\text{formation}}$ equal to 5200 (MPa) – (c)- $E_{\text{formation}}$ equal to 4400 (MPa)

4.2.7 Temperature

Variation of the temperature in the wellbore system for the intended depth does not show a significant impact on the calculator outputs. Three values of 340 (K), 350 (K) and 360 (K) have been applied as the initial temperature for our model. According to the results, the leakage rate slightly increases at the higher temperature (Figure 4.17).

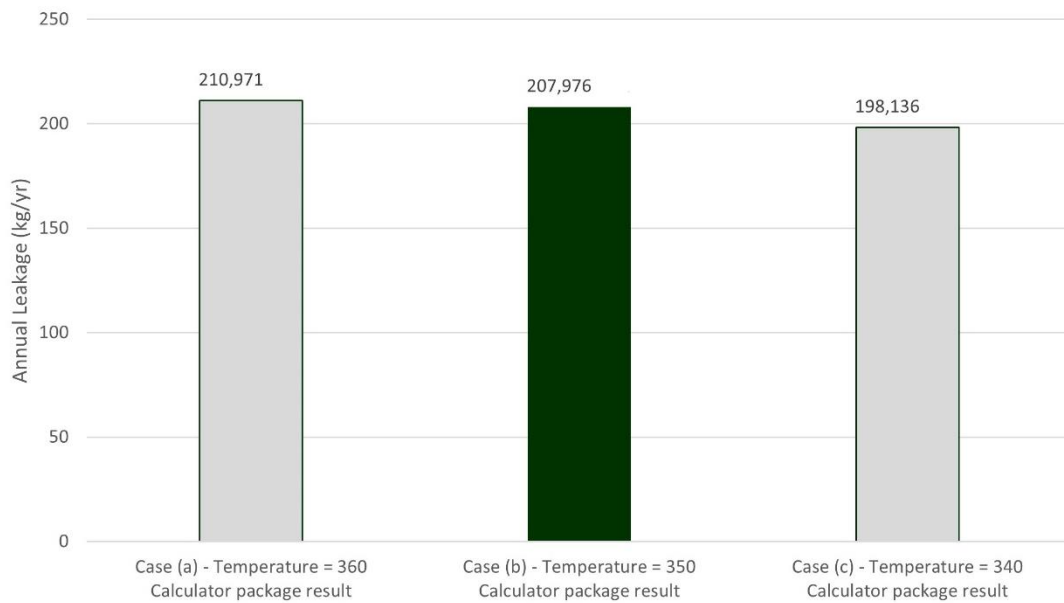


Figure 4.17. Comparison of the annual leakage rates for different values of system temperature

4.3 Two-phase flow results

Two-phase flow of water and CO₂ is included in the model. The presence of these phases results in a multiphase flow behavior which can affect the outputs of the calculations. The amount of this impact can strongly change based on the initial water saturation in the reservoir and the range of the pathway's aperture. In order to evaluate this effect, two different cases have been considered. In the first case, the Darcy module outcomes for the inner microannulus are compared for the single-phase and multiphase

flows. The same comparison is developed for the Non-Darcy module outcomes related to the outer microannulus in the second case.

4.3.1 Inner microannulus – Darcy module

Figure 4.18 (a) shows the saturation distribution in this case along the caprock, obtained from the approach described in section 3.5. As it is shown, in the first case the saturation is varying from 0.25 (reservoir saturation) to 0.1317 at the end of the intended area. Relative permeability behaviors in this range are developed by our defined function (based on the Brooks-Corey model) and are depicted in Figure 4.19 for both phases. According to the results, in both single-phase and multiphase situations, the inner microannulus opens with an aperture of 312.5 (μm) and the average hydraulic aperture calculated by our package, is reduced from 97.37 (μm) to 92.87 (μm) for the multiphase flow. Due to this change in the hydraulic apertures along the pathway (shown in Figure 4.20), a lower leakage rate is obtained with the multiphase flow consideration. The outflow rates for both situations are shown in Figure 4.18 (b).

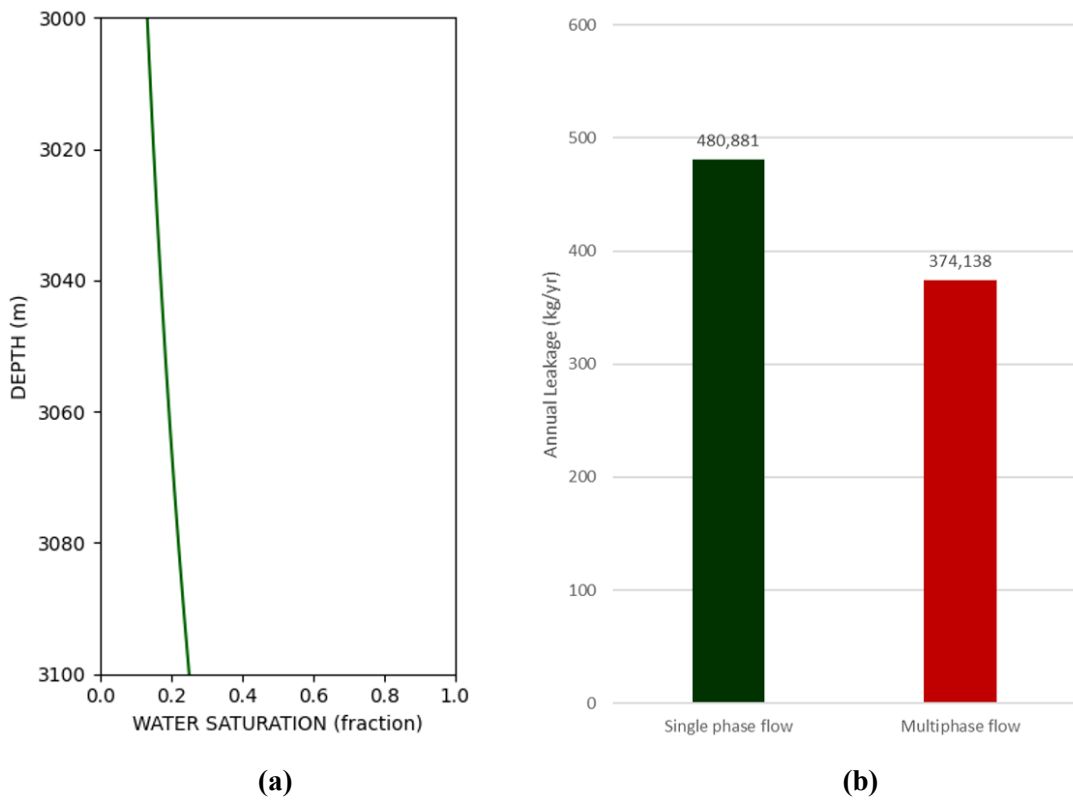


Figure 4.18. (a)- Saturation distribution inside the inner microannulus along the caprock layer – (b)- Comparison of the annual leakage rates for single-phase and multiphase flows

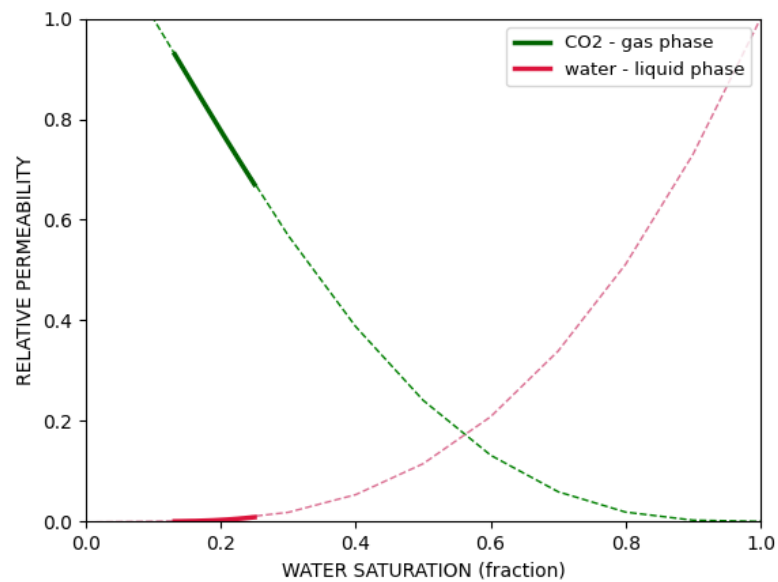


Figure 4.19. Relative permeability curve for water and CO_2 inside the microannulus along the pathway (the applicable range in the intended area is highlighted)

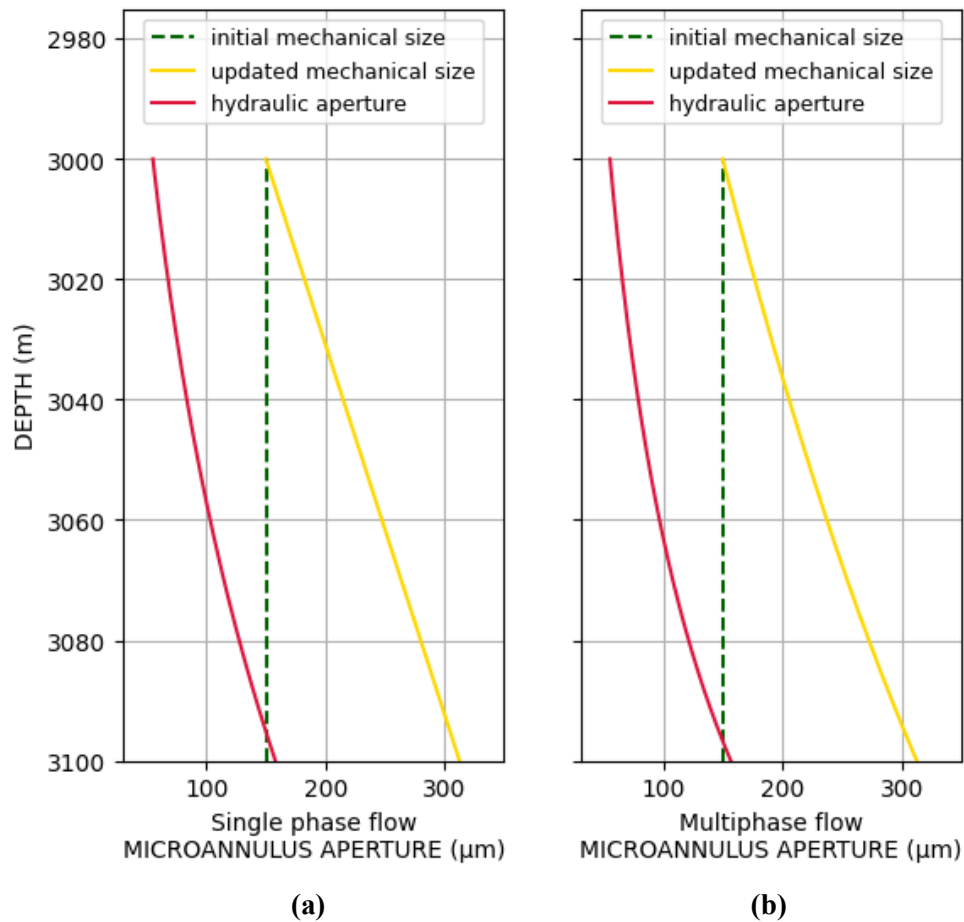


Figure 4.20. Aperture curves, the output of the leakage calculator package for (a)- Single-phase viscous flow inside the inner microannulus – (b)- Multiphase viscous flow inside the inner microannulus

4.3.2 Outer microannulus – Non-Darcy module

the saturation distribution for the second case along the intended pathway is obtained by the method described in section 3.5 and is shown in Figure 4.21 (a) varying from 0.25 (reservoir saturation) to 0.1004. Relative permeabilities are again generated for each element by our defined function (based on the Brooks-Corey model) and have been applied in the flow calculations. Similar to the case number one, both single-phase and multiphase situations result in the same opening sizes in the entrance of the outer

microannulus equal to 315.81 (μm). The average hydraulic aperture calculated by our package, is reduced from 84.07 (μm) to 77.49 (μm) for the multiphase flow in this case. With the multiphase flow consideration, the hydraulic apertures along the leakage path are slightly changed (shown in Figure 4.22) thereby resulting in a lower leakage rate (Figure 4.21 (b)).

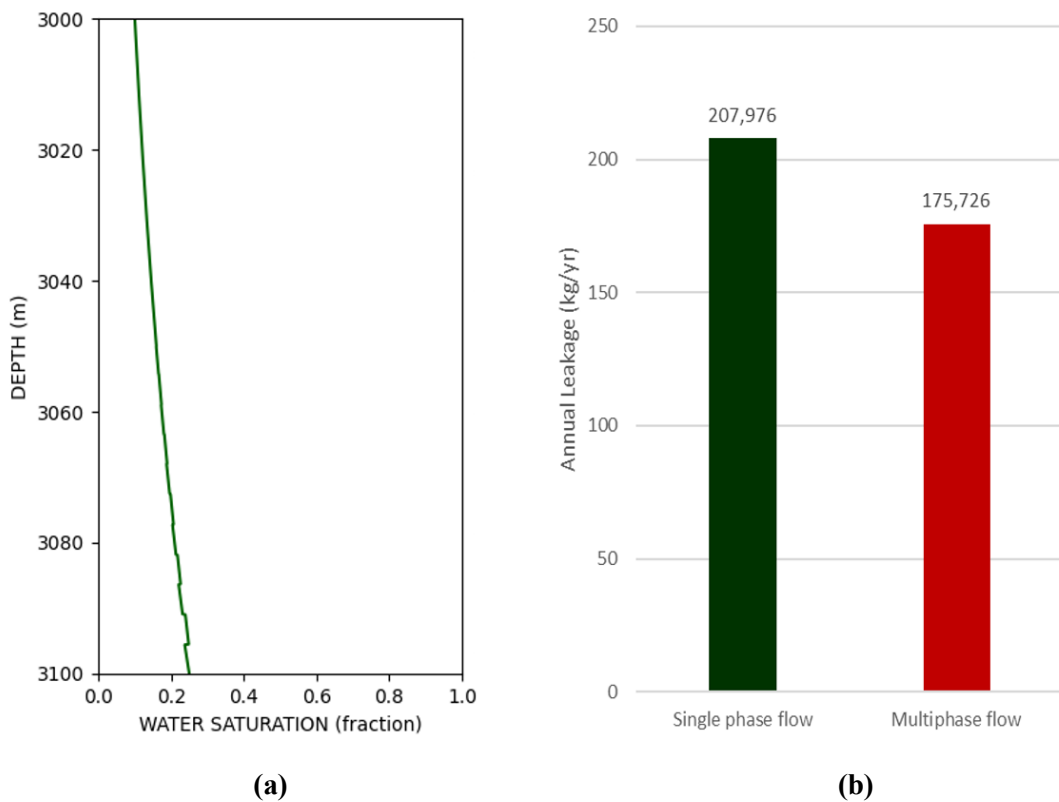


Figure 4.21. (a)- Saturation distribution inside the outer microannulus along the caprock layer – (b)- Comparison of the annual leakage rates for single-phase and multiphase flows

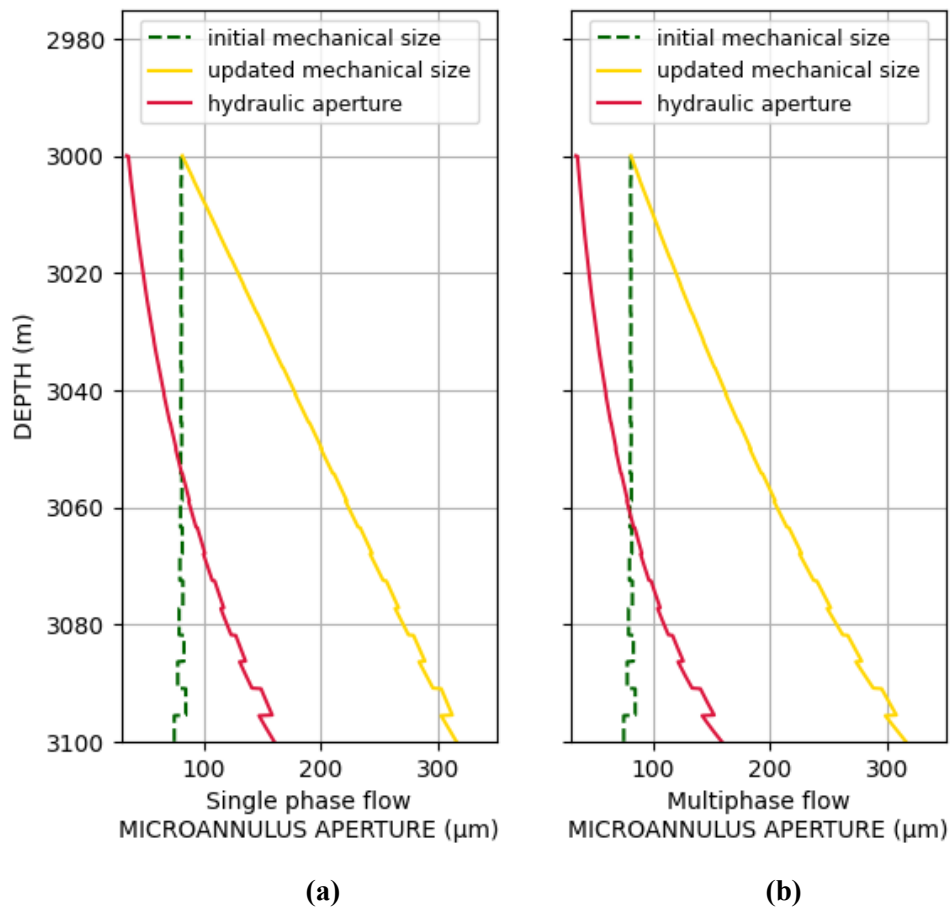


Figure 4.22. Aperture curves, the output of the leakage calculator package for (a)- Single-phase visco-inertial flow inside the outer microannulus – (b)- Multiphase visco-inertial flow inside the outer microannulus

4.4 Entire life-cycle

As mentioned in the literature review, taking the history of the stress distribution around the borehole into consideration to predict the mechanical response of the microannulus, is essential and leads to more reliable outcomes. For this reason, the Abaqus model used in this research contains four stages of the wellbore life-cycle (see section 3.3). In the very last stage (production/injection scenario), a short period in the beginning has been defined as the production time when the pressure drops from the initial value of around 40 (MPa) to 5 (MPa) (representing the reservoir depletion). Then injection of CO₂ is starting at casing pressure equal to 6 (MPa) and this pressure increases linearly over 5 years of injection to 42 (MPa). A microannulus opens in the cement-formation interfaces when the injection begins with the mean mechanical aperture around 210 (μm). Then over 5 years of injection, the stress change closes the microannulus somewhat to about 70 (μm) at the end of the period. Figures 4.23 illustrate the cumulative leakage results in 5 years based on the Abaqus model outputs and Non-Darcy module computations for the annular area between formation and cement. As mentioned in section 4.2.2, a minimum reservoir pressure of 37.47 is required to provide a positive flow potential for CO₂. Therefore, in the first months of the injection (When reservoir pressure is below 37.47), the leakage rate is equal to zero. Then for the pressures bigger than this limit the leakage rate is increasing exponentially in the last months. Figures 4.24 and 4.25 show the changes in leakage flow rate and mean hydraulic aperture over the leaky period in these 5 years.

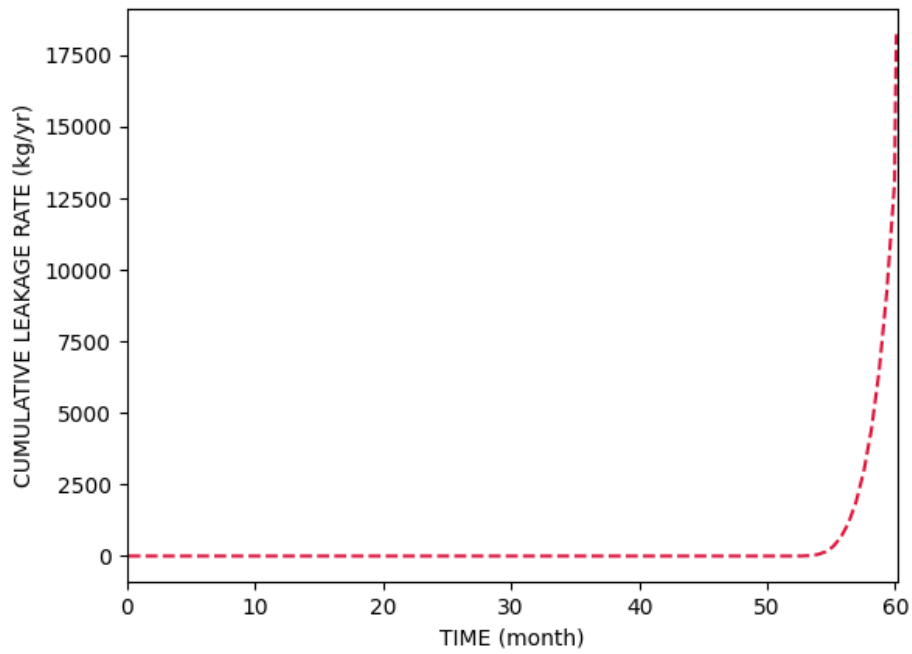


Figure 4.23. Cumulative leakage rate along the outer microannulus over five years of CO₂ injection

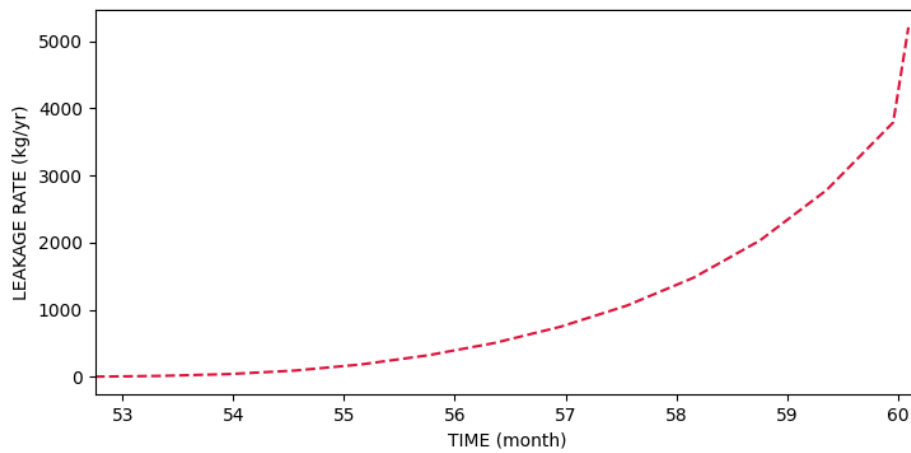


Figure 4.24. Leakage rate variation for the outer microannulus.

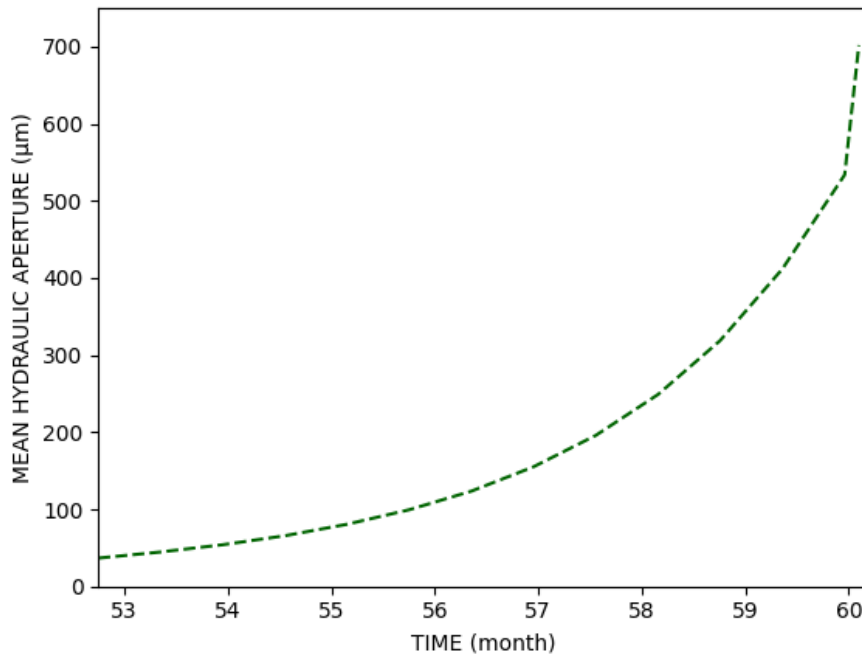


Figure 4.25. Mean hydraulic aperture variation for the outer microannulus along the caprock thickness

4.5 Validity and reliability of the results

In order to assess how reliable are the results in this study, several ranges for pathway permeability (aperture) and leakage flow rates are presented in the following based on the literature. Afterward, the outcomes of this project are compared with these ranges to investigate how they correspond.

Permeability (aperture) ranges:

From the records of gas leakage and pressure buildup or specialized measurements of wellbore permeability, effective wellbore permeabilities range from around 10^{-18} (m^2) to 10^{-12} (m^2) (Crow et al., 2010; Checkai et al., 2013; Stormont et al., 2018). Checkai et al., 2013 also interpreted the microannuli outflow data from 238 wells and concluded that 85% of the hydraulic apertures ranged from 5 to 100 (μm).

Leakage rate ranges:

Tao et al., 2010 indicated that CO₂ outflow rates through the microannuli can vary from 0.1 kg/yr for the slow leakages, up to 1000 kg/yr for the fast ones. Table 4.8 represented by Moghadam et al., 2022 shows the different ranges of leakage rates in several cases.

Tab. 4.8: Summary of the rate measurements at the wellheads of oil and gas wells (Moghadam et al., 2021)

Location	No. of wells	Status	Max leak rate (kg/yr)	Average leak rate (kg/yr)
Pennsylvania, US	19	Abandoned – plugged and unplugged	876	99
West Virginia, US	112	Abandoned – plugged	105	1
West Virginia, US	147	Abandoned - unplugged	1551	27
West Virginia, US	79	Active	28286	1218
US – 4 States	119	Abandoned – plugged	2	0
US – 4 States	19	Abandoned – unplugged	1276	88
Pennsylvania, US	53	Abandoned – unplugged	3066	193
Pennsylvania, US	35	Abandoned – plugged	2540	131
UK	102	Abandoned – plugged	1718	364
Netherlands	29	Abandoned – plugged	3881	135

The leakage rates obtained from our calculator package for several different conditions, show a reasonable range of results considering the ranges noted in this section.

4.6 Risk identification

Despite the fact that microannuli are capable of providing undesirable gas leakage pathways along the wells, their apertures can be too small to be detected as a challenge for the storage failures. It is widely accepted that annual leakage rates of 0.01%,

equivalent to 99% CO₂ retention after one hundred years, are acceptable for ensuring the efficiency of the underground storage operation (Alcalde et al., 2018). [14] If the apertures are large enough to provide outflow rates exceeding the maximum risk limit, some mitigation activities must be implemented.

4.7 Mitigations

In the event that the risk assessment predicts a significant amount of leakage in the desired period, then some mitigation activity must be considered, either before, after or during the storage operation. Some of the effective mitigation methods are indicated in the following.

- Orlic et al., 2021 designed a sensitivity analysis and concluded that adjusting the cement input parameters such as cement stiffness and shrinkage level is an effective way to reduce the risk related to the microannuli leakage and it influences the formation interface more than the casing interface. Based on this study, a cement having lower stiffness and the smallest shrinkage level is the best choice for the well integrity achievement.
- Advanced flexible cement technology is another solution for risk reduction over time in these cases. In this method, using a numerical modelling approach, the expected stress changes over different stages in the well life-cycle will be predicted and the proportionate mechanical properties will be customized for the system based on a particle-size distribution technology. Applying this technique, a mechanical flexibility is obtained which enables the cement system to withstand a variety of changes that may occur through the entire life-cycle of the wellbore (Bellabarba et al., 2008).
- Employing the expanding cement is also one of the most effective mitigation methods to control the outflows in these annular areas. A cement mixture containing expanding agents is capable of filling any gaps and ensuring that it bonds well to the formation and casing on both sides. Due to the hydration and

crystallization of the expanding agents, these cements expand ten times more than a Portland cement slurry with salt. The shear moduli of the rock and the cement play an important role to determine whether the cement will expand only towards the formation or in both directions (Baumgarte et al., 1999).

- The self-healing cement (SHC) technology offered by Schlumberger is formulated by adding self-healing components to the cement. Upon creation of the inner or outer microannuli, these components swell to close the annular gaps without any external intervention (Bellabarba et al., 2008). Underground gas storage (UGS) wells are used both for injection and production operations, meaning they undergo considerable temperature and pressure changes, which can lead to the formation of microannuli. Consequently, self-healing characteristics over time are of special interest in such projects (Bellabarba et al., 2008).

5 CONCLUSION

5.1 Research question

This study aimed to add the effect of the extra fluid pressure inside the microannulus to the computational models in order to achieve a more accurate leakage assessment in underground storage projects. Secondly, the lack of research on multiphase flow within microannuli led us to investigate how two-phase flow is affecting the results.

Regarding the first question, the term extra pressure refers to the difference between real pressure inside the pathway and hydrostatic pressure. In order to answer this question, a comprehensive literature review has been performed to explore the history of the leakage calculator and models. Then a mechanically coupled method has been developed to add the effect of this pressure difference into the calculations. This pressure margin will be preserved along the impermeable caprock layer, which is the intended thickness for this study. We developed a step-wise calculator package which divides the pathway into smaller elements and using the known boundary conditions at the reservoir top, calculates the extra pressure values for the next elements moving upward. In parallel, the radial displacement of the microannulus walls is calculating and updating the change in the aperture as a result of this extra stress at each step. Then the updated sizes are taken into account to calculate the leakage rate through the leakage pathway.

Considering the latter question, an approach was designed to model the water saturation distribution along the pathway based on a dimension-less parameter based on the capillary pressure ratios. In addition a function was defined in the calculator package to compute the relative permeability of the involved phases along the pathway based on the Brook-Corey model, using the referred saturation values. A call to this function is made in each element to calculate the relative permeability value and add it to the flow calculations.

5.2 Key contributions and findings

The lack of the multiphase flow investigation and involving the injection pressure's effect on the leakage pathway (microannuli) opening was encountered during the literature review. Therefore, this research attempted to incorporate these points into the assessments of microannuli leakage. For this reason, the approaches described above have been used and provided a confident range of results based on the validity chapter. The most important findings of this research are outlined in the following:

1. Coupling the numerical Abaqus model with the leakage calculator package by creating a data processing bridge. Modeling tools like Abaqus are powerful tools to model the microannulus creation and openings in the well systems. The aspect not included in this model is the additional fluid pressure inside the microannulus, which will change the aperture calculated by the numerical model or create a pathway in case of higher injection pressures, whereas no microannuli were formed based on the numerical model. In this study a data processing tool is developed that receives the aperture output reports of the Abaqus model, identifies the interface where the annular areas lie, and introduces the mean apertures to our calculator package as the initial mechanical sizes. In this way, the package makes use of the reliable results of the numerical model, fills the two mentioned gaps in the calculations, and reports the updated leakage rates.
2. Adding the option of accounting for the circular non-uniformity of the microannulus around the borehole at each step in the data processing tool. For this purpose, it is grouping the aperture values related to each horizontal slice along the wellbore and calculates the average of the aperture around the circumference for the intended depth. The specific averaging method used for this reason is capable of detecting and taking the non-uniformities into account for the computational model, based on their impact on the flow calculation.

3. Providing a methodology to take the extra pressure inside microannulus into account in the flow and aperture calculations and obtaining the hydraulic aperture, fluid pressure distribution and leakage rate along the pathway as the outputs. The result obtained from this approach has been then compared to the rough estimations based on the boundary conditions (without considering the effect of the extra pressure). The results of these comparisons are as follows:
 - For the inner microannulus (cement-casing interface): the leakage rate predicted by the calculator package for viscous flow is about four times smaller than the estimation based on the mean mechanical aperture and about four times bigger than the rough estimation based on the average hydraulic aperture. For visco-inertial flow, the obtained rate is about two times smaller than the estimation based on the mean mechanical aperture, and about three times bigger than the rough estimation based on the average hydraulic size.
 - For the outer microannulus (cement-formation interface): the estimated leakage rate from the calculator package is approximately equal to what would be predicted by the average mechanical size, and about sixteen times greater than what would be predicted by the average hydraulic size. The value obtained for visco-inertial flow is approximately equal to the rough estimation based on the mean mechanical aperture, and about eleven times larger than the estimation based on the average hydraulic aperture.

In the light of these results, we concluded that this factor in the calculations is important and can have a significant impact on the final leakage estimations. Therefore, it is essential to incorporate it into risk assessments in order to avoid overestimating or underestimating and design an optimum operation.

4. Identification of the most and least effective parameters in the computational model through the sensitivity analysis development using the calculator package. Reservoir pressure value during or after the storage operation has been detected as the most influential parameter in the leakage estimation. Next, it is the initial mechanical size which shows the most impact on the computations. In

case of the visco-inertial flow existence, the calculation results are significantly sensitive to the inertial coefficient value. In order to gain the best estimations, it is therefore necessary for these inputs to be accurately described in each case. The calculation results indicate a weaker sensitivity to other parameters like caprock thickness and mechanical properties. Regarding the mechanical properties of different materials in the system, cement properties are the most effective mechanical parameters in the estimations.

5. Introducing an approach for including multiphase flow consideration into the leakage prediction models through the wellbore microannuli. The result of this tool for viscous flow, the average mechanical size of 150 (μm), reservoir water saturation equal to 0.25 and irreducible water saturation inside the pathway equal to 0.1 shows a 22% reduction in the annual leakage flow rate equal to about 106 kg of CO_2 per year. The same estimation based on the two-phase flow for the visco-inertial flow, the average mechanical size of 80 (μm), reservoir water saturation equal to 0.25 and irreducible water saturation inside the pathway equal to 0.1 implies a 15% reduction in the annual leakage flow rate equivalent to about 32 kg/yr. It should be noted that the level of the multiphase flow impact in the flow calculations, strongly depends on the initial reservoir saturation and the range of the pathway's aperture. Therefore, for the smaller microannuli and higher reservoir water saturations a larger influence is expected.
6. The ability to visualize the leakage assessment for the entire life-cycle of the well system. The leakage calculator package developed in this study is capable of running the model automatically for as many time steps as are available and plotting the cumulative leakage over time. By developing a numerical model over several years of gas injection, we were able to depict the leakage rate over this period.

5.3 Suggestions for future research

We propose several research directions to be pursued in the future:

- Taking into account the multiphase flow applied in our leakage model, the Brooks-Corey model validity in the microannulus has been demonstrated in previous experimental studies, as discussed in the literature. However, laboratory studies are still needed to confirm the reliability and validity of the approach developed for saturation modeling in this research. Moreover, experimental studies on multiphase flow inside microannulus will lead to finding more accurate values for parameters like λ (pore-size distribution index), which will reduce the uncertainty in such computational models.
- A big area of uncertainty in all the microannulus leakage calculators is still the correlation between hydraulic and mechanical aperture that needs more researches confirming or modifying the model used in this study.
- It is recommended to incorporate the tools and methodologies developed in this study in the overall leakage investigations, since leakage pathways are likely to be comprised of microannuli, shear cracks, radial cracks, cement channels, and uncemented segments.

References

- Aas, B., Sørbo, J., Stokka, S., Drillwell, I., Saasen, A., Norske, D., Rune, O., Statoil, G., Lunde, Ø., Phillips, C., & Vrålstad, T. (2016). Cement Placement with Tubing Left in Hole during Plug and Abandonment Operations. *IADC/SPE-178840-MS*
- Agnaou, M., Lasseux, D., & Ahmadi, A. (2017). Origin of the inertial deviation from Darcy's law: An investigation from a microscopic flow analysis on two-dimensional model structures. *Physical Review E*, 96(4). <https://doi.org/10.1103/PhysRevE.96.043105>
- Ajayi, T., Gomes, J. S., & Bera, A. (2019). A review of CO₂ storage in geological formations emphasizing modeling, monitoring and capacity estimation approaches. *China University of Petroleum Beijing*. <https://doi.org/10.1007/s12182-019-0340-8>
- Akhavan, A., Shafaatian, S. M. H., & Rajabipour, F. (2012). Quantifying the effects of crack width, tortuosity, and roughness on water permeability of cracked mortars. *Cement and Concrete Research*, 42(2), 313–320. <https://doi.org/10.1016/j.cemconres.2011.10.002>
- Alcalde, J., Flude, S., Wilkinson, M., Johnson, G., Edlmann, K., Bond, C. E., Scott, V., Gilfillan, S. M. V., Ogaya, X., & Stuart Haszeldine, R. (2018). Estimating geological CO₂ storage security to deliver on climate mitigation. *Nature Communications*. <https://doi.org/10.1038/s41467-018-04423-1>
- Anwar, I., Chojnicki, K., Bettin, G., Taha, M. R., & Stormont, J. C. (2019). Characterization of wellbore casing corrosion product as a permeable porous medium. *Journal of Petroleum Science and Engineering*, 180, 982–993. <https://doi.org/10.1016/j.petrol.2019.05.087>
- Bachu, S., & Bennion, D. B. (2009). Experimental assessment of brine and/or CO₂ leakage through well cements at reservoir conditions. *International Journal of Greenhouse Gas Control*, 3(4), 494–501. <https://doi.org/10.1016/j.ijggc.2008.11.002>
- Baumgarte, C., Thiercelin, M., & Klaus, D., (1999). Case Studies of Expanding Cement To Prevent Microannular Formation. *SPE & Schlumberger Dowell*. <http://onepetro.org/SPEATCE/proceedings-pdf/99ATCE/All-99ATCE/SPE-56535-MS/1920119/spe-56535-ms.pdf/1>
- Bear, J., (1972). Dynamics of fluids in Porous Media. *American Elsevier, New York, N.Y., and Amsterdam*.
- Bellabarba, M., Bulte-Loyer, H., Froelich, B., Roy-Delage, S.L., Kuijk, R., Zeroug, S. (2008). Ensuring zonal isolation beyond the life of the well. *Multi-physics measurements inversions and interpretations for O&G reservoir characterization View project Self-healing cement CO₂ View project*. <https://www.researchgate.net/publication/288046715>
- Benge, G. (2005). Cement Designs for High-Rate Acid Gas Injection Wells. *IPTC 10608*
- Berkowitz, B. (2002). Characterizing flow and transport in fractured geological media: A review. www.elsevier.com/locate/advwatres
- Bois, A.-P., Garnier, A., & Rodot, F. (2011). How To Prevent Loss of Zonal Isolation Through a Comprehensive Analysis of Microannulus Formation.
- Bois, A.-P., Garnier, A., Gory Galdiolo, G., Benoit, J.-B., & Total, S. A. (2012). Use of a Mechanistic Model To Forecast Cement-Sheath Integrity.
- Bois, A. P., Vu, M. H., Noël, K., Badalamenti, A., Delabroy, L., Théron, E., & Hansen, K. (2019). Evaluating cement-plug mechanical and hydraulic integrity. *SPE Drilling and Completion*, 43(2), 92–102. <https://doi.org/10.2118/191335-PA>

- Boukhelifa, L., Moroni, N., James, S.G., Le Roy-Delage, S., & Thiercelin, M.J., (2004). Evaluation of Cement Systems for Oil and Gas Well Zonal Isolation in a Full-Scale Annular Geometry. *SPE, ENI SpA, Schlumberger & INSA Toulouse*
- Brooks, R. H., & Corey, A. T. (1964). *Hydraulic Properties of Porous Media*.
- Carey, J. W., Wigand, M., Chipera, S. J., WoldeGabriel, G., Pawar, R., Lichtner, P. C., Wehner, S. C., Raines, M. A., & Guthrie, G. D. (2007). Analysis and performance of oil well cement with 30 years of CO₂ exposure from the SACROC Unit, West Texas, USA. *International Journal of Greenhouse Gas Control*, 1(1), 75–85. [https://doi.org/10.1016/S1750-5836\(06\)00004-1](https://doi.org/10.1016/S1750-5836(06)00004-1)
- Carroll, S. A., Iyer, J., & Walsh, S. D. C. (2017). Influence of Chemical, Mechanical, and Transport Processes on Wellbore Leakage from Geologic CO₂ Storage Reservoirs. *Accounts of Chemical Research*, 50(8), 1829–1837. <https://doi.org/10.1021/acs.accounts.7b00094>
- Chadwick, R. A., Zweigel, P., Gregersen, U., Kirby, G. A., Holloway, S., & Johannessen, P. N. (2004). Geological reservoir characterization of a CO₂ storage site: The Utsira Sand, Sleipner, northern North Sea. <https://doi.org/10.1016/j.energy.2004.03.071>
- Checkai, D., Bryant, S., & Tao, Q. (2013). Towards a frequency distribution of effective permeabilities of leaky wellbores. *Energy Procedia*, 37, 5653–5660. <https://doi.org/10.1016/j.egypro.2013.06.487>
- Chen, Y. F., Zhou, J. Q., Hu, S. H., Hu, R., & Zhou, C. B. (2015). Evaluation of Forchheimer equation coefficients for non-Darcy flow in deformable rough-walled fractures. *Journal of Hydrology*, 529, 993–1006. <https://doi.org/10.1016/j.jhydrol.2015.09.021>
- Corina, A. N., Skorpa, R., Sangesland, S., & Vrålstad, T. (2021). Simulation of fluid flow through real microannuli geometries. *Journal of Petroleum Science and Engineering*, 196. <https://doi.org/10.1016/j.petrol.2020.107669>
- Crow, W., Carey, J. W., Gasda, S., Brian Williams, D., & Celia, M. (2010). Wellbore integrity analysis of a natural CO₂ producer. *International Journal of Greenhouse Gas Control*, 4(2), 186–197. <https://doi.org/10.1016/j.ijggc.2009.10.010>
- de Andrade, J. (2014). Influence of Casing Centralization on Cement Sheath Integrity During Thermal Cycling. In *Technology*. NTNU. *IADC/SPE 168012*
- de Andrade, J., Sangesland, S., Skorpa, R., Todorovic, J., & Vrålstad, T. (2016). Experimental laboratory setup for visualization and quantification of cement-sheath integrity. *SPE Drilling and Completion*, 31(4), 317–326. <https://doi.org/10.2118/173871-PA>
- Do Quang, K., Tam, T. N. T., Kieu, P., Huynh, N. V., & Trong, Q. H. (2020). Modelling stress distribution around boreholes. in *Civil Engineering*. https://doi.org/10.1007/978-981-15-0802-8_122
- Dusseault, M. B., Jackson, R. E., & Macdonald, D. (2014). Towards a Road Map for Mitigating the Rates and Occurrences of Long-Term Wellbore Leakage.
- Feng, Y., Li, X., & Gray, K. E. (2017). Development of a 3D numerical model for quantifying fluid-driven interface debonding of an injector well. *International Journal of Greenhouse Gas Control*, 62, 76–90. <https://doi.org/10.1016/j.ijggc.2017.04.008>
- Ford, E. P., Moeinikia, F., Hans, U. ;, Lohne, P., Arild, Ø., Majoumerd, M. M., Kjell, I. ;, & Fjelde, K. (2017). *Leakage Calculator for Plugged and Abandoned Wells*. *SPE-185890-MS*
- Fourar, M., Bories, S., & Persoff, P. (1993). Two-Phase Flow in Smooth and Rough Fractures' Measurement and Correlation by Porous-Medium and Pipe Flow Models. In *WATER RESOURCES RESEARCH (Vol. 29, Issue 11)*.

- Garcia Fernandez, S., & Fernandez, G. (2018). Characterization of wellbore microannuli. *University of New Mexico*. https://digitalrepository.unm.edu/ce_etds
- Garcia Fernandez, S., Matteo, E. N., Taha, M. R., & Stormont, J. C. (2019). Characterization of wellbore microannuli. *Journal of Natural Gas Science and Engineering*, 62, 13–25. <https://doi.org/10.1016/j.jngse.2018.12.003>
- Garcia Fernandez, S., Anwar, I., Reda Taha, M. M., Stormont, J.C. Matteo, E.N. (2020). Two-phase flow properties of a wellbore microannulus. *Department of Civil Engineering, University of New Mexico, Albuquerque, NM, USA & Sandia National Laboratories, Albuquerque, NM, USA*.
- Gasda, S. E., Bachu, S., & Celia, M. A. (2004). Spatial characterization of the location of potentially leaky wells penetrating a deep saline aquifer in a mature sedimentary basin. *Environmental Geology*, 46(6–7), 707–720. <https://doi.org/10.1007/s00254-004-1073-5>
- Gomez, S. P., Sobolik, S. R., Matteo, E. N., Reda Taha, M., & Stormont, J. C. (2017). Investigation of wellbore microannulus permeability under stress via experimental wellbore mock-up and finite element modeling. *Computers and Geotechnics*, 83, 168–177. <https://doi.org/10.1016/j.compgeo.2016.10.001>
- Goodwin, K. (1992). Cement Sheath Stress Failure.
- Grandi, S., Rao, R., & Nafi Toksöz, M. (2002). Geomechanical Modeling of In-Situ Stresses Around a Borehole. *Earth Resources Laboratory, Department of Earth, Atmospheric, and Planetary Sciences, Massachusetts Institute of Technology, Cambridge, MA 02139*
- Gray K.E., Podnos E., & Becker E. (2007). Finite Element Studies of Near-Wellbore Region During Cementing Operations: Part I. *University of Texas at Austin*
- Gu, J., Zhong, P., Shao, C., Bai, S., Zhang, H., & Li, K. (2012). Effect of interface defects on shear strength and fluid channeling at cement-interlayer interface. *Journal of Petroleum Science and Engineering*, 100, 117–122. <https://doi.org/10.1016/j.petrol.2012.11.021>
- Hatambeigi, M., Chojnicki, K., Reda Taha, M., & Stormont, J. C. (2020). Visco-inertial gas flow through wellbore cement fractures; Visco-inertial gas flow through wellbore cement fractures. *University of New Mexico, Albuquerque, NM, United States & Sandia National Laboratories, Albuquerque, NM, United States*
- Hatzignatiou, D. G. (1996). Determination of Effective or Relative Permeabilities From Well Tests. *SPE 20537*
- Hawkes, C. D., McLellan, P. J., & Bachu, S. (2005). Geomechanical Factors Affecting Geological Storage of CO₂ in Depleted Oil and Gas Reservoirs. *Journal of Canadian Petroleum Technology*, 44(10), 52–61. <https://doi.org/10.2118/05-10-05>
- Huang, X., Zhang, L., Zhang, R., Chen, X., Zhao, Y., & Yuan, S. (2021). Numerical simulation of gas-liquid two-phase flow in the micro-fracture networks in fractured reservoirs. *Journal of Natural Gas Science and Engineering*, 94. <https://doi.org/10.1016/j.jngse.2021.104101>
- Huerta, N. J., Checkai, D. A., & Bryant, S. L. (2009). Utilizing Sustained Casing Pressure Analog to Provide Parameters to Study CO₂ Leakage Rates Along a Wellbore. *SPE 126700*
- Humez, P., Audigane, P., Lions, J., Chiaberge, C., Bellenfant, G., & Bellenfant, G. (2011). Modeling of CO₂ Leakage up Through an Abandoned Well from Deep Saline Aquifer to Shallow Fresh Ground-waters. <https://doi.org/10.1007/s11242-011>
- Jackson, P. (1993). Effect of Casing Pressure on Gas Flow Through a Sheath of Set Cement.

- Javadi, M., Sharifzadeh, M., Shahriar, K., & Mitani, Y. (2014). Critical Reynolds number for non-linear flow through rough-walled fractures: The role of shear processes. *Water Resources Research*, 50(2), 1789–1804. <https://doi.org/10.1002/2013WR014610>
- Lackey, G., Vasylykivska, V. S., Huerta, N. J., King, S., & Dilmore, R. M. (2019). Managing well leakage risks at a geologic carbon storage site with many wells. *International Journal of Greenhouse Gas Control*, 88, 182–194. <https://doi.org/10.1016/j.ijggc.2019.06.011>
- Lavrov, A. (2018). Stiff cement, soft cement: Nonlinearity, arching effect, hysteresis, and irreversibility in CO₂-well integrity and near-well geomechanics. *International Journal of Greenhouse Gas Control*, 70, 236–242. <https://doi.org/10.1016/j.ijggc.2017.11.012>
- Lecampion, B., Quesada, D., Loizzo, M., Bungler, A., Kear, J., Deremble, L., & Desroches, J. (2011). Interface debonding as a controlling mechanism for loss of well integrity: Importance for CO₂ injector wells. *Energy Procedia*. <https://doi.org/10.1016/j.egypro.2011.02.500>
- Lecampion, B., Bungler, A., Kear, J., & Quesada, D. (2013a). Interface debonding driven by fluid injection in a cased and cemented wellbore: Modeling and experiments. *International Journal of Greenhouse Gas Control*, 18, 208–223. <https://doi.org/10.1016/j.ijggc.2013.07.012>
- Li, M., Bi, G., Shi, Y., & Zhao, K. (2022). A semi-analytical two-phase flow model of fractured horizontal well with complex fracture networks in natural fractured reservoirs. *Energy Exploration and Exploitation*, 40(1), 174–192. <https://doi.org/10.1177/01445987211041782>
- Maloney, D., & Doggett, K. (1997). *Multiphase Flow in Fractures*.
- Malvern, L. E. (1969). *INTRODUCTION TO THE MECHANICS OF A CONTINUOUS MEDIUM*.
- Matteo, E. N., Stormont, J. C., & Stenko, M. (2019). Monitoring and Repair of Cement-Geomaterial Interfaces in Borehole and Repository Scenarios. *Sandia National Laboratories, Albuquerque, NM, USA*. <https://classic.nts.gov/help/order-methods/>
- Matteo, E. N., Verzi, S., Bauer, S. J., Pyrak-Nolte, L. J., Reda Taha, M. M., & Stormont, J. C. (2021). SANDIA REPORT Advanced Detection of Wellbore Failure for Safe and Secure Utilization of Subsurface Infrastructure . *Sandia National Laboratories, Albuquerque, NM, United States*
- Mei, C. C., & Auriault, J.L. (1991). The effect of weak inertia on flow through a porous medium. In *J. Fluid Mech* (Vol. 222).
- Moghadam, A., Corina, A.N., 2022. Modelling stress evolution in cement plugs during hydration. In *Proceedings of the 56th US Rock Mechanics / Geomechanics Symposium (ARMA), June 26-29, Santa Fe, New Mexico. ARMA 22-0966*.
- Moghadam, A., Orlic, B., 2021. Estimation of initial cement stress in wells. In *Proceedings of the 55th US Rock Mechanics / Geomechanics Symposium (ARMA), June 21-25, Houston, Texas. ARMA 21-1230*.
- Moghadam, A., Castelein, K., ter Heege, J., & Orlic, B. (2022). A study on the hydraulic aperture of microannuli at the casing–cement interface using a large-scale laboratory setup. *Geomechanics for Energy and the Environment*. <https://doi.org/10.1016/j.gete.2021.100269>
- Nagelhout, A., Brunei, S., Bosma, M., Mul, P., Krol, G., van Velzen, J., Joldersma, J., James, S., Dargaud, B., Schreuder, G., & Théry, F. (2010). Laboratory and Field Validation of a Sealant System for Critical Plug-and-Abandon Situations.
- Orlic, B. (2009). Some geomechanical aspects of geological CO₂ sequestration. *KSCE Journal of Civil Engineering*, 13(4), 225–232. <https://doi.org/10.1007/s12205-009-0225-2>

- Orlic, B., Moghadam, A., Brunner, L., van Unen, M., Wojcicki, A., Bobek, K., van der Valk, K., Wollenweber, J., 2021. A Probabilistic Well Integrity Analysis Workflow for Leakage Risk Assessment: Case Studies for Shale Gas and Re-Use for CCS. *In Proceedings of the 15th Greenhouse Gas Control Technologies Conference 2020 (GHGT-15), March 16-21, UAE.*
- Picandet, V., Khelidj, A., & Bellegou, H. (2009). Crack effects on gas and water permeability of concretes. *Cement and Concrete Research*, 39(6), 537–547. <https://doi.org/10.1016/j.cemconres.2009.03.009>
- Ranjith, P. G., & Darlington, W. (2007). Nonlinear single-phase flow in real rock joints. *Water Resources Research*, 43(9). <https://doi.org/10.1029/2006WR005457>
- Ravi, K., Bosma, M., International, S. E., & Gastebled, O. (1999). Safe and Economic Gas Wells through Cement Design for Life of the Well.
- Rocha-Valadez, T., Hasan, A. R., Mannan, S., & Kabir, C. S. (2014). Assessing wellbore integrity in sustained-casing-pressure annulus. *SPE Drilling and Completion*, 29(1), 131–138. <https://doi.org/10.2118/169814-PA>
- Roy, P., Morris, J. P., Walsh, S. D. C., Iyer, J., & Carroll, S. (2018). Effect of thermal stress on wellbore integrity during CO₂ injection. *International Journal of Greenhouse Gas Control*, 77, 14–26. <https://doi.org/10.1016/j.ijggc.2018.07.012>
- Seidel F.A. Use of Expanding Cement Improves Bonding and Aids in Eliminating Annular Gas Migration in Hobbs Grayburg-San Andres Wells. *Amoco Production Co., and T.G. Greene, Dowell Schlumberger.*
- Shad, S., & Gates, I. D. (2010). Multiphase Flow in Fractures: Co-Current and Counter-Current Flow in a Fracture. *Journal of Canadian Petroleum Technology*.
- Shi, Y., Guo, B., Guan, Z., Xu, Y., & Zhang, B. (2017). Influence of the initial loaded state on the stress distribution of a wellbore system. *Journal of Petroleum Science and Engineering*, 157, 547–557. <https://doi.org/10.1016/j.petrol.2017.07.054>
- Sivila, L. J. (2013). A Petrophysical Evaluation of Capillary Pressure for a Naturally Fractured Tight Gas Sandstone Reservoir: a Case Study.
- Skorpa, R., & Vrålstad, T. (2018). Visualization of fluid flow through cracks and microannuli in cement sheaths. *SPE Journal*, 23(4), 1067–1074. <https://doi.org/10.2118/180019-pa>
- Stormont, J. C., Fernandez, S. G., Taha, M. R., & Matteo, E. N. (2018). Gas flow through cement-casing microannuli under varying stress conditions. *Geomechanics for Energy and the Environment*, 13, 1–13. <https://doi.org/10.1016/j.gete.2017.12.001>
- Tao, Q., Checkai, D., & Bryant, S. L. (2010). Permeability Estimation for Large-Scale Potential CO₂ Leakage Paths in Wells Using a Sustained-Casing-Pressure Model. *SPE 139576*.
- Tao, Q., Checkai, D., Huerta, N., & Bryant, S. L. (2011). An improved model to forecast CO₂ leakage rates along a wellbore. *Energy Procedia*, 4, 5385–5391. <https://doi.org/10.1016/j.egypro.2011.02.522>
- Tao, C., Rosenbaum, E., Kutchko, B. G., & Massoudi, M. (2021). A brief review of gas migration in oilwell cement slurries. *In Energies*. <https://doi.org/10.3390/en14092369>
- Tardy, P. M. J. (2018). A 3D model for annular displacements of wellbore completion fluids with casing movement. *Journal of Petroleum Science and Engineering*, 162, 114–136. <https://doi.org/10.1016/j.petrol.2017.11.071>
- Tavassoli, S., Ho, J. F., Shafiei, M., Huh, C., Bommer, P., Bryant, S., & Balhoff, M. T. (2018). An experimental and numerical study of wellbore leakage mitigation using pH-triggered polymer gelant. *Fuel*, 217, 444–457. <https://doi.org/10.1016/j.fuel.2017.12.098>

- Therond, E., Bois, A. P., Whaley, K., & Murillo, R. (2017). Large-scale testing and modeling for cement zonal isolation in water-injection wells. *SPE Drilling and Completion*, 32(4), 290–300. <https://doi.org/10.2118/181428-pa>
- Thiercelin, M. J., Dargaud, B., Baret, J. F., Dowell, W. J., & Rodriguez, I. S. A. (1998). Cement Design Based on Cement Mechanical Response.
- van der Tuuk Opedal, N., Torsæter, M., Vralstad, T., & Cerasi, P. (2014). Potential leakage paths along cement-formation interfaces in wellbores; Implications for CO₂ storage. *Energy Procedia*, 51, 56–64. <https://doi.org/10.1016/j.egypro.2014.07.007>
- van Genuchten, M. T. (1980). A Closed-form Equation for Predicting the Hydraulic Conductivity of Unsaturated Soils.
- Vrålstad, T., Saasen, A., Fjær, E., Øia, T., Ytrehus, J. D., & Khalifeh, M. (2019). Plug & abandonment of offshore wells: Ensuring long-term well integrity and cost-efficiency. In *Journal of Petroleum Science and Engineering (Vol. 173, pp. 478–491)*. Elsevier B.V. <https://doi.org/10.1016/j.petrol.2018.10.049>
- Wang, W., & Dahi Taleghani, A. (2017). Impact of hydraulic fracturing on cement sheath integrity; A modelling approach. *Journal of Natural Gas Science and Engineering*, 44, 265–277. <https://doi.org/10.1016/j.jngse.2017.03.036>
- Watson, T. L., & Bachu, S. (2009). Evaluation of the Potential for Gas and CO₂ Leakage Along Wellbores.
- Welch, N. J., Frash, L. P., Harp, D. H., & Carey, J. W. (2020). Shear strength and permeability of the cement-casing interface. *International Journal of Greenhouse Gas Control*, 95. <https://doi.org/10.1016/j.ijggc.2020.102977>
- William Carey, J., Svec, R., Grigg, R., Zhang, J., & Crow, W. (2010). Experimental investigation of wellbore integrity and CO₂-brine flow along the casing-cement microannulus. *International Journal of Greenhouse Gas Control*. <https://doi.org/10.1016/j.ijggc.2009.09.018>
- William Carey, J., Svec, R., Grigg, R., Lichtner, P. C., Zhang, J., & Crow, W. (2009). Wellbore integrity and CO₂-brine flow along the casing-cement microannulus. *Energy Procedia*, 1(1), 3609–3615. <https://doi.org/10.1016/j.egypro.2009.02.156>
- William Carey, J., Lewis, K., Kelkar, S., & Zyvoloski, G. A. (2013). Geomechanical behavior of wells in geologic sequestration. *Energy Procedia*, 37, 5642–5652. <https://doi.org/10.1016/j.egypro.2013.06.486>
- Witherspoon, P. A., Wang, J. S. Y., Iwai, K., & Gale, J. E. (1980). Validity of Cubic Law for Fluid Flow in a Deformable Rock Fracture. In *WATER RESOURCES RESEARCH* (Vol. 16, Issue 6).
- Xu, Y., Cavalcante Filho, J. S. A., Yu, W., & Sepehrnoori, K. (2017). Discrete-fracture modeling of complex hydraulic-fracture geometries in reservoir simulators. *SPE Reservoir Evaluation and Engineering*, 20(2), 403–422. <https://doi.org/10.2118/183647-PA>
- Yang, R., Huang, Z., Li, G., Tian, S., Song, X., & Sheng, M. (2016). An Innovative Approach to Model Two-Phase Flowback of Shale Gas Wells with Complex Fracture Networks (Vol. 2). *SPE-181766-MS*
- Zeng, Z., & Grigg, R. (2006). A Criterion for Non-Darcy Flow in Porous Media. *Transport in Porous Media*, 63(1), 57–69. <https://doi.org/10.1007/s11242-005-2720-3>
- Zhang, M., & Bachu, S. (2011). Review of integrity of existing wells in relation to CO₂ geological storage: What do we know? In *International Journal of Greenhouse Gas Control* (Vol. 5, Issue 4, pp. 826–840). Elsevier Ltd. <https://doi.org/10.1016/j.ijggc.2010.11.006>

-
- Zhang, Z., & Nemcik, J. (2013). Fluid flow regimes and nonlinear flow characteristics in deformable rock fractures. *Journal of Hydrology*, 477, 139–151. <https://doi.org/10.1016/j.jhydrol.2012.11.024>
- Zhang, W., & Eckert, A. (2020). Micro-annulus generation under downhole conditions: Insights from three-dimensional staged finite element analysis of cement hardening and wellbore operations. *Journal of Rock Mechanics and Geotechnical Engineering*, 12(6), 1185–1200. <https://doi.org/10.1016/j.jrmge.2020.03.003>
- Zhou, J. Q., Hu, S. H., Fang, S., Chen, Y. F., & Zhou, C. B. (2015). Non-linear flow behavior at low Reynolds numbers through rough-walled fractures subjected to normal compressive loading. *International Journal of Rock Mechanics and Mining Sciences*, 80, 202–218. <https://doi.org/10.1016/j.ijrmms.2015.09.027>
- Zimmerman, R. W., Al-Yaarubi, A., Pain, C. C., & Grattoni, C. A. (2004). Non-Linear Regimes of Fluid Flow in Rock Fractures. *Department of Earth Science and Engineering Imperial College, London SW7 2AZ, UK*